Fys-3921
Master's Thesis in Electrical Engineering

Motion induced electromagnetic fields in the ocean: Exploratory data analysis and signal processing

by

Andreas Eide

Supervisors: Alfred Hanssen and Mårten Blixt

December, 2007

Faculty of Science
Department of Physics and Technology
University of Tromsø

Abstract

We will in this thesis analyse data from antennas located at the seafloor measuring the vertical component of the natural electric field. The internal source to electromagnetic fields in the ocean is saltwater crossing the geomagnetic field, and the main contributor to the motion induced vertical electric field is the water velocity in the East-West direction weighted by the North component of the geomagnetic field. The motivation is to study the motion induced signal which is present in the frequency range 0.1-10 Hz. This is a frequency range of interest when using electromagnetic methods in marine hydorcarbon exploration.

To analyse the electric field data we have implemented and applied the multitaper estimator for spectrum estimation. The multitaper estimator also provide for a test for periodic (sinusoidal) components, which we have implemented and applied. To further analyse the statistics of the motion induced electric field, we have applied both conventional estimators to estimate the statistical properties and the kernel smoothing estimator to estimate the distribution of the data.

The electric field data contained a prominent oscillation visible in the time series, and the spectrum estimates of the recorded data show a prominent peak about 0.15 Hz and with features just above 0.1 Hz and at 0.24 Hz. These features corresponds to the observed periods of the surface waves during the recordings. While the frequency of the prominent peak is rather stable, its level changes more than 10 dB during the recording (30 minutes). Theory and other experiments shows that the surface waves causes pressure fluctuation in the ocean, causing both disturbance in the seafloor and the seawater, which induce electric fields. This mechanism is the most likely source to the fluctuations we see in the measured data.

Acknowledgements

I thank Alfred Hanssen for his excellent work as supervisor during the study, particularly for sharing his knowledge about data analysis and for all the helpful discussions and comments about the manuscript.

The assignment was proposed by Mårten Blixt at Discover Petroleum, which also provided the data sets from the electric field and the antenna position measurements. I thank him for his excellent work as supervisor, and for useful comments and discussions about electromagnetism and the manuscript. I also thank Tom Grydeland at Discover Petroleum for useful comments to the manuscript, and I thank Discover Petroleum in general for sharing their data.

I also thank the helpful people both at Tromsø Geophysical Observatory, University of Tromsø, Norway for providing the geomagnetic data, and Meterologisk Institutt (`www.met.no`) for providing the weather (ocean) data. I also thank Jonathan Lilly (Earth and Space Research, Seattle) for the useful inputs on the ocean wave dynamics.

Contents

Abstract **i**

Acknowledgements **iii**

Contents **v**

1 Introduction **1**

2 Electromagnetic induction in the ocean **5**
2.1 Maxwell equations 5
2.2 Conductivity 7
2.3 Motion induced electric fields 7
2.4 The vertical electric field 8
2.5 Induction in antenna 11
2.6 Noise sources 12
2.6.1 Surface waves induced noise 12
2.6.2 Turbulent Eddies 13
2.6.3 Other noise sources 13

3 Experiment **15**
3.1 Electric field measurements 15
3.2 Measurements of antenna motion 17

4 Signal analysis and processing methods **19**
4.1 Statistical properties 20
4.1.1 Sample moments 21
4.2 Estimation of the probability density 21
4.2.1 Histogram 22
4.2.2 Parzen window estimator 22
4.3 Stationarity 23
4.3.1 Runs Test 24
4.4 Power spectrum estimation 25

4.4.1 Definition of the power spectrum density 25
4.4.2 Basic power spectrum estimators 26
4.5 Multitaper power spectrum estimation 29
4.5.1 Selecting the optimal window functions - discrete prolate spheroidal sequences 29
4.5.2 The multitaper estimator 35
4.6 The chi-square and F-distributions 42
4.6.1 The chi-square distribution 42
4.6.2 The F-distribution 44
4.7 Distribution of spectrum estimates 46
4.8 Confidence interval of the multitaper spectral estimate 48
4.9 Thomson's F-test for single frequency components 49
4.9.1 Numerical example 51

5 Results **53**
5.1 E-field measurements: 50 m cable antenna, Station 1 53
5.1.1 Time series 53
5.1.2 E-field runs test 54
5.1.3 Multitaper estimation, number of averaged eigenspectra 55
5.1.4 Time series, spectral estimates and probability density function estimates 57
5.1.5 Approximate slope of the background spectrum 65
5.1.6 F-test for sinusoidal components 66
5.1.7 Time development of the prominent peak 72
5.2 Measurements of antenna position 76
5.3 Geomagnetic activity 79
5.4 E-field measurements from other locations 81

6 Discussion and conclusions **85**

Bibliography **89**

Chapter 1

Introduction

For marine hydrocarbon (oil/gas) exploration, the most important tool for subsurface imaging is without doubt the seismic reflection method. In seismics, a pressure wave is launched close to the sea surface that reflects at interfaces between formations of different acoustic impedance. By measuring the time it takes for the wave to return to a receiver, a map of the seafloor and the sediments can be retrieved (e.g., Dobrin and Savit [1988]). However, within the last decade, an increasingly important method, named Controlled-Source Electromagnetic (CSEM) method, has appeared (MacGregor and Sinha [2000], Ellingsrud et al. [2002], Eidesmo et al. [2002], Kong et al. [2002], Johansen et al. [2005]). In contrast to seismics, the information in the CSEM method is propagated by the diffusion of electromagnetic energy, and has a resolution proportional to the depth of the target, which is much worse than for seismic methods (e.g., Constable and Srnka [2007]). However, the CSEM method is directly sensitive to the electric resistivity of the sediments, and the resistivity in hydrocarbon filled sediments is substantially higher than for sediments filled with saltwater. Therefore, the CSEM methods can be used to map the resistivity of the sediments, and hence provide a direct measure of the existence of hydrocarbons in the sediments. Academic research on marine electromagnetic methods for analysing the solid Earth beneath the ocean has been quite active since the 70's, and Chave et al. [1991] presents several of the developed methods. It was not until Ellingsrud et al. [2002] and Eidesmo et al. [2002] showed that the method was sensitive enough to detect thin hydrocarbon reservoirs that it caught interest in the hydrocarbon exploration industry. In Norway, Petromarker and EMGS have patented their own CSEM methods, called "Petromarker" and "Sea Bed Logging", respectively.

As an oceanographic tool the electromagnetic methods provide useful measures of ocean currents. Because the marin environment is conductive, any

motion, of the water or of the receiving antennas, will create an electromagnetic force in the Earths magnetic field. The internal source of electromagnetic fields in the ocean is saltwater moving across the geomagnetic field, and particles with opposite charge will due to the Lorentz force be separated into opposite directions and build up an electric field across a seawater stream. By measuring the cross stream voltage, this can be used to monitor ocean streams in terms of velocity, and e.g., Chave and Filloux [1985] and Bindoff et al. [1986], present experiments where the vertical electric field were used as a measure of the long-term East-West water velocity. Larsen [1992] presents a thorough research from the Strait of Florida, where the horizontal cross stream voltage have been measured since 1969 by a long sub sea cable (abandoned communications cable). For a bounded stream through a strait, the velocity can hence be related to the volume transport through the strait. Because of lateral changes in a strait boundaries and inhomogeneous water velocity, there will also be potential difference along the stream boundaries. Harvey and Montaner [1977], Palshin et al. [2002] and Palshin et al. [2006] present experiments, were the voltage along the stream were measured by on-land receivers directed almost parallel to the ocean stream, that give a measure of the tide.

For the CSEM method, any motion induced electric field will appear as an unwanted source of noise. Roughly, it can be expressed as a part of the total measured field as, $\mathbf{E}_{\text{MEAS}} = \mathbf{E}_{\text{CSEM}} + \mathbf{E}_{\text{SW}} + \mathbf{E}_{\text{other}}$. Here, $\mathbf{E}_{\text{CSEM}}$ is related to the field from the CSEM transceiver, $\mathbf{E}_{\text{SW}}$ is the motion induced field, and $\mathbf{E}_{\text{other}}$ is caused by other noise sources, like distortion from the geomagnetic field and noise from the electrodes and electronics. A further complication is that the fluctuation in the electric field at the seafloor is related to the surface waves (Cox et al. [1978], Webb and Cox [1986]), which coincide with important frequencies used in CSEM. The motivation is thus to reduce the effect of $\mathbf{E}_{SW}$, and the presented methods and analysis will be useful for further analysis of the motion induced field.

We will in this thesis present measured data of the vertical component of the motion induced electric field, recorded by a vertical antenna placed at the seafloor. During the recordings, the position of the antenna was also monitored to reveal relations between the motion of the antenna and the recorded electric field. Unfortunately, because of the lack of accuracy in the position data, we can not tell if the observed motion were the actual motion of the antenna, or an effect of uncertainties in the measurement. We will therefore focus on analysing the electric field data. The frequency range of interest is 0.1-10 Hz, and observations of the vertical electric field in this frequency range

are limited.

To analyse the electric field data, we will present some advanced data analysis methods in great detail, in particular the multitaper spectrum estimator (Thomson [1982]), which has good variance properties, also for relatively short data segments. By the use of the multitaper method we can also extend the spectrum analysis with an F-test to search for single frequency components (proposed by Thomson [1982], example of implementation by Lees [1995]). We have implemented an automatic version of the F-test which will be applied. To further analyse the statistics of the motion induced electric field, we will apply both conventional estimators to estimate the statistical properties, and also apply a more advanced kernel smoothing estimator of the probability density function (e.g., Silverman [1986]).

In Chapter 2 we will describe the electromagnetic properties of the ocean, the vertical electric field in particular and noise sources. The measurement setup is described in Chapter 3. In Chapter 4 we present the analysis methods, and the multitaper spectrum estimator in particular. We then apply the methods to the real data, and the results are presented in Chapter 5. The methods and results are discussed in Chapter 6, which also contains the conclusions.

Chapter 2

Electromagnetic induction in the ocean

In this chapter we will describe some of the electromagnetic properties of the ocean. We will derive an approximation of the electric field measured by a vertical antenna, and describe the dominant internal noise sources that generate fluctuation in the electric field between $0.1-10$ Hz.

2.1 Maxwell equations

For electromagnetic fields at low frequency in the conducting ocean and seabed, the conductive electric currents are dominant, and Maxwell's equations simplifies to (e.g., Larsen [1973])

$$\nabla\cdot\mathbf{D} = q \tag{2.1}$$

$$\nabla\cdot\mathbf{B} = 0 \tag{2.2}$$

$$\nabla\times\mathbf{E} = -\frac{\partial\mathbf{B}}{\partial t} \tag{2.3}$$

$$\nabla\times\mathbf{B} = \mu\mathbf{J}. \tag{2.4}$$

Here, $\mathbf{B}$ is the magnetic induction (Wb/m^2), $\mathbf{E}$ the electric field (V/m), $\mathbf{D}$ is the electric displacement (C/m^2), $\mathbf{J}$ is the electric current density (A/m^2), and q is the electric charge density, C/m^3. The magnetic permeability μ is equal to $\mu_0 = 4\pi\times10^{-7}(H/m)$ (e.g., Keller [1987]).

Ohm's law for a moving conducting medium with fluid particle velocity $\mathbf{v}$ (m/s) and conductivity σ $(\Omega\,\mathrm{m})^{-1}$ is given by (e.g., Sanford [1971])

$$\mathbf{J} = \sigma(\mathbf{E}+\mathbf{v}\times\mathbf{B}). \tag{2.5}$$

When taking the curl of Eq. (2.3) and inserting (2.4), the differential equation for **E** can be derived as

$$\nabla \times \nabla \times \mathbf{E} = -\frac{\partial}{\partial t}(\nabla \times \mathbf{B}) \tag{2.6}$$

$$\nabla(\nabla \cdot \mathbf{E}) - \nabla^2 \mathbf{E} = -\mu_0 \frac{\partial}{\partial t}(\mathbf{J}). \tag{2.7}$$

For simplicity we assume zero velocity of the water, $\mathbf{v} = 0$, and Ohm's law becomes $\mathbf{J} = \sigma \mathbf{E}$. In addition we assume $\nabla \cdot \mathbf{J} = 0$. The leftmost part in (2.7) then becomes zero,

$$\nabla(\nabla \cdot \mathbf{E}) = \nabla(\nabla \cdot \mathbf{J}/\sigma) = 0, \tag{2.8}$$

and when inserting $\mathbf{J} = \sigma \mathbf{E}$ into the right side of Eq. (2.7), we get

$$-\nabla^2 \mathbf{E} = -\mu_0 \sigma \frac{\partial}{\partial t}(\mathbf{E}) \;\; => \;\; \frac{\partial \mathbf{E}}{\partial t} - \frac{1}{\mu_0 \sigma} \nabla^2 \mathbf{E} = 0. \tag{2.9}$$

This equation can be recognised as the diffusion equation

$$\frac{\partial \mathbf{E}}{\partial t} - D \nabla^2 \mathbf{E} = 0, \tag{2.10}$$

where the diffusion coefficient is $D = 1/\mu_0 \sigma$. As we can see the diffusion depends on the conductivity, which is an important property for electromagnetic exploration. When e.g., an electric field is set up by a transceiver and then turned off, the decay rate of the electric field measured by a distanced receiver can be used to map the conductivity in the sediments between the transceiver and the receiver, and areas with high resistivity (low conductivity) can be detected.

The skin depth δ_s is an important parameter both for how deep external electromagnetic fields (geomagnetic) penetrate into the ocean, and for how deep an electromagnetic field set up by a CSEM transceiver penetrate into the sediments. It represent the distance an electromagnetic wave diffuse into a conducting medium, and where the amplitude is e^{-1} of its initial value (e.g., Filloux [1973])

$$\delta_s = \sqrt{\frac{1}{\pi f \mu_0 \sigma}}. \tag{2.11}$$

Here, f is the frequency of the electromagnetic field, and σ is the conductivity of the medium.

It should be mentioned that Løseth et al. [2006] reviewed the theory of EM

fields propagating in the conducting ocean, and concluded that the approximation leading to a diffusion equation is valid, but that mathematically it is more correct to express it as wave propagation with dispersion and attenuation.

2.2 Conductivity

The ocean conductivity depends mostly on temperature and salinity, and can be approximated as (e.g., Chave et al. [1991]),

$$\sigma(T) = 3 + T/10. \tag{2.12}$$

Here, T is given in Celsius, and $T/10$ is the approximation of the contribution from the salinity. For the sediments, the conductivity can be modelled with Archie's law (e.g., Keller [1987])

$$\sigma = a\sigma_W \phi^m, \tag{2.13}$$

where ϕ is the porosity of the rock, σ_W is the conductivity of the pore water. Here, a and m are fitting parameters for different rock types which are found experimentally. Some of the pores can be occupied by hydrocarbons (oil/gas) with low conductivity, replacing the conductive water, and the conductivity of the rock can then be written as

$$\sigma = a\sigma_W (1 - S_{HC})^n \phi^m, \tag{2.14}$$

where S_{HC} is the saturation of hydrocarbons, and ϕ is the porosity of the rock, and n the saturation factor. As we can see from latter equation, the conductivity of the rock will decrease if saturated by hydrocarbons, and increase its electric resistivity.

2.3 Motion induced electric fields

Following Sanford [1971], we assume the electric field to be quasi-static. This means that $\nabla \times \mathbf{E} = \mathbf{0}$, and a scalar electric potential ϕ exists ($\mathbf{E} = -\nabla\phi$). With this approximation, the time variations of the magnetic induction is neglected, and the contribution from the magnetic field is only due to the static geomagnetic field, $\mathbf{F}$. If we rearrange Eq. (2.5), and replace $\mathbf{B}$ with $\mathbf{F}$, we get

$$\mathbf{E} = \mathbf{J}/\sigma - \mathbf{v} \times \mathbf{F}. \tag{2.15}$$

A stationary receiver will experience particle motion at the same velocity as the water velocity, and Eq. (2.15) is a good approximation of the measured

electric field when using a receiver fixed to the sea floor (e.g., Sanford [1971], Filloux [1973]).

For a receiver drifting along with the water velocity, the water motion seen from the receiver is zero, and the measured electric field is given by (Filloux [1973])

$$\mathbf{E} = \mathbf{J}/\sigma \tag{2.16}$$

For a vertical receiver, one electrode is fixed at the seafloor and the other held up by a buoy. The buoy will drift with the water stream until a balance with the buoy up drift and the cable tension is reached. In this position the cable between the electrode and the buoy will partly move with the water. The apparent velocity seen from the receiver will therefore be a combination of the water motion and the motion of the receiver.

2.4 The vertical electric field

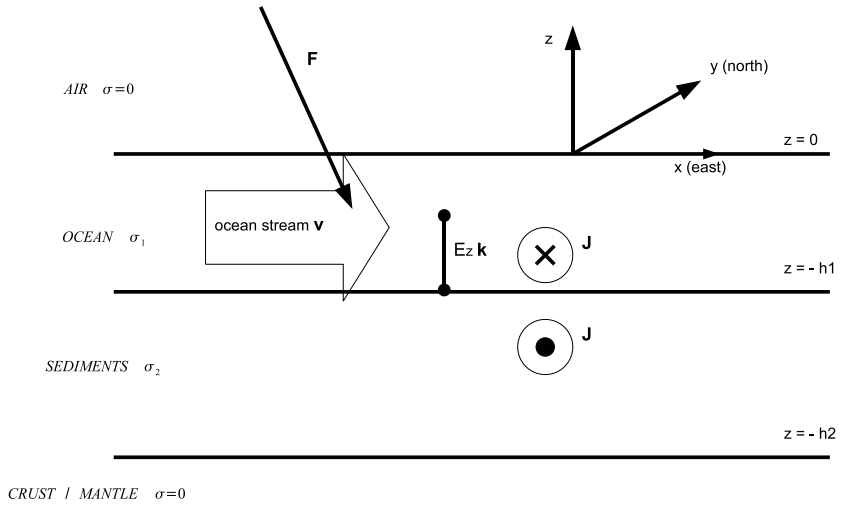

Figure 2.1: Simple model of a two layered earth, with a conductive ocean over a layer of conductive sediments. The layers are isolated by non-conductive air and crust. A vertical receiver is fixed to the sea floor in the middle of the figure.

We now assume a wide laminar ocean stream with a homogeneous velocity in either north-south or east-west direction. To calculate the electric field we use typical values of the static earth magnetic field at a high latitude. We neglect the contribution from sea surface waves and sea floor topographic, and assume a flat sea surface and sea floor. The model is placed in a Cartesian coordinate system, with x to East, y to North and z upwards, with the respective unit vectors **i**, **j** and **k** (see figure 2.1).

First we look at the contribution from $\mathbf{v}\times\mathbf{F}$ and neglect the part containing the current density ($\mathbf{J}/\sigma$), to obtain

$$\mathbf{E} = -\mathbf{v}\times\mathbf{F} = (v_z F_y - v_y F_z)\mathbf{i} + (v_x F_z - v_z F_x)\mathbf{j} + (v_y F_x - v_x F_y)\mathbf{k}. \tag{2.17}$$

A vertical antenna will only detect the vertical component, which has an amplitude of $(v_y F_x - v_x F_y)$. The time varying geomagnetic field is assumed to be small, and the E-field as a function of time, can be approximated as

$$E_z(t) = v_y(t)F_x - v_x(t)F_y. \tag{2.18}$$

We now see that changes in the local horizontal water velocity **v**, will actually induce an vertical electric field. Since F_x and F_y are the horizontal components of the static geomagnetic field, the vertical electric field gives a measure of the water velocity in the geomagnetic East-West direction.

On-land magnetometers normally measure the geomagnetic field in a vertical component Z, a horizontal component H, and a declination D given in degrees east of North. Figure 2.2 place these components in our coordinate system, giving $F_x = H\sin(D)$ and $F_y = H\cos(D)$. The declination D is normally small, but its value depends on the location, but will in general increase at high latitudes. The electric field data presented in this thesis, were recorded at about 61°North. If we use the values from the nearest magnetometer station (Solund, 61°N, Tromsø Geophysical Observatory [2007]), it shows a typical declination of $D = -1.2°$. This gives $|F_y/F_x| = 1/\tan(D) \approx 50$, and for our location the main contributor to the vertical E-field is the water velocity in the latitudinal (zonal) East-West direction, weighted by the horizontal North component of the geomagnetic field

$$E_z(t) \approx -v_x(t)F_y. \tag{2.19}$$

A typical ocean stream is in the range 1 m/s or less (Sanford [1971]). Again, we use the typical geomagnetic field from Solund (61°N, Tromsø Geophysical Observatory [2007]), and for a ocean velocity of 1 m/s in the East-West direction, the vertical electric field would be

$$|E_z| = 1\ \text{m/s} \cdot 14500\ \text{nT} \cdot \cos(1.2) \approx 14.5\ \mu\text{V/m}.$$

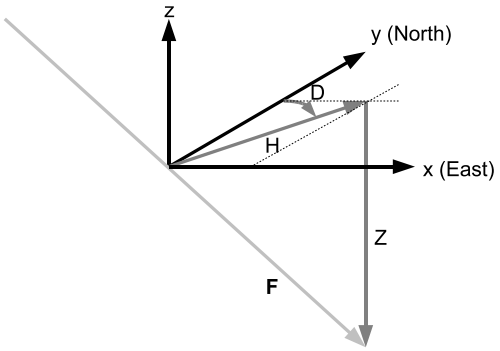

Figure 2.2: The figure show how the Z, H and D components of the geomagnetic field **F** is related to our coordinate system.

Eq. (2.18) is a good approximation for the vertical electric field, and is the same approximation as Chave and Filloux [1985] and Bindoff et al. [1986] used for their vertical receivers. Sanford [1971] derived a thorough expression for $\mathbf{J}/\sigma$, and given a broad unbounded ocean stream he concluded the vertical component to be small. Note that $\mathbf{J}/\sigma$ contains the contribution from distant ocean streams, and since it now can be neglected, measurements of the vertical electric field is mainly a measure of the water flow local to the receiver (also mentioned by Chave et al. [1989]).

In contrast to the vertical, the horizontal electric field is in addition to the local water motion, related to an average motion of the water column above the receiver, weighted by the conductivity of the ocean and the sediments. It is derived by Sanford [1971] and called the weighted average velocity, denoted by $\overline{\mathbf{v}}^*$. With the vertical boundaries from Figure 2.1 it is defined as

$$\overline{\mathbf{v}}^* = \frac{\int_{-h_1}^{0} \sigma \mathbf{v} \, \mathrm{d}z}{\int_{-h_2}^{0} \sigma \, \mathrm{d}z}. \tag{2.20}$$

If the vertical receiver tilt out of the vertical with a small angle θ, it will measure fractions of the horizontal field (Chave and Filloux [1985]). If we now use a unit vector **r** along the antenna, and use the first part of the $\mathbf{J}/\sigma$ derived by Sanford [1971], where the vertical water velocity is assumed negligible compared to the horizontal velocity, then the tilted vertical receiver will measure the electric field projected into **r**, approximated as,

$$E = \left[-\overline{v_y}^* F_z \mathbf{i} + \overline{v_x}^* F_z \mathbf{j} + (v_y F_x - v_x F_y)\mathbf{k} \right] \cdot \mathbf{r}. \tag{2.21}$$

2.5 Induction in antenna

If the cable between the electrodes is not fully stretched, the straight line between the electrodes and the cable make an electric loop with an effective area (see Figure 2.3). As mentioned by Filloux [1973], induced signals can occur in the loop. If the antenna is moving or oscillating, the area of the loop will change and the magnetic flux through the loop will change. According to Lenz's law, this will induce electric current in the loop, which in turn affects the voltage and the electric field measured by the antenna. Cox et al. [1978] reported that slight jerking of their receiver system caused large spurious signals, and indicated that it could be caused by induced charge in the receiver cables. For a vertical antenna, the force from the surrounding moving water can probably bend the cable slightly, causing an effective area between the cable and the straight line between the electrodes. Then, all movements of the antenna causing this area to change can be a potential source to the measured signal.

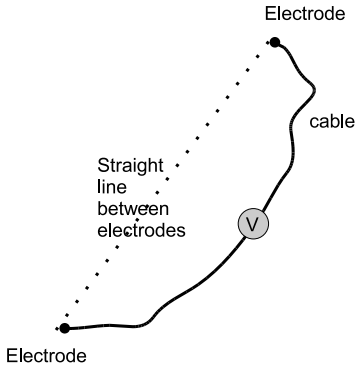

Figure 2.3: The electric loop between the straight line between the electrodes and the cable connected to the electrodes.

2.6 Noise sources

2.6.1 Surface waves induced noise

Cox et al. [1978] investigated the electromagnetic signature generated by swell with a period of the dominant wave, $T \approx 10$ s. Electromagnetic fields generated at the sea surface, will have the same frequency as the surface wave, $f = 1/T \approx 0.1$ Hz. The ocean skin depth for this frequency will be $\delta_s = \sqrt{1/\pi f \mu_0 \sigma} \approx \sqrt{1/(\pi \cdot 0.1 \cdot 4\pi \times 10^{-7} \cdot 3.3)} \approx 870$ m, where the ocean conductivity is assumed to be $\sigma = 3.3$ $(\Omega\text{m})^{-1}$ (from Larsen [1973]). Electromagnetic fields propagating this distance of ocean depth will be strongly attenuated, and with a strength of swell generated magnetic field at the sea surface $b \lessapprox 10$ nT (from Lilley et al. [2004]), the propagating electromagnetic field will definitely decay to undetectable levels below the skin depth. Still, the electromagnetic signature related to swell are strong also at greater depths.

Theory derived by Longuet-Higgins [1950] show that when surface waves from different directions interacts, they generate pressure oscillations in the underlying ocean. Surface waves from opposite directions of approximately the same wavelength and phase will form standing waves twice per wave period when they interact head on, and the oscillations will be around twice the swell frequency. The pressure fluctuations will propagate through the ocean, and when reaching the solid ocean floor, it may generate small motions in the sea floor and cause small scale quake disturbances, called microseism. In the ocean, spatial differences in the pressure may set up ocean streams, which in turn induce electromagnetic fields (Cox et al. [1978]).

Cox et al. [1978] measured the horizontal electric field with a receiver fixed to the seafloor at depths greater than the electromagnetic skin depth (1.2 to 3.5 km), and the spectra of the measured fields from a number of sites contained significant peaks at twice the swell frequency. Webb and Cox [1986] measured simultaneously the pressure fluctuations and the horizontal electric field at the sea floor. They related the electric field to the motion of charged particles above and under the receiver fixed to the sea floor. For a receiver fixed to the sea floor they derived the approximation of the measured field, given by,

$$\mathbf{E} \approx (\mathbf{v_s} - \mathbf{v}) \times \mathbf{F}, \tag{2.22}$$

where $\mathbf{v_s}$ represent the movement of the seafloor, and $\mathbf{v}$ is the seawater velocity just above the sea floor. Their measurements showed changes in the spectrum $0.1 - 1$ Hz, with strong relations between the electric field and the pressure fluctuation at the seafloor and the surface waves. The dominant peak in their

recordings were a "single-frequency" peak at the same frequency as the swell at 0.1 Hz. Peaks related to storm-generated wind waves were also observed between 0.4-0.5 Hz.

Sutton and Barstow [1990] made sea floor pressure measurements to investigate the pressure oscillation in the frequency band 0.004-0.4 Hz. They also reported a correlation between wind waves and the pressure oscillations in the band 0.2-0.4 Hz.

In this study, we focus on the electric field in the frequency band between 0.1-10 Hz. Based on the papers above, we can expect ocean surface waves will induce electric fields in the frequency band 0.1-0.5 Hz, either by movements of the solid sea floor and the lower electrode fixed to sea floor, or oscillating ocean streams.

2.6.2 Turbulent Eddies

Turbulent eddies can arise when the moving water pass an obstacle, like in the wake of an electrode or because of topographic changes on the seafloor. The water rotation in the eddy, will generate local fluctuations in the electric field. From Cox et al. [1978] we have that the fluctuation of the measured voltage caused by an eddy adjacent to an electrode is,

$$\mathbf{l} \cdot \mathbf{v_e} \times \mathbf{F}, \tag{2.23}$$

where $\mathbf{l}$ is the scale of the eddy, and $\mathbf{v_e}$ is the velocity of the rotating water in the eddy. The frequency components of the electric field fluctuations, will be related to the drifting velocity v of the water surrounding the eddy, and centred around $f = v/(2\pi l)$ Hz.

2.6.3 Other noise sources

There are several other sources present that can generate noise at the frequencies of interest for CSEM, like the electrodes, the internal electronic circuits, currents in the ionosphere and magnetosphere, and other man-made sources.

Flucations in the vertical electric field at the sea floor are mainly of oceanic origin (e.g., Chave [1984]). The conductive ocean acts as a low pass filter for fluctuating EM fields generated above it in the ionosphere and magnetosphere, and as shown by e.g., Chave et al. [1991] small amount of power will be

present at frequencies above 0.1 Hz at few hundred meters depth. In the latter paper they also calculated the sea surface to sea floor response for external EM-fields, and the horizontal magnetic component, are the most attenuated component.

Low conductivity layer can act as a channel for low frequency noise, and man-made noise can propagate offshore and contaminate recordings done in otherwise "quiet" areas (Chave et al. [1991]). The measurements presented in the next chapter were done almost 100 km from land, and the shallow part of the subsurface contained no known low conductivity layers (Blixt [2007]), so we assume this contribution to be negligible. The equipment that was used for collecting the data analysed here, has also gone through rigorous tests to ensure that the noise level is low enough to see the effect of motion induced electric fields.

Chapter 3

Experiment

The experiment and data collection were done by Petromarker on a survey assigned by Discover Petroleum.

3.1 Electric field measurements

The vertical electric field was measured by receivers located at the ocean floor. Each receiver station contained two antenna types, cable antennas and hose antennas, and two lengths (25 m and 50 m) of each type were used. All the antennas were bundled together and a dead weight of 680 kg in seawater kept the receiver steady at the seafloor. A buoy with an uplift of 310 kg kept the bundled antennas vertical. For the cable antennas, the electrodes are connected in each end of the cables, and the potential difference between them is recorded as a voltage. For the hose antennas, both electrodes are located at the seafloor, where one electrode measure the saltwater potential at the seafloor. The other electrode have seawater contact inside the hose, and the water inside the hose have approximately the same potential, given by the saltwater potential at the open end of the hose. The hose antennas are also called salt bridge antennas (Filloux [1973]). The EM-receiver station is part of a transceiver/receiver setup for CSEM measurements, but the data of our interest are the recordings while the transceiver are turned off, and the receiver station acts like a passive recorder of the natural background EM-signal. Figure 3.1 shows the EM-receiver station that was placed at the seafloor, including the different antennas.

The data were collected at a sampling rate of $f_s = 500$ Hz, and data were recorded for 30 minutes. Given in coordinated universal time (UTC), recordings started at 20:54 UTC, September 19, 2007. We will mainly analyse the

data from the 50 m cable antenna, placed at a depth of 316 m, located at approximately 61°North (Station 1). Data from other stations are also available, and the locations of the stations are shown in Figure 3.2, here given in meters in universal transverse mercator (UTM) coordinates.

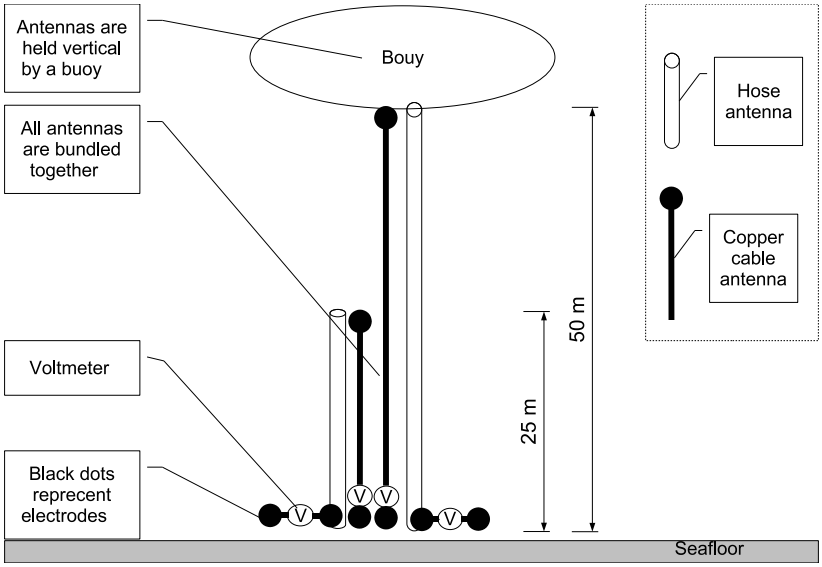

Figure 3.1: Sketch of the vertical antennas in the EM-receiver station. At the lower end, all antennas are connected to a common base anchored to the seafloor with a deadweight. All the antennas are bundled together, and held up by a common buoy. The two hose antennas (25 and 50 m) are drawn as pipes, while the thick black line represent the cable antennas (also 25 and 50 m).

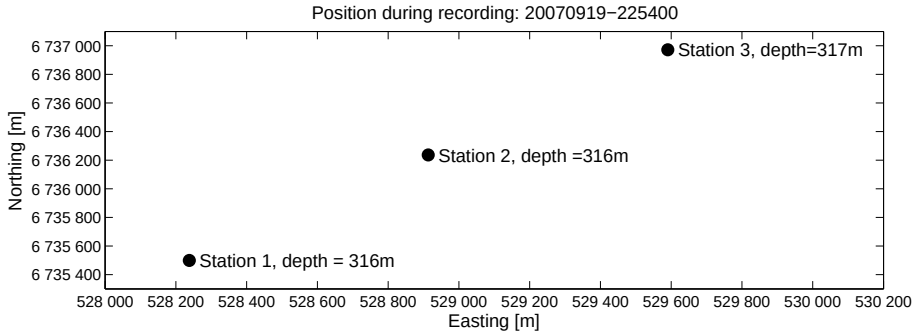

Figure 3.2: Location of the receiver stations during the recordings (UTM zone V31). The analysis will mainly cover the 50 m cable antenna in the position labeled "Station 1", seen in the lower left corner.

3.2 Measurements of antenna motion

As the movement of the EM-receivers and the water around the antenna induce unwanted signals, the purpose of measuring the position (and velocity) of the EM-receivers, is to achieve an independent data series that can be used to remove or predict this unwanted electric field.

To monitor the position and the motion of the receivers located at the seafloor, a setup with transponders was applied. A sketch of the setup is drawn in Figure 3.3. At the EM-receiver station, one transponder was attached to the seafloor base close to the lower electrodes, and one transponder was connected above the upper buoy (which holds the cable and hose receivers) and held up by an additional buoy. The upper transponder was located approximately 5 m above the upper electrodes. The transponders connected to the EM-receiver station transmits sound waves that propagates through the ocean, and is detected by a receiving transponder at the operation vessel. This receiver contain several transponders, which measures both the distance to the transmitting transponders and their location relative to the vessel. The system is called "Mini SSBL Transponder" and additional information about the system can be found at http://www.km.kongsberg.com [2007]. The horizontal distance between the operation vessel and the receiver station at the seafloor was approximately 250 m.

Since the position of the EM-antennas was measured with reference to the operation vessel, the position of the vessel was measured with a global position system (GPS) and then the EM-antennas could be placed geographically in UTM coordinates. During measurements of the background electric field, the transponder system simultaneously measured the location of the EM-receivers at a sampling rate $f_s = 1$ Hz. After correction of the vessel position and sound speed in the ocean, the positioning accuracy was calculated to approximately ± 1 m (Blixt [2007]).

Based on the first derivative of the position data $x[n]$, approximate values of the velocity were found numerically, using both the forward- and central difference methods. From the position data $x[0], x[1], ..., x[N-1]$ the velocity was calculated by the forward difference method as (e.g., Landau and Pàez [2004])

$$\widehat{v}_{fwd}[n] = \frac{x[n+1] - x[n]}{\Delta t}, \tag{3.1}$$

where the last $x[n]$ sample were used as stopping condition, resulting in $N-1$ values of $\widehat{v}_{fwd}[n]$. For the central difference method, the following scheme

was used (e.g., Landau and Pàez [2004])

$$\widehat{v}_{cent}[n] = \frac{x[n+1] - x[n-1]}{2\Delta t}. \tag{3.2}$$

Here, the first and the last samples, $x[0]$ and $x[N-1]$, were used as starting and stopping conditions. Thus, from N samples of $x[n]$, we get $N-2$ samples of the velocity when using the central difference method.

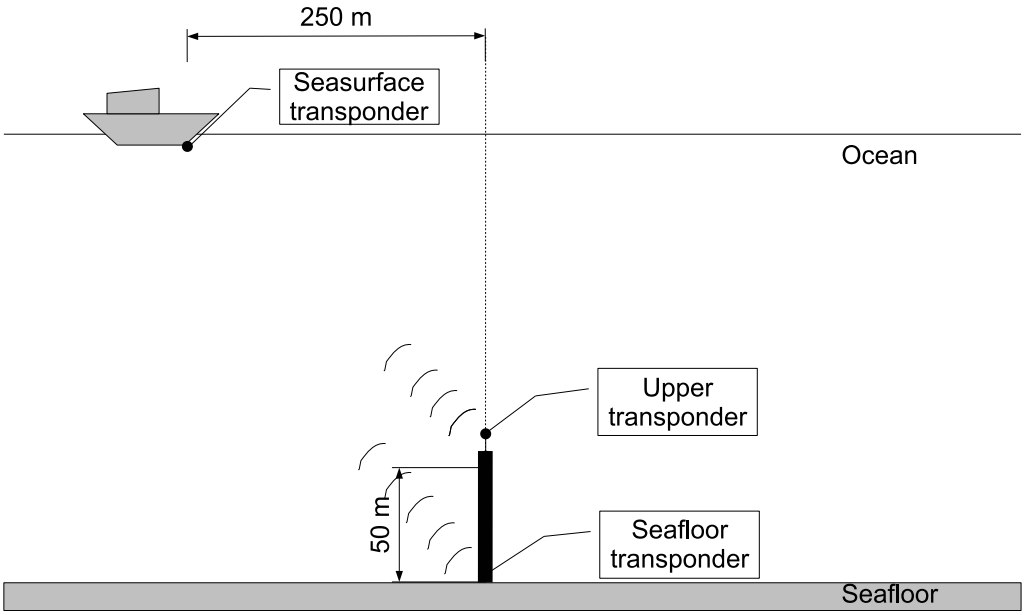

Figure 3.3: Setup of the antennas position measurement. The receiving transponder is attached to the operation vessel, one transmitting transponders is attached to the seafloor base (where the lower electrodes are located), and one to the main buoy, held up by an additional buoy. The upper transponder is therefore located 5 m above the upper electrodes. The EM-receiver station is shown as the thick black line in the lower part of the figure.

Chapter 4

Signal analysis and processing methods

To examine and characterise the measured data, we will in this chapter present a number of nonparametric methods. The nonparametric approach is a natural choice when a priori information of statistical properties of the signal is unknown. The presented methods will cover stationarity (runs-test), probability density function (Parzen kernel estimation) and the most thorough part will cover the power spectrum density (multitaper estimators, and the multitaper F-test).

4.1 Statistical properties

To characterise the measured data it is useful to estimate the mean and the variability (by the standard deviation or the variance) of the data. In addition, skewness and kurtosis gives us measures of how the data is distributed relative to normal distributed data.

For a random variable X, the statistical properties can be described by its moments. The arithmetic mean is defined as the first moment about zero (e.g., Stuart and Ord [1987](§ 2.3)),

$$\mu = E\{X\} = \int_{-\infty}^{\infty} x f(x) dx.$$

Here, $E\{\cdot\}$ denotes the expectation operator, and $f(x)$ denotes the probability density function (PDF) of X. The measure of spread around the mean value is given by the variance σ^2, or the standard deviation σ, which is the positive square root of the variance and in same units as the mean. The variance is given as the second moment about mean (e.g., Stuart and Ord [1987](§ 2.19))

$$m_2 = \sigma^2 = E\left\{(X-\mu)^2\right\} = \int_{-\infty}^{\infty} (x-\mu)^2 f(x) dx.$$

If X is a Gaussian distributed random variable, then the PDF is fully described by the mean and variance.

Skewness is a dimensionless measure of the asymmetry of the PDF (around its mean). It is given as the third moment about mean, normalised by σ^3 (e.g., Stuart and Ord [1987](§ 3.31)),

$$sk = \frac{m_3}{\sigma^3} = \frac{E\left\{(X-\mu)^3\right\}}{\sigma^3}.$$

Gaussian distributions are symmetric, and hence have zero skewness. Negative skewness indicate a non Gaussian left skewed PDF with more data in the left tail (right skewed if skewness is positive).

Kurtosis is a measure for the "peakedness" around the mean (also dimensionless), and the weight of the tails compared to a Gaussian PDF. It is given by the fourth moment about mean, normalised by σ^4 (e.g., Stuart and Ord [1987](§ 3.31)),

$$k = \frac{m_4}{\sigma^4} = \frac{E\left\{(X-\mu)^4\right\}}{\sigma^4} - 3.$$

Here, the number three is subtracted to give zero kurtosis for the Gaussian distribution. Compared to a Gaussian distribution, negative kurtosis indicate a PDF which is more flat around mean and with lighter tails. A positive kurtosis indicates a PDF which is more peaked around mean and with heavier tails.

4.1.1 Sample moments

The following estimators will be used to calculate the sample moments based on the sampled data $x[n]$ (e.g., Press et al. [1992](Ch. 14.1)).

Mean:
$$\overline{x} = \frac{1}{N}\sum_{n=0}^{N-1} x[n], \tag{4.1}$$

Standard deviation:
$$\widehat{\sigma} = \sqrt{\frac{1}{N-1}\sum_{n=0}^{N-1}(x[n]-\overline{x})^2}, \tag{4.2}$$

Variance:
$$\widehat{\sigma}^2 = \frac{1}{N-1}\sum_{n=0}^{N-1}(x[n]-\overline{x})^2, \tag{4.3}$$

Skewness:
$$\widehat{sk} = \frac{1}{\widehat{\sigma}_N^3}\cdot\frac{1}{N}\sum_{n=0}^{N-1}(x[n]-\overline{x})^3, \tag{4.4}$$

Kurtosis:
$$\widehat{k} = \frac{1}{\widehat{\sigma}_N^4}\cdot\frac{1}{N}\sum_{n=0}^{N-1}(x[n]-\overline{x})^4 - 3. \tag{4.5}$$

Note that for the skewness and kurtosis estimators, we will divide by the biased estimator $\widehat{\sigma}_N$ of the standard deviation

$$\widehat{\sigma}_N = \sqrt{\frac{1}{N}\sum_{n=0}^{N-1}(x[n]-\overline{x})^2}.$$

4.2 Estimation of the probability density

In addition to the sample moments, an estimate of the probability density function (PDF) is useful to reveal the statistical nature of the observed data. For a random variable X, the PDF is defined as $f(x) \geq 0$, $\forall x$, and $\int_{-\infty}^{\infty} f(x)dx = 1$. From the PDF we can also find the probability of X being within a given interval, e.g., the probability of X being between a and b is given by (e.g, Silverman [1986])

$$P(a \leq X \leq b) = \int_a^b f(x)dx.$$

4.2.1 Histogram

The most basic estimator of the PDF is the normalised histogram. Here, the amplitude of the data are distributed in a user selected number of bins. We count the number of samples in each bin, and by dividing this number by total number of samples and the binwidth, we get a crude estimate of the probability for a sample falling into the different bins. For the observed data denoted x_n, and $n = 1,2,...,N$, binwidth b and number of samples N, the histogram estimator of the PDF can be written as (Wand and Jones [1995])

$$\widehat{f}(x) = \frac{\text{no. of observations of } x_n \text{ in bin centered at } x}{Nb}. \tag{4.6}$$

This estimator results in a discontinuous function, which is very sensitive to our choice of number and width of the bins.

4.2.2 Parzen window estimator

A more convenient method than the histogram is the Parzen window estimator, named after the inventor Parzen [1962]. Here, a smooth and normalised function, a so-called kernel, is centered with its origin at each data point x_n. By summing the kernels we achieve a continuous estimate, which also has good statistical properties (e.g., Parzen [1962], Wand and Jones [1995] and Hanssen et al. [2003]).

If we have N independent identically distributed samples x_n, and $n = 1,2,...,N$, the kernel estimate of the PDF at amplitude x, is given by Parzen [1962],

$$\widehat{f}(x) = \frac{1}{N}\sum_{n=1}^{N}\frac{1}{b}\phi\left(\frac{x-x_n}{b}\right). \tag{4.7}$$

At every x position we place the smoothing kernel $\phi(\cdot)$ and by $(x - x_n)$ the kernel will be centered with its origin in each data point x_n. The sum of all the kernel values at amplitude x is then scaled to get the estimated value $\widehat{f}(x)$. The binwidth parameter b, is now a width parameter defining the shape of the kernel function $\phi(\cdot)$ and thereby also gives the level of smoothing. For a valid estimator the kernel function need to fulfil the following constraints

$$\phi(v) \geq 0 \text{ and } \int_{-\infty}^{\infty}\phi(v)dv = 1, \tag{4.8}$$

where $v = (x - x_n)/b$. To ensure that the estimate in Eq. (4.7) results in a density, the kernel is chosen to be a symmetric distribution function. The

standard Gaussian distribution function ($N(0,1)$)

$$\phi(v) = \left(1/\sqrt{2\pi}\right) \exp\left(-v^2/2\right), \tag{4.9}$$

is a good standard choice (e.g., Theodoridis and Koutroumbas [1998] and Hanssen et al. [2003]), and will be the smoothing kernel used in this thesis. The choice of the width parameter b is crucial for our estimate. If b is too small, the variance of the estimate will be unacceptable, and if b is too big, the bias increases and we lose details in the estimate. Under the assumptions of Gaussian observed data and a Gaussian kernel, an optimal value of b is given by (Silverman [1986])

$$b = \widehat{\sigma} \left(\frac{4}{3N}\right)^{(1/5)}, \tag{4.10}$$

where $\widehat{\sigma}$ is calculated from the observed data using the sample standard deviation in Eq. (4.2).

4.3 Stationarity

Several classes of stationarity exist, where a strict stationarity process is one for which the probability density function of all orders do not change with time. This is a very strict and difficult task to test for in a given sample of data. The spectrum estimation methods in the following sections are developed based on the assumption of wide-sense (or weak) stationary process. For a stochastic process $X(t)$, the process is called wide-sense stationary if the following conditions are met (e.g., Bendat and Piersol [2000]):

1. $E\{X(t)\} = \text{constant}$
2. $R_{XX}(t_1, t_2) = E\{X(t_1)X(t_2)\} = E\{X(0)X(\tau)\} = R_{XX}(\tau)$.

In words, the expectation value does not change with time, and the autocorrelation between the process X_{t_1} observed at time t_1 and X_{t_2} at time t_2 only depends on the time difference $\tau = t_2 - t_1$. If only the first condition is met, the process is called stationary in the mean.

In this thesis we will check if the mean and the variance change with time using the so-called runs test (e.g., Shiavi [1999]). For the spectrum estimators in the following sections, a nonstationary process will cause bias in the estimates. For example, if we record data for a given time T, and the data contains a signal with period greater than T, this will cause the mean to change with time and hence the data set will be nonstationary. In the spectrum estimate this will cause a bias for the lowest frequencies.

4.3.1 Runs Test

To test whether the data come in a random order, the nonparametric runs test can be used to check for trends in the sample moments (e.g the mean and variance). We will here use the method as explained in the book Shiavi [1999] (p.198). The data set is divided into N_s subsets, and the sample mean (or other moments) are calculated for each subset, giving a sequence of N_s mean values. We then find the median value of this sequence (median of the sample mean from all subsets). By comparing the mean values and the median value we generate a run sequence that only indicate if the subset value is greater (+) or less (-) than the median value, e.g.,

$$\text{runs sequence}: \ [+-+++--+---+]$$

We now count the numbers of runs, r, where adjacent subsequences of same sign is counted as a run, also including single events of a sign as one run. Alternatively, the number of runs can be counted as numbers of sign changes, including the first sign as a change of sign (included as 1 in following equation), $r = 1 +$ (number of sign changes). For the runs sequence above, the number of runs is $r = 7$.

From Shiavi [1999] the number of runs have a mean and variance given by

$$m_r = (N_s/2)+1 \qquad \sigma_r^2 = \frac{N_s(N_s-2)}{4(N_s-1)}. \tag{4.11}$$

The null hypotesis is that the runs sequence is N_s independent measures from the same random variable. To form the confidence interval we use the table in Shiavi [1999](p.199). For example, if $N_s = 10$, the 95% confidence interval is given by $2 < r \leq 9$. An approximately 95% interval can be formed as $[m_r - 2\sigma_r \leq r \leq m_r + 2\sigma_r]$, where $2\sigma_r$ is rounded off to the nearest integer. If the number of runs is outside the confidence interval, we reject the random order hypothesis, which also indicate nonstationary data.

An alternative method to the runs test could be the reverse arrangement method given in Bendat and Piersol [2000](p.105)

4.4 Power spectrum estimation

4.4.1 Definition of the power spectrum density

When analysing real data, the estimation of the power spectrum density (PSD) is useful to predict the power contribution from different frequency intervals, and hence help us to describe and understand the observed time-series. We will now define the power spectral density following Hanssen [2003]. Similar approaches are also given in e.g., Percival and Walden [1993] and Shiavi [1999].

To calculate the energy and the Fourier transform of a realization $x(t)$ of the stochastic process $X(t)$, it needs to be absolute integrable ($\int_{-\infty}^{\infty}|x(t)|dt<\infty$). For a stochastic process that fluctuates/oscillates for infinite time, neither the total energy nor the Fourier transform can be calculated. However, if we observe $x(t)$ in the limited time interval $-T<t<T$, the truncated variable $x_T(t)$ is given as

$$x_T(t)=\begin{cases} x(t) & , \ -T<t<T \\ 0 & , \text{ elsewhere.} \end{cases} \tag{4.12}$$

Now, the truncated variable can be Fourier transformed as usual,

$$X_T(f)=\int_{-\infty}^{\infty}x_T(t)e^{-j2\pi ft}\,dt=\int_{-T}^{T}x(t)e^{-j2\pi ft}\,dt. \tag{4.13}$$

By Parseval's theorem the energy of a signal is conserved in both time and frequency domain. The energy of $x(t)$ in the given time interval is given as

$$\epsilon=\int_{-T}^{T}|x(t)|^2dt=\int_{-\infty}^{\infty}\left|X_T(f)\right|^2df, \tag{4.14}$$

where $X_T(f)$ denotes the Fourier transform of $x_T(t)$. Since the energy of a stochastic process does not exist, we instead calculate the total average power (energy per time). The truncated $x_T(t)$ is observed during a time interval of length $2T$. If we then let $T\to\infty$, and introduce the expectation operator or ensemble average $E\{\cdot\}$, the total average power of $x(t)$ can be defined as

$$P=\lim_{T\to\infty}\frac{\int_{-T}^{T}E\left\{|x(t)|^2\right\}dt}{2T}=\int_{-\infty}^{\infty}\lim_{T\to\infty}\frac{E\left\{|X_T(f)|^2\right\}}{2T}df. \tag{4.15}$$

The integrand,

$$\lim_{T\to\infty}\frac{E\left\{|X_T(f)|^2\right\}}{2T}, \tag{4.16}$$

is obviously a density in the frequency domain, and it is called the power spectrum density (PSD). By expressing Eq. (4.16) in terms of $x(t)$ (see Eq. (4.13)), we obtain the fundamental definition of the PSD, denoted $S(f)$, for a stochastic signal

$$S(f) = \lim_{T\to\infty} E\left\{ \frac{1}{2T} \left| \int_{-T}^{T} x(t) e^{-j2\pi f t}\, dt \right|^2 \right\}. \tag{4.17}$$

The estimators of the power spectrum density in the following sections will be based the definition in Eq. (4.17).

4.4.2 Basic power spectrum estimators

We will now look at the basic estimators for the power spectrum density, the periodogram and the modified periodogram, following Hanssen [2003]. Other good sources are e.g., Percival and Walden [1993] and Shiavi [1999].

If we have N equally spaced samples $x[n]$ of $x(t)$, sampled every Δt, an estimator of the power spectrum density, can be derived from the definition in Eq. (4.17). We have to disregard the expectation operator since we know the values of $x[n]$ only for the finite time $2T$, now given by $2T = N\Delta t$. Furthermore, we also need to remove the $\lim_{T\to\infty}$ operator. Finally, we convert the Fourier transform to a Discrete Time Fourier transform (DTFT), given by $X(f) = \Delta t \sum_{n=0}^{N-1} x[n] e^{-j2\pi f n\Delta t}$. The basic estimator, called the periodogram, now becomes

$$\widehat{S}^{(per)}(f) = \frac{1}{N\Delta t} \left| X(f) \right|^2 = \frac{\Delta t}{N} \left| \sum_{n=0}^{N-1} x[n] e^{-j2\pi f n\Delta t} \right|^2 \quad ; \ |f| \le 1/(2\Delta t). \tag{4.18}$$

Before further discussion we first derive the expectation properties of the periodogram,

$$E\{\widehat{S}^{(per)}(f)\} = \frac{\Delta t}{N} \cdot E\left\{ \sum_{n=0}^{N-1} \sum_{m=0}^{N-1} x[n] e^{-j2\pi n\Delta t} x[m] e^{j2\pi n\Delta t} \right\}. \tag{4.19}$$

The expectation operator $E\{\cdot\}$ works only on the stochastic terms $x[n]$ and $x[m]$, giving $E\{x[n]x[m]\}$. This is equal to the autocorrelation function $R_{XX}[n,m]$. We then assume the data are from a wide sense stationary process, then $R_{XX}[n,m] = R_{xx}[n-m]$ and by the Wiener-Khinchin relation, the following can be replaced in Eq. (4.19)

$$E\{x[n]x[m]\} = R_{XX}[n-m] = \int_{-1/2\Delta t}^{1/2\Delta t} S(f') e^{j2\pi f'(n-m)\Delta t}\, df', \tag{4.20}$$

where $S(f)$ denotes the true spectrum. When inserting Eq. (4.20) into Eq. (4.19) we obtain

$$\begin{aligned} E\{\widehat{S}^{(per)}(f)\} &= \frac{\Delta t}{N}\int_{-1/2\Delta t}^{1/2\Delta t} S(f')\sum_{n=0}^{N-1} e^{-j2\pi(f-f')\Delta t}\sum_{m=0}^{N-1} e^{j2\pi m(f-f')\Delta t}\,df' \\ &= \frac{\Delta t}{N}\int_{-1/2\Delta t}^{1/2\Delta t} S(f')\left|\sum_{n=0}^{N-1} e^{-j2\pi(f-f')n\Delta t}\right|^2 df'. \end{aligned} \tag{4.21}$$

If we now gather the parts not containing the true spectrum $S(f)$, we get the fundamental Dirichlet kernel (Percival and Walden [1993]), here denoted $D(f)$

$$D(f) = \frac{\Delta t}{N}\left|\sum_{n=0}^{N-1} e^{-j2\pi(f)n\Delta t}\right|^2 = \frac{\Delta t}{N}\sum_{n=0}^{N-1} e^{-j2\pi n\Delta t}\sum_{m=0}^{N-1} e^{j2\pi m\Delta t} = \frac{\Delta t}{N}\frac{\sin^2(N\pi f\Delta t)}{\sin^2(\pi f\Delta t)}. \tag{4.22}$$

Returning to Eq. (4.21) we see that the expectation of the periodogram becomes a convolution between the Dirichlet kernel $D(f)$ and the true spectrum,

$$E\{\widehat{S}^{(per)}(f)\} = \int_{-1/2\Delta t}^{1/2\Delta t} D(f-f')S(f')df' = D(f) * S(f). \tag{4.23}$$

This is an important and fundamental result when discussing spectral estimators. The convolution results in a smoothing of the true spectrum and an unwanted smearing of the power. The Dirichlet kernel is shown in Figure 4.1. The main lobe, centred at $f = 0$ has a width of $2/N\Delta t$ and a main lobe side lobe ratio of 13 dB. The high levels of the side lobes cause spectral leakage, due to the convolution, where the power of the true spectrum leaks via the side lobes and causes a smoothing of the true spectrum. In general, peaked areas of the true spectrum will be underestimated, and low level regions will be overestimated. In particular, the spectral leakage from maxima of the true spectrum cause overestimated levels in frequency intervals were the true spectrum level is low, and peaks and features in these interval can be totally hidden in the estimate.

By the use of a window function that weights the samples of $x[n]$ in time domain, we can modify the Dirichlet kernel spectral properties, to achieve lower side lobes and better control of the bias of the estimate. This estimator is called the modified periodogram or windowed periodogram, and can be written as

$$\widehat{S}^{(w)}(f) = \frac{\Delta t}{NU}\left|\sum_{n=0}^{N-1} v[n]x[n]e^{-j2\pi f\Delta t}\right|^2. \tag{4.24}$$

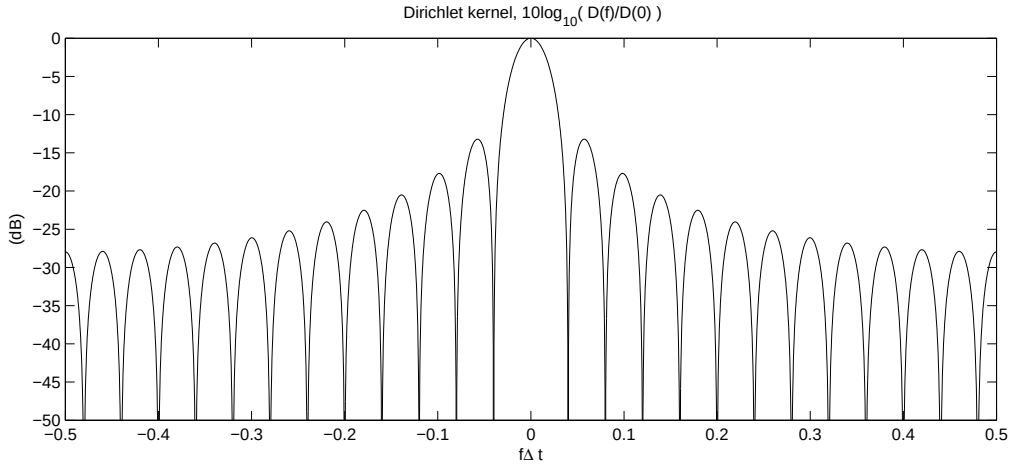

Figure 4.1: Dirichlet kernel, based on $N = 25$ samples.

Here, $v[n]$ denotes the window function, and $U = \sum_{n=0}^{N-1} v^2[n]/N$ is a normalisation factor that removes the energy introduced by the window function from the final estimate.

The expectation value can be calculated similarly as for the periodogram, but now also including the window function $v[n]$ (for the window function $v[n] = 1\ \forall n$, the modified periodogram equals the periodogram). When we sort the parts not including the true spectrum (similar to Eq. (4.22)), we now form the so-called spectral window $Q(f)$, where

$$Q(f) = \frac{\Delta t}{NU} \left| \sum_{n=0}^{N-1} v[n] e^{-j2\pi(f)n\Delta t} \right|^2 . \tag{4.25}$$

The expectation value is now given as the convolution between the spectral window $Q(f)$ and the true spectrum $S(f)$

$$E\{\widehat{S}^{(w)}(f)\} = \int_{-1/2\Delta t}^{1/2\Delta t} Q(f-f')S(f')df' = Q(f) * S(f). \tag{4.26}$$

The level of overestimation of the low level regions of the true spectrum depends on the side lobe levels of the spectral window. We understand that the properties of the spectral window $Q(f)$ have a considerable impact on the final estimate, and the result depends on our choice of the window function $v[n]$. By selecting a window with small side lobes, we are able to reduce the bias and spectral leakage, but there is always a price to pay. Less spectral leakage results in worse frequency resolution, and vice versa.

In the asymptotic limit ($N \to \infty$), it can be shown (e.g., Percival and Walden [1993](p.222)) that the variance of the periodogram and the modified periodogram can be approximated as

$$\mathrm{var}\left\{\widehat{S}^{(w)}(f)\right\} \approx S^2(f), \tag{4.27}$$

for $0 < f < f_{(N)}$, where $f_{(N)} = 1/(2\Delta t)$ is the Nyquist frequency . To summarise, the periodogram is generally biased, but by the use of a good window function, we are able to reduce the bias. Both the periodogram and windowed periodogram is inconsistent since the variance do not reduce when we increase N. The high variance makes these estimators less trustworthy, and no scientific conclusions should be made based on only one estimate using these "single-window" estimators.

4.5 Multitaper power spectrum estimation

The multitaper (MT), or multi window spectrum estimator is an extension of the "single-window" periodogram as given in Eq. (4.24). Thomson [1982] proposed to use several orthogonal window functions called discrete prolate spheroidal sequences (DPSS) to form several modified periodograms that can be applied on the same data. Averaging the modified periodograms, also called eigenspectra, results in an advantageous reduction of the variance.

4.5.1 Selecting the optimal window functions - discrete prolate spheroidal sequences

The windowed periodogram has been used to reduce the spectral leakage by the use of window functions (also called tapers) that manipulate the Dirichlet's kernel, and reduces the level of the sidelobes. The Hamming and Hanning windows are the most familiar, and they are just two examples out of the many windows that have been studied. The papers by Harris [1978], Nuttall [1981] and Kaiser and Schafer [1980] contain extensive research on the conventional window functions and their spectral properties.

Instead of studying the spectral properties of various more than less incidental windows to find the optimal window function, Slepian [1978] presented a different approach (for review see Slepian [1983]). He started out with some criteria which ensure that the window functions with the best leakage properties for a given frequency resolution can be derived. This is commonly called the concentration problem (e.g., Percival and Walden [1993]). The solution of

the problem is an eigenvalue equation, were the DPSS are the eigenvectors of the equation. The zeroth order DPSS is the window function that provide the best leakage properties (e.g., Eberhard [1973]). In the innovative paper by Thomson [1982], the properties of the DPSS were a central part of the derivation of the multitaper method, and Thomson proposed to use several of the DPSS obtained from the eigenvalue equation in spectrum estimation.

The eigenvalue equation defining the DPSS can be derived as follows:

1. The spectral concentration λ in the mainlobe should be maximised. For a user specified resolution bandwidth $2W$ (given in normalised frequency), the power in the mainlobe is given by $\int_{-W}^{W} Q(f)df$, and the total power of the spectral window is $\int_{-1/2}^{1/2} Q(f)df$. The spectral concentration can now be defined as the ratio between the energy in the mainlobe and the total energy,

$$\lambda = \frac{\int_{-W}^{W} Q(f)df}{\int_{-1/2}^{1/2} Q(f)df}. \tag{4.28}$$

   For an ideal choice of $Q(f)$, all the window energy will be located in the mainlobe and $\lambda = 1$.

2. The spectral window should be normalised $\sum_{n=0}^{N-1} v^2[n] = 1$. If we represent $v[n]$ as a vector $\mathbf{v} = [v_0, v_1, ...v_{N-1}]^T$, this can be expressed as $\mathbf{v}^T\mathbf{v} = 1$.

For simplicity we choose $\Delta t = 1$ in this section. Since the $v[n]$ is normalised, the scaling outside the absolute sign in Eq. (4.25), reduces to

$$U = 1/N \sum_{n=0}^{N-1} v^2[n] = 1/N,$$

and $\Delta t/NU = 1$. The purpose is now to find the window function $v[n]$ that maximises λ. We start by writing out Eq. (4.28) using definition Eq. (4.25). First, we consider the numerator

$$\begin{aligned}
\int_{-W}^{W} Q(f)df &= \int_{-W}^{W} \sum_{n=0}^{N-1} v[n]e^{-j2\pi fn} \sum_{m=0}^{N-1} v[m]e^{j2\pi fm} df \\
&= \sum_{n=0}^{N-1} v[n] \left(\int_{-W}^{W} e^{-j2\pi f(n-m)} \mathrm{df} \right) \sum_{m=0}^{N-1} v[m] \\
&= \sum_{n=0}^{N-1} v[n] \left(\frac{\sin(2\pi W[n-m])}{\pi[n-m]} \right) \sum_{m=0}^{N-1} v[m].
\end{aligned} \tag{4.29}$$

If we now use vector/matrix notation and define the matrix $\mathbf{A}$ as $[A]_{nm} = \sin(2\pi W[n-m])/\pi[n-m]$, the numerator can be written as

$$\int_{-W}^{W} Q(f)df = \mathbf{v}^T\mathbf{A}\,\mathbf{v}.$$

For the denominator, we derive the following expression,

$$\begin{aligned}\int_{-1/2}^{1/2} Q(f)df &= \sum_{n=0}^{N-1} v[n]\left(\int_{-1/2}^{1/2} e^{-j2\pi f(n-m)}\mathrm{df}\right)\sum_{m=0}^{N-1} v[m] \\ &= \sum_{n=0}^{N-1} v[n]\left(\frac{\sin[\pi(n-m)]}{\pi(n-m)}\right)\sum_{m=0}^{N-1} v[m] \\ &= \left(\sum_{n=0}^{N-1} v[n]\sum_{m=0}^{N-1} v[m]\right)\delta[n-m] \\ &= \sum_{n=0}^{N-1} w^2[n] = \mathbf{v}^T\mathbf{v}.\end{aligned} \tag{4.30}$$

Furthermore, we can now write Eq. (4.28) as

$$\lambda = \frac{\mathbf{v}^T\mathbf{A}\,\mathbf{v}}{\mathbf{v}^T\mathbf{v}}. \tag{4.31}$$

To find the sequence $\mathbf{v}$ that maximises λ, we need to differentiate λ with respect to $\mathbf{v}$ in the latter equation, to obtain the criterion

$$\frac{\partial\lambda}{\partial\mathbf{v}} = \mathbf{0} \implies \frac{2\mathbf{A}\,\mathbf{v}(\mathbf{v}^T\mathbf{v}) - (\mathbf{v}^T\mathbf{A}\,\mathbf{v})2\mathbf{v}}{(\mathbf{v}^T\mathbf{A}\,\mathbf{v})^2} = \mathbf{0}. \tag{4.32}$$

If we now insert $(\mathbf{v}^T\mathbf{A}\,\mathbf{v}) = \lambda(\mathbf{v}^T\mathbf{v})$ from Eq. (4.31), we obtain

$$\frac{2\mathbf{A}\,\mathbf{v}(\mathbf{v}^T\mathbf{v}) - \lambda(\mathbf{v}^T\mathbf{v})2\mathbf{v}}{(\mathbf{v}^T\mathbf{v})^2} = \mathbf{0}. \tag{4.33}$$

The above equation is true as long as the numerator is equal to the zero vector, and we then end up with the fundamental eigenvalue equation from which the window function $v[n]$ with the best leakage properties can be derived,

$$\mathbf{A}\,\mathbf{v} = \lambda\mathbf{v}. \tag{4.34}$$

For a matrix $\mathbf{A}$ of size $N \times N$ the eigenvalue equation will have N eigenvalues with corresponding $N \times 1$ eigenvectors, $(\lambda_0, \mathbf{v}_0), (\lambda_1, \mathbf{v}_1), ..(\lambda_{N-1}, \mathbf{v}_{N-1})$. The

eigenvalues λ_k simply represent the spectral concentration for the corresponding eigenvector $\mathbf{v}_k$, and will always be between 1 and 0 in the order,

$$1 \geq \lambda_0 \geq \lambda_1 \geq ... \geq \lambda_{N-1} \geq 0.$$

Since λ_0 is the largest eigenvalue, the corresponding eigenvector $\mathbf{v}_0$ has the greatest spectral concentration of all the eigenvectors, and hence the optimal leakage properties. The eigenvectors are orthogonal to each other, $\mathbf{v}_k^T \mathbf{v}_l = \delta[k-l]$, and named discrete prolate spheroidal sequences (DPSS), or Slepian sequences after the inventor.

For spectrum estimation, the DPSS provides a selection of orthogonal windows with optimal leakage properties, and the multitaper method was formed based on these windows (Thomson [1982]). To find the DPSS for a given length N and frequency resolution $2W$, Eq. (4.34) will have to be solved numerically. In Matlab, the function 'dpss' can be used, while Lees and Park [1995] provide C-subroutines for the purpose.

In Figure 4.2 the Dirichlet kernel, Hanning, Hamming and Kaiser window functions are plotted together with the zeroth-order DPSS ($k = 0$), and their respective normalised spectral windows $|V(f)/V(0)|^2$, where $V(f)$ denotes the DTFT of $v[n]$. For $n = 0, 1, \ldots, N-1$, the window functions are given by

$$\text{Dirichlet kernel: } v[n] = 1, \tag{4.35}$$

and (Nuttall [1981])

$$\text{Hanning: } v[n] = 0.5\left[1 - \cos\left(\frac{2\pi n}{N-1}\right)\right], \tag{4.36}$$

$$\text{Hamming: } v[n] = 0.54 - 0.46\cos\left(\frac{2\pi n}{N-1}\right), \tag{4.37}$$

and (Kaiser and Schafer [1980])

$$\text{Kaiser: } v[n] = \frac{I_0\left(\alpha\sqrt{1-\left(\frac{2\cdot n-(N-1)}{N-1}\right)^2}\right)}{I_0(\alpha)}. \tag{4.38}$$

Here, α is a design parameter which changes the shape of the window and I_0 is the modified Bessel function of first kind and zeroth-order, from Harris [1978], $I_0(x) = \sum_{k=0}^{\infty}\left[\frac{x^k}{2^k k!}\right]^2$. For the four latter windows the frequency resolution and the mainlobe width, denoted f_M, can be defined as twice the distance from $V(f=0)$ to the first zero-crossing. This implies the following mainlobe width

$$\text{Dirichlet kernel: } f_M = \frac{2}{N\Delta t},$$

from Nuttall [1981]

$$\text{Hanning and Hamming}: \quad f_M = \frac{4}{N\Delta t},$$

and from Kaiser and Schafer [1980]

$$\text{Kaiser}: \quad f_M = \frac{2}{\pi N\Delta t}\sqrt{\pi^2+\alpha^2}.$$

The equivalent main lobe width for the DPSS is given by the design parameter W, as $2W/(\Delta t)$, normally expressed through the normalised time-half bandwidth product NW, hence $f_M = 2W/\Delta t = 2NW/(N\Delta t)$. In Figure 4.2 the design parameters for the Kaiser window and the DPSS, is respectively $\alpha = \pi\sqrt{3}$ and $NW = 2$ to achieve the same resolution as the Hanning and Hamming window ($f_M = 4/(N\Delta t)$).

The low sidelobes of the zeroth order DPSS are clearly seen in Figure 4.2. In addition, we can also observe the tradeoff between low sidelobes and frequency resolution. For the window functions were the sidelobes are attenuated, we can see the mainlobe width increases compared to the Dirichlet kernel. A good window function has a low sidelobe next to the mainlobe, and a rapid decay of the following sidelobes, which reduces both the interference between adjacent and distant frequency components (e.g., Nuttall [1981]). As we can see from Figure 4.2, the Hanning window provides a rapid decay of the sidelobes, but with a high level of the sidelobe next to the mainlobe. The Hamming window provides the opposite, a low sidelobe next to the mainlobe but with less decay of the rest of the sidelobes. The Kaiser window and the DPSS, provides both a low sidelobe next to the mainlobe, and a rapid decay of the following sidelobes. The Kaiser window is actually an approximation of the zeroth order DPSS (Kaiser and Schafer [1980]), and we can see they have a similar shape, but where the DPSS has the lowest sidelobes.

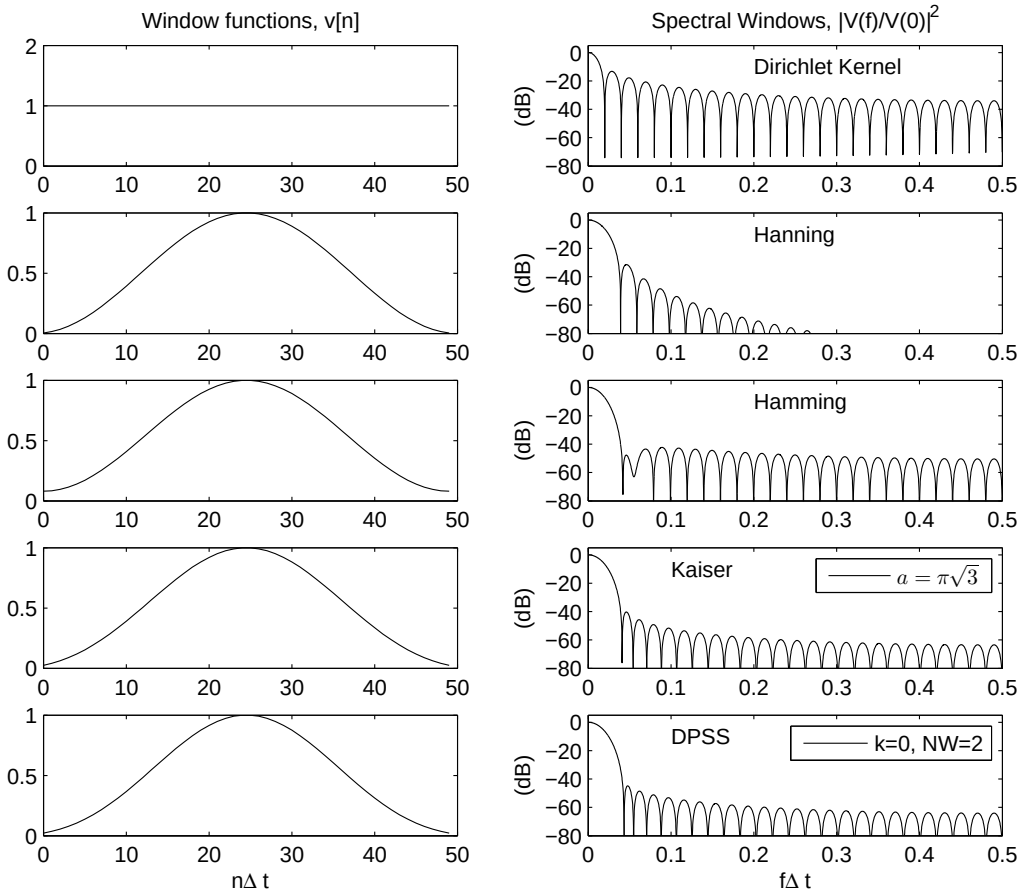

Figure 4.2: Plots of $N = 50$ samples of some well known window functions $v[n]$ (left panels) and their corresponding normalised spectral windows, $|V(f)/V(0)|^2$. From the top the respective windows are, Dirichlet's kernel, Hanning window, Hamming window, Kaiser window ($\alpha = \pi\sqrt{3}$) and the DPSS with the largest eigenvalue, $k = 0$, $NW = 2$. The design parameters for the Kaiser window and the DPSS are selected so the four latter spectral windows have the same mainlobe width of $f_M = 4/N\Delta t$.

4.5.2 The multitaper estimator

When solving Eq. (4.34), we are only interested in the DPSS (eigenvectors) with low spectral leakage. We therefore only select the eigenvectors with corresponding eigenvalue λ_k close to 1. It can be shown that the first eigenvalues are close to one, while the eigenvalues drop to almost 0 beyond the eigenvalue number $2NW$. To be sure to only use eigenvectors with low spectral leakage selecting the first $K = 2NW - 2$ DPSS, is usually safe (Percival and Walden [1993]). Thomson [1982] proposed to use the K first eigenvectors (DPSS) as window functions and calculate one modified periodogram for each of them, from now on called the eigenspectrum. The simplest multitaper (MT) estimator is the arithmetic average of all these eigenspectra (Thomson [1982])

$$\widehat{S}^{(MT)}(f) = \frac{1}{K}\sum_{k=0}^{K-1}\widehat{S}_k^{(MT)}(f;k). \tag{4.39}$$

The eigenspectrum of order k is denoted by $\widehat{S}_k^{(MT)}(f;k)$, and is given by

$$\widehat{S}_k^{(MT)}(f;k) = \Delta t\left|\sum_{n=0}^{N-1} v_k[n]x[n]e^{-j2\pi fn\Delta t}\right|^2, \tag{4.40}$$

were the window function v_k is the k'th order DPSS. It should be noted that the first eigenspectrum, $\widehat{S}_k^{(MT)}(f;0)$, is the estimate with the best leakage properties of all "single window" estimators with frequency resolution $2W$ (Eberhard [1973] and Thomson [1982]). As for the modified periodogram, the expectation value of the eigenspectrum results in a convolution between the spectral window and the true spectrum (Percival and Walden [1993](p.334))

$$E\left\{\widehat{S}_k^{(MT)}(f)\right\} = Q_k(f) * S(f), \tag{4.41}$$

where $Q_k(f)$ denotes the spectral window for the k'th DPSS, given by

$$Q_k(f) = \Delta t\left|\sum_{n=0}^{N-1} v_k[n]e^{-j2\pi fn\Delta t}\right|^2.$$

When we average the K eigenspectra, the expectation value for the multitaper estimate is given by

$$E\left\{\widehat{S}^{(MT)}(f)\right\} = \overline{Q}(f) * S(f), \tag{4.42}$$

were $\overline{Q}(f)$ denotes the average spectral window given by

$$\overline{Q}(f) = \frac{1}{K}\sum_{k=0}^{K-1} Q_k(f). \tag{4.43}$$

If $x[n]$ is sampled from a Gaussian zero mean process, the eigenspectra are approximately uncorrelated (as long as we select $K \leq 2NW$). This implies that the asymptotic variance ($N \rightarrow \infty$) can be approximated as (Percival and Walden [1993](p.351))

$$\text{var}\left\{\widehat{S}^{(MT)}(f)\right\} \approx \frac{1}{K^2}\sum_{k=0}^{K-1}\text{var}\left\{\widehat{S}_k^{(MT)}(f;k)\right\} \approx \frac{S^2(f)}{K}. \tag{4.44}$$

From Eq. (4.42) and (4.44) we understand that the multitaper method provides control of both the bias and of the variance reduction. By the use of the DPSS and a careful selection of K, we achieve a spectral window $\overline{Q}(f)$ with low side lobes and minimum amount of spectral leakage, and by averaging the eigenspectra we reduce the variance with a factor $1/K$ compared to the periodogram. For a fixed W, the number of K useable eigenspectra increase with N. Hence, the variance is reduced when we increases N, and the MT estimator is consistent (Thomson [1982]).

Another well known method used to reduce the variance is the weighted overlapped segment averaging (WOSA) (Welch [1967]). Here, single-window periodograms are applied to overlapping data segments, which are then averaged, hence the variance is reduced. Bronez [1992] compared WOSA and MT in terms of resolution bandwidth, leakage and variance. By holding two of the measures equal in both methods, he showed that the MT always performed better than WOSA on the last measure.

In this thesis we will consistently use the averaged multitaper method described above, and the DPSS window functions. It should be noted that the averaged MT can be further extended by adaptive weighting procedures (Thomson [1982] and e.g, Percival and Walden [1993](Ch.7.4)). In addition, the orthogonal sinusoidal window functions proposed by Riedel and Sidorenko [1995], can also be used as an alternative to the DPSS in multitaper estimation. The sinusoidal windows perform similar to the DPSS in many situations, and are less complicated to calculate.

Multitaper estimation example

As an example of the use of the multitaper estimator, we will now use data generated by an autoregressive model of order four (AR(4)), and compare the true spectrum of the AR(4) model, with the estimated results. The AR(4) model is given by

$$x[n] = 2.7607x[n-1] - 3.8106x[n-2] + 2.6535x[n-3] - 0.9238x[n-4] + \epsilon[n],$$

and is a frequently used test model, e.g., used in Percival and Walden [1993]. The driving noise, $\epsilon[n]$, is a Gaussian white noise process with zero mean and unity variance. For the example we use $N = 1024$ samples of the AR(4) process.

The resolution bandwidth of the DPSS is given by the design parameter $2W$. This is normally expressed indirectly by the time half-bandwidth product NW, and the resolution bandwidth is then given by $2NW/(N\Delta t)$. We now select $NW = 4$, and for $N = 1024$, this gives $W = 4/(1024\Delta t)$, and a frequency resolution about $0.008/\Delta t$. Here, we will calculate and evaluate all the $2NW = 8$ first DPSS, $v_k[n]$ for $k = 0, 1, ..., 7$. The window functions are shown in the left panels of Figure 4.3. Here we can see that only v_0 have the conventional bell shape, and number of zero crossings increases with increasing order k. In the middle panels of Figure 4.3, we have the AR(4) data weighted by the DPSS window functions ($v_k[n]x[n]$). As the order k increase, more of the data in the start and end of the time series are included. Hence, information lost by the zeroth-order DPSS will be recovered by the higher order DPSS, an advantage single windowed estimators do not have. The right panels of Figure 4.3 shows the eigenspectra for the respective DPSS (gray), and the true spectrum of the AR(4) process is given by the dashed line. For the eigenspectra of order $k = 5, 6$ and 7, the spectral leakage becomes prominent for frequencies around 0.2 and above, were we can clearly see the true spectrum is overestimated.

In Figure 4.4, we have the final multitaper estimates when $K = 1$ to $K = 8$ eigenspectra are applied. In the upper left panel, only the zeroth-order eigenspectra is included, and this is the single-windowed estimate with best leakage properties, but with no reduction of the variance, which explains the large fluctuation in this estimate. The variance reduces the more eigenspectra we average, and we can see the fluctuation reduces in the other panels for $K = 2$ to $K = 8$. For $K = 1$ to $K = 5$, the estimates do not indicate any spectral leakage. From $K = 6$ to $K = 8$, the spectral leakage increases, and the overestimation of the low region at the high frequencies increases. A proper choice for the final estimate seems to be the average of $K = 2NW - 3 = 5$ eigenspectra, given in the upper right panel of Figure 4.4. This estimate provides an acceptable reduction of the variance, and minimal evidence of spectral leakage.

In Figure 4.5, the spectral windows of the DPSS of orders $k = 0$ to $k = 7$ are shown in the left panels, which are the spectral windows for the corresponding order eigenspectra in Figure 4.3. The vertical line indicates the half-bandwidth frequency, $W = 4/(1024\Delta t)$. Here we see that the centre of the

main lobe moves to higher frequencies, and that the levels of the side lobes increase with increasing order k. We also note that $Q_k(f=0)=0$ for odd k. In the right panels of Figure 4.5 we have the spectral windows $\overline{Q}(f)$, corresponding to the average multitaper estimates in Figure 4.4. As we increase the number of averaged $Q_k(f)$, the level of the main lobe in $\overline{Q}(f)$ become closer to constant, and side lobe levels becomes higher.

To summarise, the best compromise between bias and variance properties for our example seems to be the multitaper estimate based on $K=5$ eigenspectra ($K=2NW-3$). The final result for this choice is given in the upper right panel of Figure 4.4, and the corresponding spectral window $\overline{Q}(f)$ is shown in Figure 4.5, from the top, the fifth of the right panels.

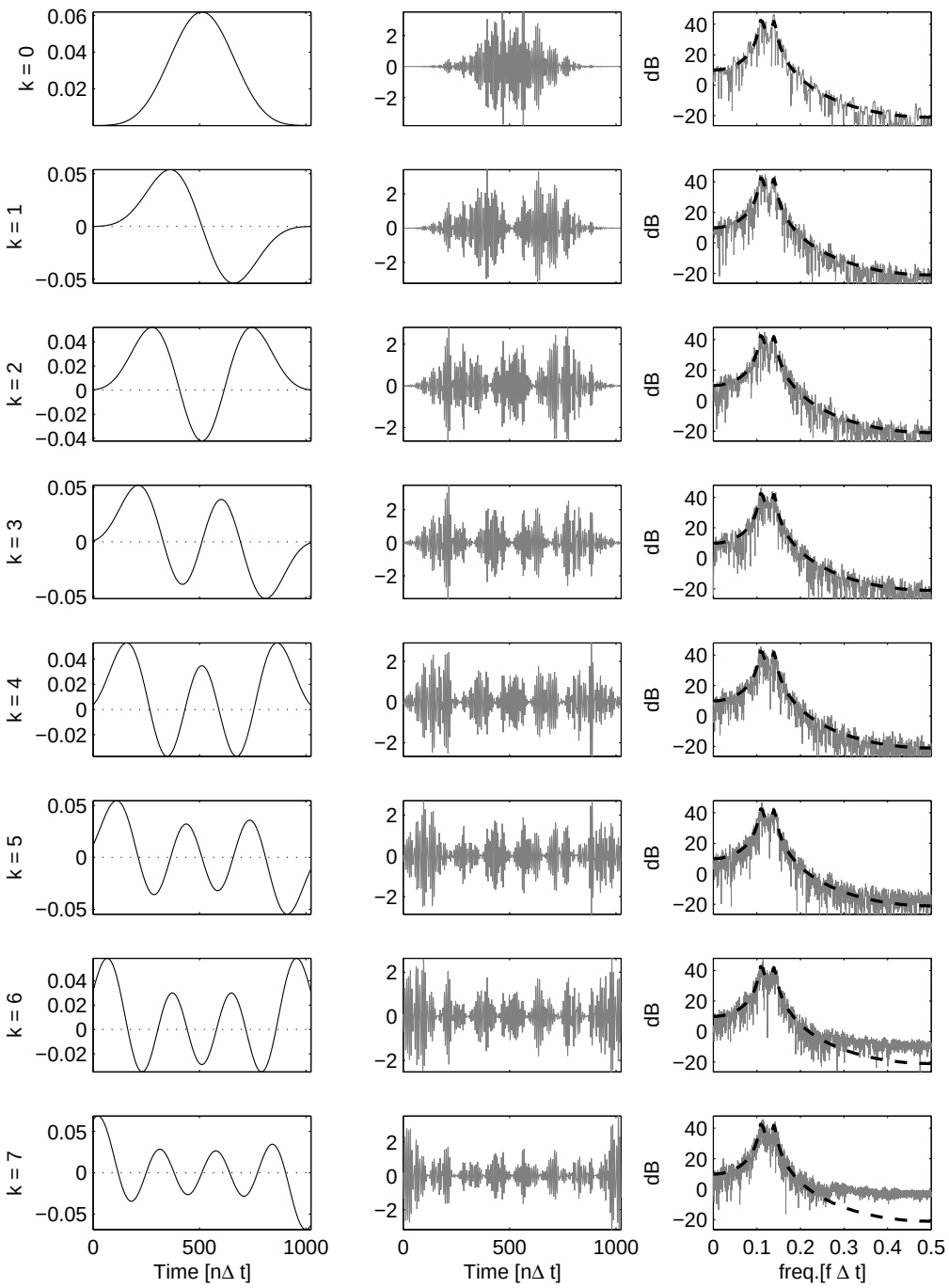

Figure 4.3: (1) Left panels display the DPSS, $v_k[n]$, for 1024 samples and $NW = 4$. (2) Middle panels display the product $v_k[n] \cdot x[n]$, which is fourier transformed for each eigenspectrum. (3) Right panels display the k'th eigenspectrum (gray) vs the exact spectrum of the AR(4) process (dashed). The upper to the lower panels correspond to $k = 0, 1, 2, 3, 4, 5, 6, 7$, respectively. The $x[n]$ data are generated by the AR(4) process defined in the text.

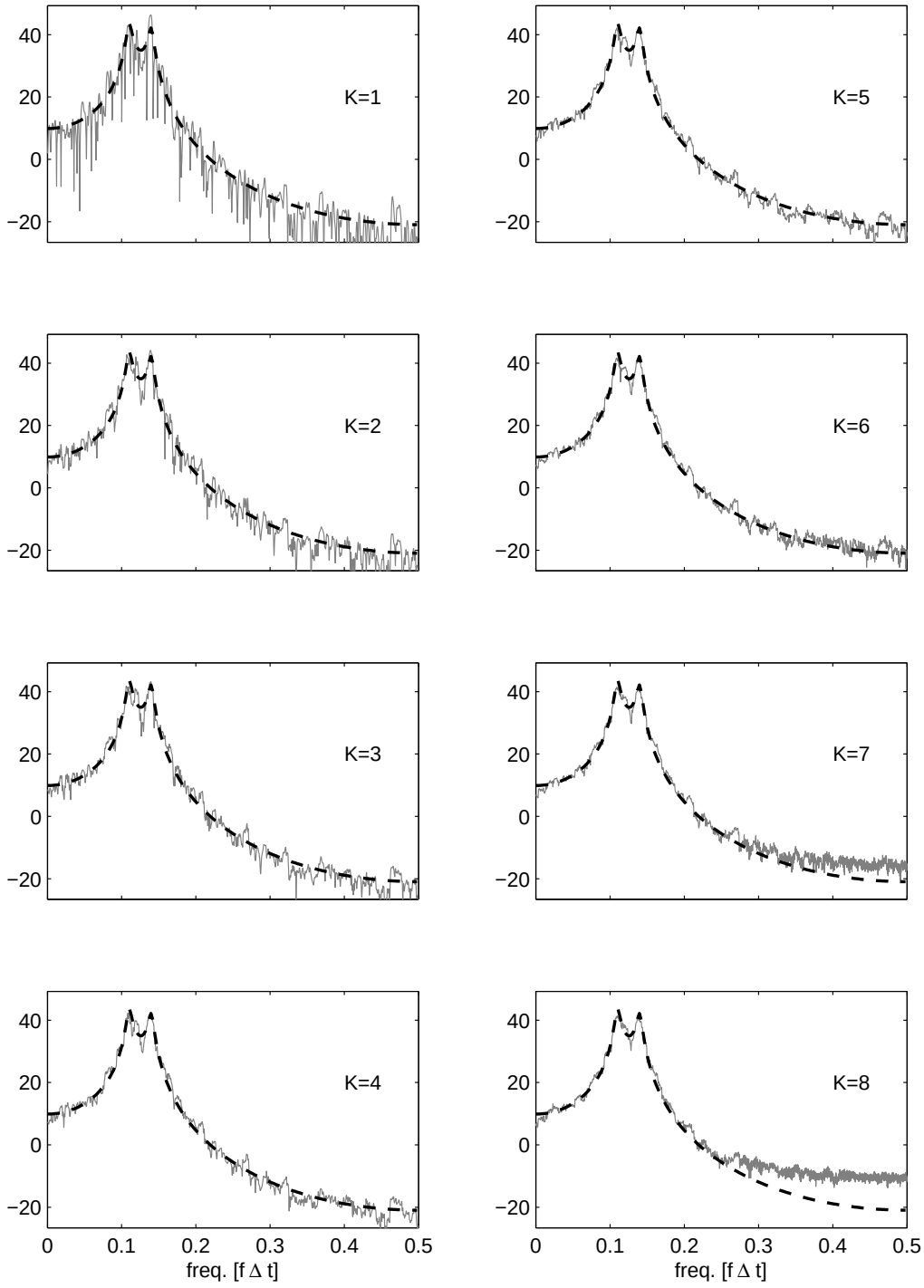

Figure 4.4: Multitaper estimates, $\widehat{S}^{(MT)}(f)$, based on the average of K eigenspectra (gray). From top and down, left panels show the average of K =1,2,3 and 4 eigenspectra respectively, and right panels the average of K =5,6,7 and 8 eigenspectra, respectively. The same AR(4) data as used in Figure 4.3 (1024 samples and $NW = 4$). The exact AR(4) spectrum is given by the dashed line.

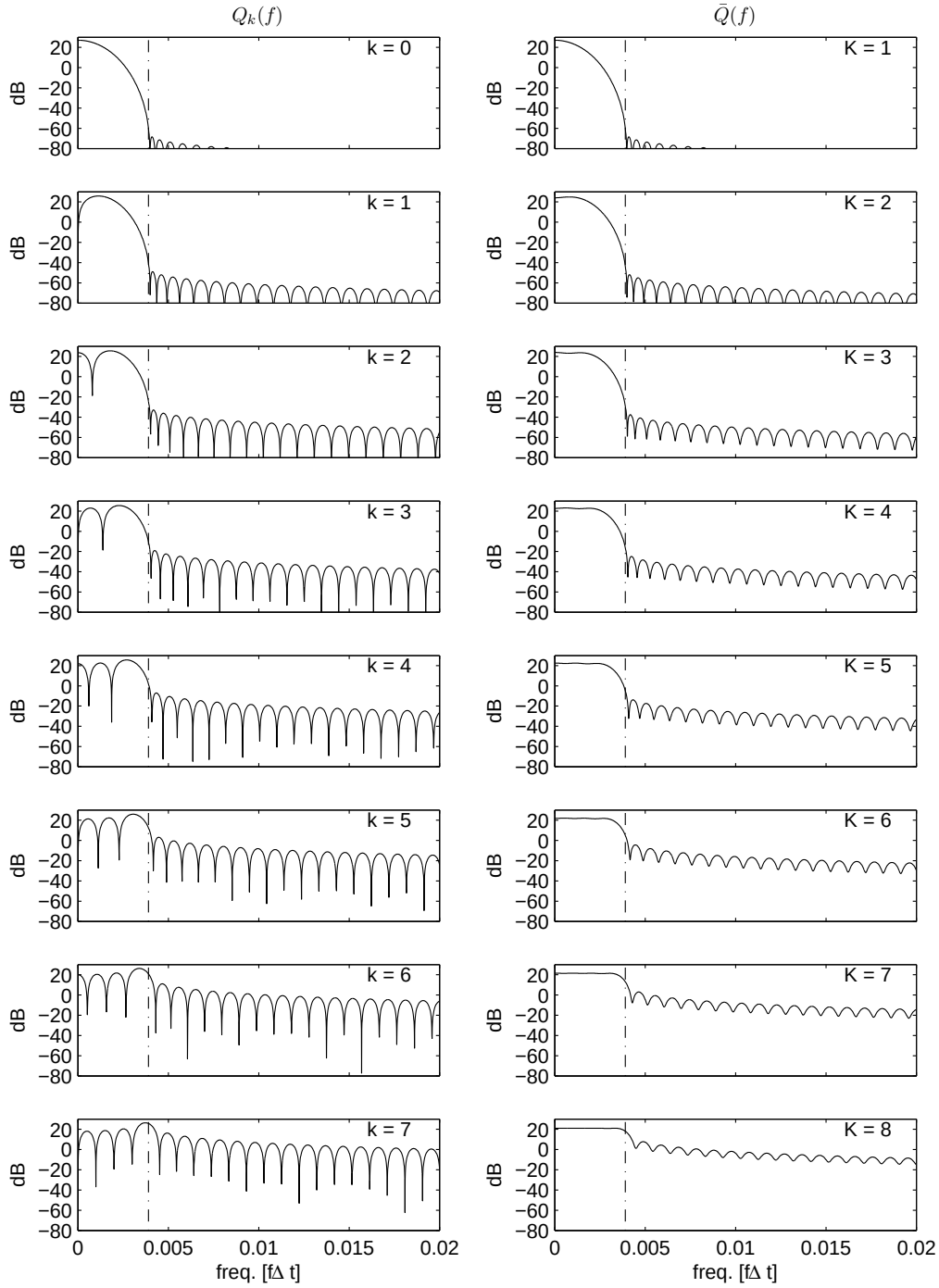

Figure 4.5: In the left panels, we show the spectral windows, $Q_k(f)$, for the k'th order DPSS, from the top, $k = 0,1,2,3,4,5,6,7$ respectively (1024 samples and $NW = 4$). These are the spectral windows for the respective eigenspectra in Figure 4.3. The spectral windows for the average multitaper estimates in Figure 4.4, are shown in the right panels and denoted $\overline{Q}(f)$. From top and down $K = 1,2,3,4,5,6,7,8$ respectively. The vertical line indicate the half-bandwidth W.

4.6 The chi-square and F-distributions

The chi-square distribution is important for computing confidence intervals for the spectrum estimators, while the F distribution will be used in a test to search for significant single sinusoidal frequencies in the spectrum. We will first define the distributions, and then use them in the following sections.

4.6.1 The chi-square distribution

If we have $Y_1, Y_2, ..., Y_\nu$ independent Gaussian random variables with zero mean and unity variance, then the sum of the square of the latter variables has a chi-square distribution, χ^2_ν, with ν degrees of freedom (e.g., Percival and Walden [1993]

$$\chi^2_\nu = Y_1^2 + Y_2^2 + ... + Y_\nu^2$$

The chi-square probability density function (PDF) is given by (e.g., Stark and Woods [2002])

$$f_X(x) = \begin{cases} \dfrac{x^{(\nu-2)/2} e^{-\nu/2}}{2^{\nu/2}\Gamma(\nu/2)} & \text{for } x > 0, \\ 0 & \text{for } x \leq 0, \end{cases} \tag{4.45}$$

where the Gamma function $\Gamma(\cdot)$ is defined as

$$\Gamma(\beta) = \int_0^\infty x^{(\beta-1)} e^{-x} \mathrm{dx} \quad \text{for } \beta > 0. \tag{4.46}$$

For β equal to a positive integer, i.e., when $\nu = 2K$ in Eq. (4.45), the Gamma function reduces to $(\beta-1)!$. The percentage point $Q_\nu(p)$ is found numerically (Matlab function 'chi2inv'), and related to the chi-square PDF, Eq. (4.45), as

$$p = \int_0^{Q_\nu(p)} f_X(x)\mathrm{dx}.$$

In Figure 4.6, the chi-square distribution is shown for different degrees of freedom. We can see that when the degrees of freedom increase, the distribution approach a more symmetric bell shape. The gray part of the curves start at the percentage point $Q_\nu(0.025)$, and end at the percentage point $Q_\nu(0.975)$, hence indicating the 95% confidence interval.

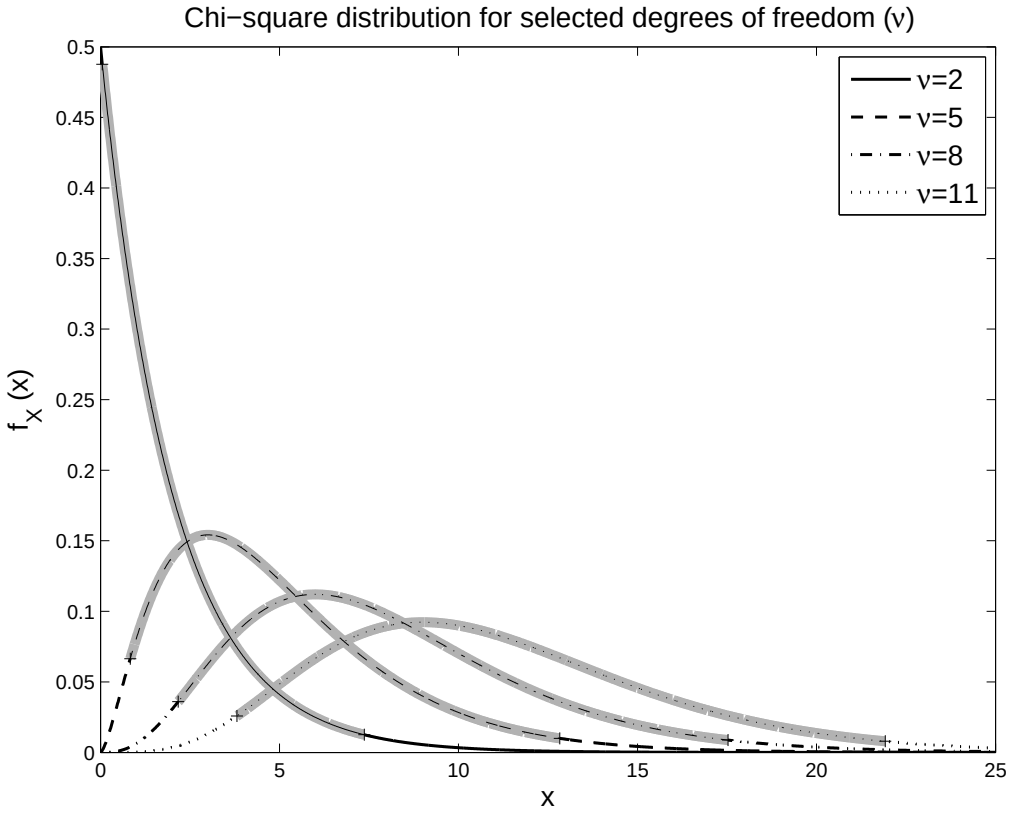

Figure 4.6: Plot of the chi-square distribution for a selection of degrees of freedom. The gray part of the curves start at the 2.5% percentage point $Q_\nu(0.025)$, and end at the upper 97.5% percentage point $Q_\nu(0.975)$. The area under the gray part represent the 95% of the total area under the curves.

4.6.2 The F-distribution

As described in Section 4.6.1, the sum of ν squared independent Gaussian variables with zero-mean and unity variance will have a χ^2_ν distribution. The F-test is defined as the ratio of two χ^2_ν variables, each divided by their degree of freedom (e.g., Bendat and Piersol [2000])

$$F_{\nu_1,\nu_2} = \frac{\chi^2_{\nu_1}/\nu_1}{\chi^2_{\nu_2}/\nu_2}, \tag{4.47}$$

where the ratio F_{ν_1,ν_2} is F-distributed and described by the degrees of freedom in both the χ^2_ν variables. This test can, e.g., be used to compare the variance of two data sets. The probability density function of the F-distribution is given by (e.g., Bendat and Piersol [2000])

$$f_X(x) = \begin{cases} \dfrac{\Gamma[(\nu_1+\nu_2)/2]}{\Gamma[\nu_1/2]\,\Gamma[\nu_2/2]} \dfrac{(\nu_1/\nu_2)^{\nu_1/2}\, x^{(\nu_1/2)-1}}{[1+(x\nu_1/\nu_2)]^{(\nu_1+\nu_2)/2}} & \text{for } x > 0, \\ 0 & \text{for } x \leq 0, \end{cases} \tag{4.48}$$

where $\Gamma(\cdot)$ is the Gamma function defined in Eq. (4.46). The percentage point $Q_{\nu_1,\nu_2}(p)$ for the $100p\%$ confidence limit is related to Eq. (4.48) as follows

$$p = \int_0^{Q_{\nu_1,\nu_2}(p)} f_X(x)\mathrm{dx}, \tag{4.49}$$

and can be found numerically with Matlab command 'finv'. For Thomson's F-test in Section 4.9, the test is one sided, meaning we are only interested in the upper percentage point where the calculated F_{ν_1,ν_2} value is greater than $Q_{\nu_1,\nu_2}(p)$. For this test the degrees of freedom in the numerator will also always be $\nu_1 = 2$ which in turn simplify the calculation of the upper $100p\%$ percentage point to (e.g., Percival and Walden [1993])

$$Q_{2,\nu_2}(p) = \frac{\nu_2[1-(1-p)^{2/\nu_2}]}{2(1-p)^{2/\nu_2}}. \tag{4.50}$$

Figure 4.7 displays the F-distribution for several ν_2 values (degrees of freedom in the denominator). The degrees of freedom in the numerator is fixed to $\nu_1 = 2$, since this will be the case in the F-test in Section 4.9. To better separate the lines, the function values are given on a logarithmic scale. From the upper percentage points, $Q_{2,\nu_2}(p)$, we can clearly see that when ν_2 increases the upper percentage point decreases, and the function approaches its asymptotic limit faster.

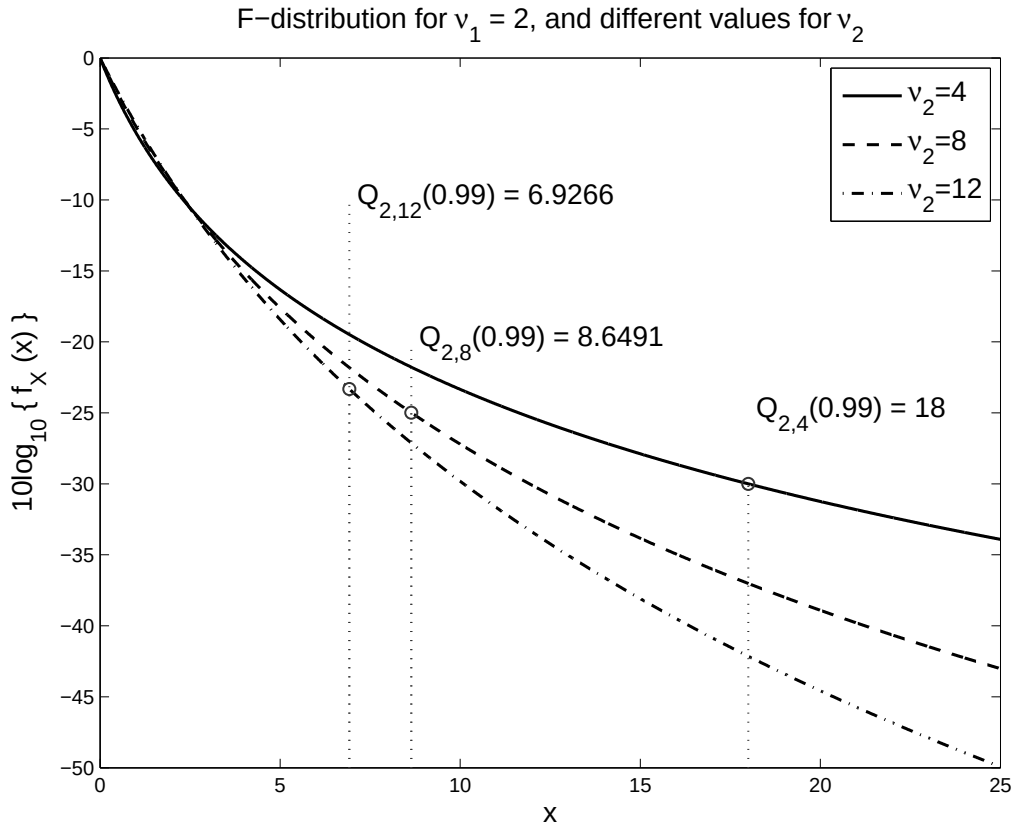

Figure 4.7: The F_{ν_1,ν_2} distribution for $\nu_1 = 2$, and $\nu_2 = 4,8$ and 12. The upper 99% percentage points are displayed for the respective values of ν_2.

4.7 Distribution of spectrum estimates

We will now follow the approach from Percival and Walden [1993] (p.220), and derive the probability distribution of the periodogram. To calculate the confidence intervals for the estimator, we need to know the distribution of the estimator. First we rewrite Eq. (4.18) to include the scaling inside the absolute sign,

$$\widehat{S}^{(per)}(f) = |J(f)|^2,$$

where $J(f)$ is given by

$$J(f) = \left(\frac{\Delta t}{N}\right)^{1/2} \sum_{n=0}^{N-1} G_x[n] e^{-j2\pi f n \Delta t}. \tag{4.51}$$

The observed data are now denoted $G_x[n]$ and assumed to be drawn from a Gaussian white process, with zero mean and $\text{var}\{G_x[n]\} = \sigma^2$. We then evaluate the real and imaginary parts $A(f)$ and $B(f)$, $J(f) = A(f) - jB(f)$, given by

$$\begin{aligned} A(f) &= \left(\frac{\Delta t}{N}\right)^{1/2} \sum_{n=0}^{N-1} G_x[n] \cos\left(2\pi f n \Delta t\right), \\ B(f) &= \left(\frac{\Delta t}{N}\right)^{1/2} \sum_{n=0}^{N-1} G_x[n] \sin\left(2\pi f n \Delta t\right). \end{aligned} \tag{4.52}$$

Since $G_x[n]$ is a Gaussian white process, also $A(f)$ and $B(f)$ will have zero mean,

$$E\left\{A(f)\right\} = \left(\frac{\Delta t}{N}\right)^{1/2} \sum_{n=0}^{N-1} E\left\{G_x[n]\right\} \cos\left(2\pi f n \Delta t\right) = E\left\{B(f)\right\} = 0. \tag{4.53}$$

The variance is given by

$$\begin{aligned} \text{var}\left\{A(f)\right\} = E\left\{A^2(f)\right\} &= \frac{\Delta t}{N} \sum_{n=0}^{N-1} E\{G_x^2[n]\} \cos^2(2\pi f n \Delta t), \\ &= \frac{\sigma^2 \Delta t}{N} \sum_{n=0}^{N-1} \cos^2(2\pi f n \Delta t) \\ \text{var}\{B(f)\} &= \frac{\Delta t}{N} \sum_{n=0}^{N-1} E\{G_x^2[n]\} \sin(2\pi f n \Delta t) \\ &= \frac{\sigma^2 \Delta t}{N} \sum_{n=0}^{N-1} \sin^2(2\pi f n \Delta t). \end{aligned} \tag{4.54}$$

If we now only evaluate the above equations for the standard frequencies, $f_m = m/N\Delta t$, where m is an integer, and excluding $f_m = 0$ and the Nyquist frequency $f_{(N)} = 1/(2\Delta t)$ we get

$$\begin{aligned} \text{var}\{A(f_m)\} &= \frac{\sigma^2\Delta t}{2} \\ \text{var}\{B(f_m)\} &= \frac{\sigma^2\Delta t}{2}. \end{aligned} \tag{4.55}$$

for $0 < f_m < f_{(N)}$ and $m = 1, 2, .., N-2$. Since $A(f_m)$ and $B(f_m)$ are orthogonal, they are also uncorrelated, and uncorrelated Gaussian random variables are also independent. The periodogram is given by

$$A^2(f_m) + B^2(f_m) = \widehat{S}^{(per)}(f_m).$$

If we scale $A(f_m)$ and $B(f_m)$ with $(2/\sigma^2\Delta t)^{1/2}$ the scaled periodogram is then a sum of two squared independent random variables with zero mean and unit variance, and hence, chi-square distributed, with 2 degrees of freedom,

$$(\frac{2}{\sigma^2\Delta t})\widehat{S}^{(per)}(f_m) \stackrel{d}{=} \chi_2^2 \quad => \quad \widehat{S}^{(per)}(f_m) \stackrel{d}{=} \frac{\sigma^2\Delta t}{2}\chi_2^2, \tag{4.56}$$

where $\stackrel{d}{=}$, denotes equality in distribution. The spectrum for a sampled white Gaussian process is $S(f) = \sigma^2\Delta t$ and hence we can replace the scaling in Eq. (4.56) with the true spectrum

$$\widehat{S}^{(per)}(f_m) \stackrel{d}{=} \frac{S(f)}{2}\chi_2^2. \tag{4.57}$$

If the observed data are stationary (not necessary white noise or Gaussian distributed) and the true spectrum is continuous on the interval $[-f_{(N)}, f_{(N)}]$, each eigenspectrum $\widehat{S}_k^{(MT)}(f)$ is asymptotically distributed as

$$\widehat{S}_k^{(MT)}(f) \stackrel{d}{=} \frac{S(f)}{2}\chi_2^2, \quad 0 < f < f_{(N)}. \tag{4.58}$$

The average multitaper estimate is an average of K approximately uncorrelated eigenspectra, each with $\nu = 2$ degrees of freedom, and hence has $2K$ degrees of freedom. In the asymptotically limit this estimate is distributed as a scaled chi-square distribution with $2K$ degrees of freedom,

$$\widehat{S}^{(MT)}(f) \stackrel{d}{=} \frac{S(f)}{2K}\chi_{2K}^2, \quad 0 < f < f_{(N)}. \tag{4.59}$$

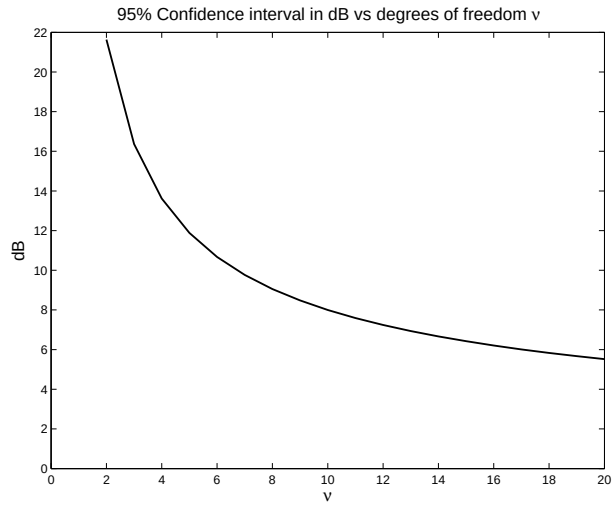

Figure 4.8: The width of the 95% confidence interval $10\log_{10}(\frac{Q_\nu(1-p)}{Q_\nu(p)})$ for different degrees of freedom ν.

4.8 Confidence interval of the multitaper spectral estimate

Based on Eq. (4.59) and the assumption that the observed data are stationary, and that the true spectrum is continuous, we can compute an approximate confidence interval of the true spectrum based on the estimated $\widehat{S}^{(MT)}(f)$, given in dB (Percival and Walden [1993])

$$10\log_{10}\frac{\nu}{Q_\nu(1-p)}+10\log_{10}\widehat{S}^{(MT)}(f) \leq 10\log_{10}S(f) \leq 10\log_{10}\frac{\nu}{Q_\nu(p)}+10\log_{10}\widehat{S}^{(MT)}(f),$$

for a significance level of $100(1-2p)\%$. Here, $Q_\nu(p)$ is the percentage points of the χ^2_ν distribution for a given degree of freedom ν.

The width of the confidence interval is clearly given by $10\log_{10}(\frac{Q_\nu(1-p)}{Q_\nu(p)})$, and in Figure 4.8 we can see this width decrease when we increase ν. The degrees of freedom in the above equations is given by the degrees of freedom of the estimator. From Eq. (4.59) we know the degrees of freedom for the multitaper estimator is $\nu = 2K$, and hence the confidence interval for the true spectrum $10\log_{10}(S(f))$ will decrease when we increase the number of K averaged eigenspectra.

4.9 Thomson's F-test for single frequency components

To test the observed data for spectral lines (sinusoidal components), Thomson [1982] proposed a F-test to check the significance of possible present single frequency components. We will now describe the test, closely following the approach from Percival and Walden [1993](p.496).

The observed data are now assumed to contain one sinusoidal components at a given frequency f_i

$$X_S[n] = D_i \cos(2\pi f_i n\Delta t + \phi_i) + \epsilon[n]. \tag{4.60}$$

Here, the part $\epsilon[n]$ represents the background noise, assumed to have a continuous spectrum, and is "locally white" in the frequency band $[f_i - W, f_i + W]$. We recall that $2W$ is the width of the mainlobe of the spectral window when using the multitaper method with DPSS windows. For a given frequency, the expectation value of the observed data equals the sinusoidal part,

$$E\{X_S[n]\} = D_i \cos(2\pi f_i n\Delta t + \phi_i) = C_i e^{i2\pi f_i n\Delta t} + C_i^* e^{-i2\pi f_i n\Delta t},$$

where * denotes the complex conjugate, and $C_i = (D_i/2)e^{i\phi_i}$. The observed data can then be written as $X_S[n] = E\{X_S[n]\} + \epsilon[n]$.

We rewrite the eigenspectrum from Eq. (4.40), and include the scaling in the absolute sign

$$\widehat{S}_k(f) = \left|J_k(f)\right|^2,$$

where we define $J_k(f)$ as

$$J_k(f) = (\Delta t)^{1/2} \sum_{n=0}^{N-1} v_k[n] X_S[n] e^{-i2\pi f n\Delta t}, \tag{4.61}$$

where $v_k[n]$ is the k'th order DPSS window function. For $f = f_i$ and $2f_i > W$, $J_k(f_i)$ can be approximated as

$$J_k(f_i) \approx C_i \frac{V_k(0)}{(\Delta t)^{1/2}} + (\Delta t)^{1/2} \sum_{n=0}^{N-1} v_k[n]\epsilon[n] e^{-i2\pi f_i n\Delta t}, \tag{4.62}$$

where $V_k(f)$ is the discrete time Fourier transform of the k'th order DPSS function $V_k(f) = \Delta t \sum_{n=0}^{N-1} v_k[n] e^{-i2\pi f n\Delta t}$. The first term in Eq. (4.62) is the contribution from the sinusoidal component, and the last term represents the background noise, which is the nature of the true background spectrum, denoted

by $S_\epsilon(f)$.

By linear regression an estimator of C_i can be found as

$$\widehat{C_i} = (\Delta t)^{1/2} \frac{\sum_{k=0}^{K-1} J_k(f_i) V_k(0)}{\sum_{k=0}^{K-1} V_k^2(0)}. \tag{4.63}$$

Under the null hypothesis, $\widehat{C_i}(f_i)$ is assumed to be a zero mean complex Gaussian variable, and $|\widehat{C_i}(f_i)|^2$ will be a sum of two squared independent variables, were each part has the variance $S_\epsilon(f_i)\Delta t/2\sum_{k=0}^{K-1} V_k^2(0)$. A scaled $|\widehat{C_i}(f_i)|^2$ variable will then follow a chi-square distribution with 2 degrees of freedom

$$\frac{2|\widehat{C_i}|^2 \sum_{k=0}^{K-1} V_k^2(0)}{S_\epsilon(f_i)\Delta t} \stackrel{d}{=} \chi_2^2. \tag{4.64}$$

We can now form an estimate of the background spectrum by subtracting the contribution from the sinusoidal part in Eq. (4.62), using the estimated $\widehat{C_i}$, and perform a multitaper estimate on the residuals

$$\widehat{S}_\epsilon^{(MT)}(f_i) = \frac{1}{K} \sum_{k=0}^{K-1} \left| J_k(f_i) - \widehat{C_i} \frac{V_k(0)}{(\Delta t)^{1/2}} \right|^2. \tag{4.65}$$

As given in Eq. (4.59), the multitaper estimate has a scaled chi-square distribution with $2K$ degrees of freedom, but the subtraction including $\widehat{C}_i$ in Eq. (4.65) reduces the sum of squared independent variables by 2. The scaled variable $\widehat{S}_\epsilon^{(MT)}(f_i)$ therefore follows a chi-square distribution with $2K-2$ degrees of freedom,

$$\frac{2K\widehat{S}_\epsilon^{(MT)}(f_i)}{S_\epsilon(f_i)} = \frac{2\sum_{k=0}^{K-1} \left| J_k(f_i) - \widehat{C_i} \frac{V_k(0)}{(\Delta t)^{1/2}} \right|^2}{S_\epsilon(f_i)} \stackrel{d}{=} \chi_{2K-2}^2. \tag{4.66}$$

Finally, the F-test proposed by Thomson is formed by the ratio between the two chi-square variables in Eq. (4.64) and Eq. (4.66), divided by their respective degrees of freedom, giving a new F-distributed variable with 2 and $2K-2$ degrees of freedom, respectively:

$$\frac{\frac{2|\widehat{C_i}|^2 \sum_{k=0}^{K-1} V_k^2(0)}{S_\epsilon(f_i)\Delta t}/2}{\frac{2K\widehat{S}_\epsilon^{(MT)}(f_i)}{S_\epsilon(f_i)}/(2K-2)} \stackrel{d}{=} F_{2,2K-2}.$$

Rearranging, the basic quantity that should be calculated is given by

$$F(f_i) = \frac{(K-1)\left|\widehat{C_i}\right|^2 \sum_{k=0}^{K-1} V_k^2(0)}{\Delta t \sum_{k=0}^{K-1} \left| J_k(f_i) - \widehat{C_i} \frac{V_k(0)}{(\Delta t)^{1/2}} \right|^2}. \tag{4.67}$$

Under the null hypothesis, no sinusoidal component exists at f_i, and $C_i = 0$. This is rejected if $F(f_i)$ is above the upper percentage point (e.g., 99%) of the $F_{2,2K-2}$ distribution, and a sinusoidal component is detected. It is important to note that the test will fail detecting the sinusoidal components if several sinusoidal components are present in the range $[f_i - W \leq f \leq f_i + W]$. Hence, we may encounter problems if the signal is a narrow band signal (amplitude and phase modulated), or if the background spectrum is changing rapidly in the bandwidth of interest.

If a sinusoid is found significant at a given f_i, Thomson [1982] proposed to reshape the spectrum in the region $[f_i - W \leq f \leq f_i + W]$ to estimate the background spectrum according to

$$\widehat{S}_{\epsilon}^{(MT)}(f) = \frac{1}{K}\sum_{k=0}^{K-1}\left|J_k(f) - \widehat{C}_i\frac{V_k(f-f_i)}{(\Delta t)^{1/2}}\right|^2. \tag{4.68}$$

4.9.1 Numerical example

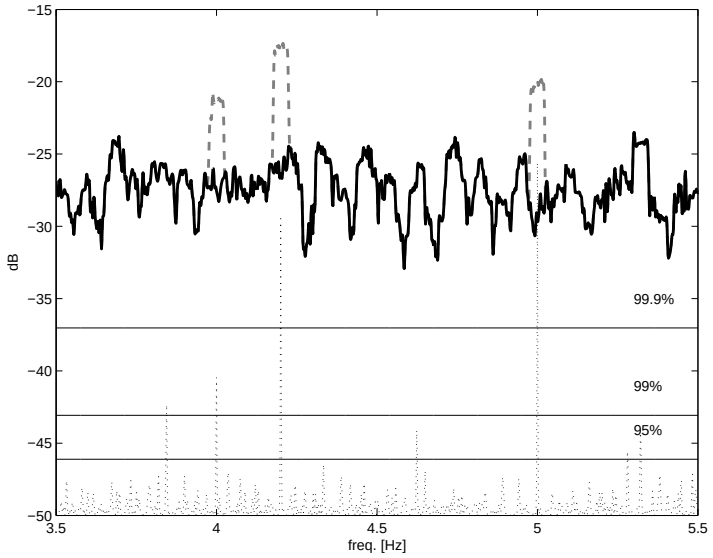

Figure 4.9: Reshaped spectrum (black), original spectrum (dashed gray), F-test values (dotted gray). The horizontal lines show the 99.9%, 99% and 95% limits for the F-test, from top to bottom, respectively.

To verify the implemented F-test numerically, we generated a data set of 90000 samples of a weighted sum of three sinusoidal components embedded in additive white Gaussian noise. The numerical data were generated according

to

$$x[n] = 0.03\sin[2\pi 4n\Delta t + (\pi/3)] + 0.05\cos[2\pi 4.2n\Delta t] + 0.04\sin[2\pi 5n\Delta t] + \epsilon[n],$$

where $\Delta t = 1/500$, and $\epsilon[n]$ is Gaussian white noise with zero mean and unit variance. As an additional measure (Lees [1995]), we also evaluated the power level at the frequencies found significant with the F-test, before we decided to reshape and remove the power from the sinusoidal. For frequencies with F-values above the 99% confidence limit, we checked whether the level at the given frequency was more than 5 standard deviations above the mean of the "flat" estimated spectrum. For both the spectrum estimate and the F-test the frequency resolution was chosen to be $NW = 5$, and 7 DPSS tapers were used.

The F-values calculated with Eq. (4.67) are given in Figure 4.9, together with the original estimated spectrum and the reshaped spectrum (the F-values are scaled to overlap the spectrum values). The black dotted line gives the F-values, and the three sinusoidal components (at 4.0, 4.2 and 5.0 Hz) are all above the 99% confidence limit, given by the middle horizontal line. The spectrum power were 5 standard deviations above the mean, and hence we reshaped the spectrum around these frequencies. The bold black line are the reshaped spectrum, and the gray dotted line are the parts of the original spectrum removed after reshaping. Also at around 3.8 Hz, the F-value are above the 99% limit, but a sinusoidal component were rejected because of low power in the spectrum at the given frequency. Therefore no reshaping were done here.

Chapter 5

Results

5.1 E-field measurements: 50 m cable antenna, Station 1

The following analysis will be conducted on data from the vertical electric field measured by the 50 m long cable antenna located at Station 1 (see Figure 3.2). A total of 900000 samples were recorded at the sampling rate $f_s = 500$ Hz, giving a total of 30 minutes of data. As the antenna actually measured the voltage between the electrodes, the electric field were obtained by dividing the voltage by the length of the cable. Hence, the source of the motion induced electric field is the average apparent water velocity between the electrodes. Since we are interested in the fluctuation of the E-field in the range 0.1-10 Hz, the overall sample mean was removed before further analysis ($\overline{x} = -22.8\ \mu$V/m). Note that the DC-level for the electrode pair was not absolutely calibrated (Blixt [2007]), and we will not relate this mean level to the mean water velocity (East-West).

5.1.1 Time series

The time series of the analysed data is given in Figure 5.1. Two main features are observed, an overall trend, and a prominent oscillation with a modulated amplitude. The first minute of the data is plotted in the upper right corner, and clearly shows the oscillation. Here we can also count about 9 cycles during the 60 seconds, giving an oscillation frequency about 0.15 Hz and period $T \approx 6.7$ s.

We received weather data from a nearby platform (Meteorologisk institutt [2007]), and during the electric field recordings, the average frequency of the surface

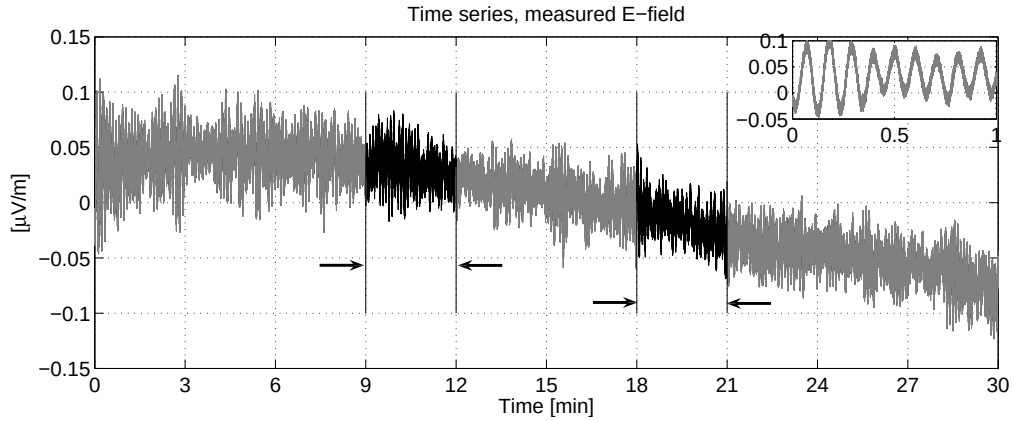

Figure 5.1: Time series of E-field data from the 50 m cable antenna, Station 1. The small figure in the upper right corner, is a zoomed in view of the first minute. Sections enclosed by the arrows indicate the segments failing the runs test.

waves was also about 0.15 Hz ($T \approx 6.8$ s). Hence, the frequency of the main oscillation in the electric field corresponds well with the surface waves.

5.1.2 E-field runs test

The data set was divided into 10 non-overlapping segments of 90000 samples, and the runs test outlined in Section 4.3.1 was applied individual to each segment to check for local randomness and nonstationarity. The estimation in Section 5.1.4 will also be based on the same segments.

For each segment the runs test were used to evaluate the sample mean and variance. Both subset length of 7500 and 9000 samples were used, giving run sequences of $N_s = 12$ and $N_s = 10$ respectively. It is vital to select the subset length long enough to resolve at least two cycles of a dominating oscillation. We have an oscillation at $T \approx 6.7$ s. In seconds, our subset lengths correspond to 15 s (7500 samples) and 18 s (9000 samples), and the subset of 7500 samples barely cover two cycles.

The hypotesis is that there is no trends in the data. We used a confidence interval of 95%, and for the subset length of 7500 samples the hypotesis was rejected for the data between $9-12$ minutes. Here, the number of runs for the variance was too low, indicating a trend in the amplitude variation. Between $18-21$ minutes number of runs for the mean was to low, indicating a trend in the mean. Here, the hypotesis was rejected for both subset lengths of 7500 and 9000 samples. The two segments are enclosed by arrows in Figure 5.1,

and flagged as nonstationary according to this test.

5.1.3 Multitaper estimation, number of averaged eigenspectra

In Figure 5.2, we have plotted the average multitaper estimates for different number of K eigenspectra, based on the first 90000 samples of the E-field data from the 50 m cable antenna (Station 1). Here, $NW = 4$, giving 8 DPSS tapers with eigenvalues close to one, and 8 potentially useable eigenspectra. The multitaper estimates are plotted in black, and the gray lines in the figure represent the 95% confidence interval. Hence, with 95% confidence the true spectrum is located within the gray lines. As we average more eigenspectra, we can clearly see this interval shrinks, which gives a good visualisation of the variance reduction provided by the multitaper method. For $K = 7$ and $K = 8$, leakage from the peak at around 0.15 Hz becomes prominent, resulting in overestimated levels from 0.2 Hz and above. Also for $K = 6$, there is potential spectral leakage problems, but the average of $K = 5$ eigenspectra show no sign of spectral leakage, and still provides a good reduction of the variance. As a compromise between good bias and variance properties, the multitaper estimates in the following sections will therefore be based on the average of $K = 2NW - 3$ eigenspectra.

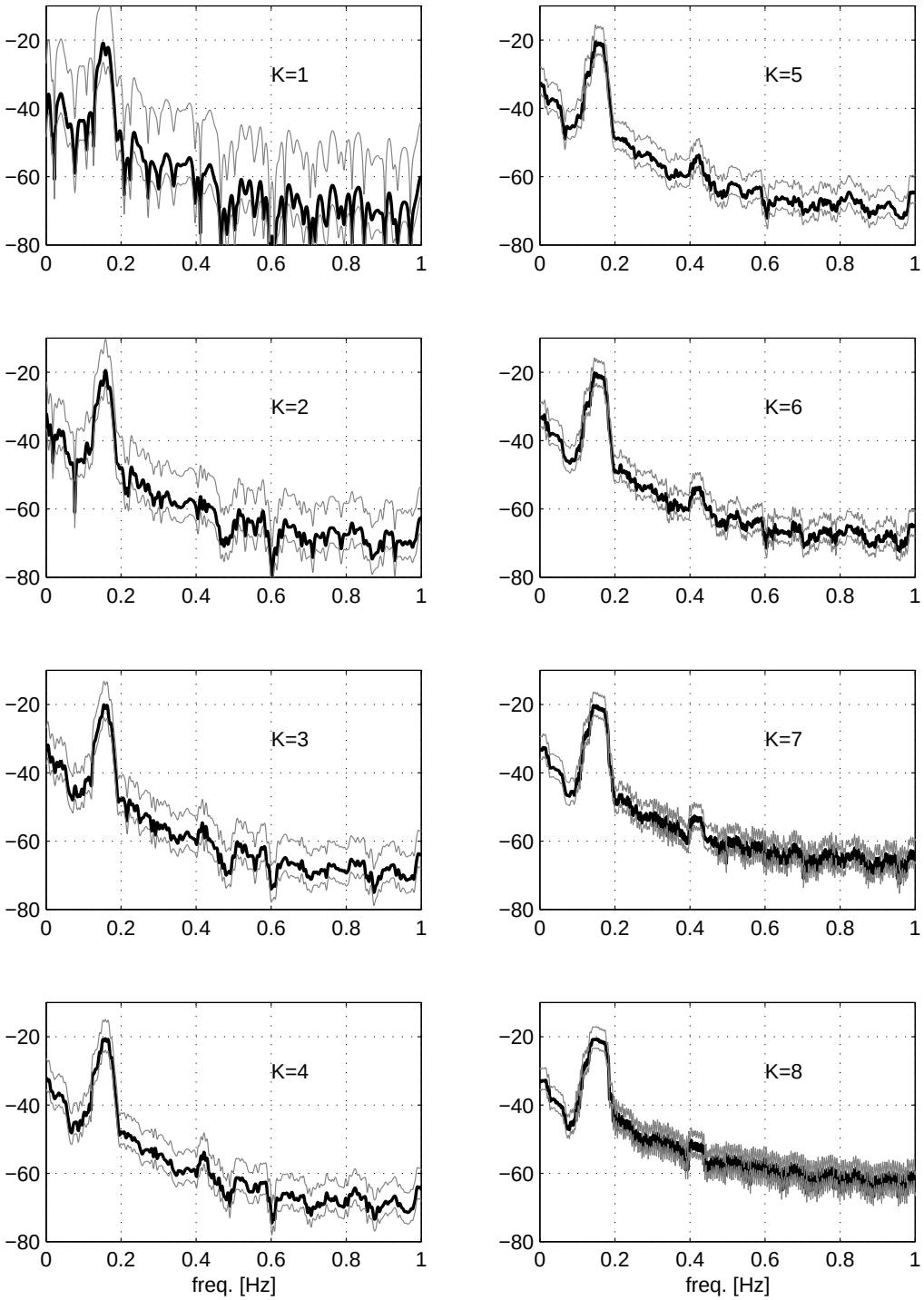

Figure 5.2: Multitaper spectrum estimates, $NW = 4$, for different number of K averaged eigenspectra. The left panels shows the average of $K = 1, 2, 3, 4$ eigenspectra, and the right panels shows the average of $K = 5, 6, 7$ and 8. The 95% confidence interval is located between the gray lines.

5.1.4 Time series, spectral estimates and probability density function estimates

To study the development of the vertical electric field with time, the analysis in this Section is based on 3 minutes long data segments ($N = 90000$ samples). The power spectrum density (PSD) and the probability density function (PDF) were estimated by the methods outlined in Section 4.5.2 and 4.2 respectively. The multitaper method is more robust against nonstationary data than single windowed methods, and the time length of the used data segments are also short. Therefore, also the segments found nonstationary in Section 5.1.2, will be included in this analysis. The region of interest is 0.1-10 Hz, and the spectrum estimates in this section only displays the interval between 0-10 Hz.

The time series with the sample mean removed are presented in Figure 5.3, 5.4, 5.5, 5.6 and 5.7, together with spectrum estimates and PDF estimates for each segment. Here, each figure contains results for two segments, one in each column. The upper panels displays the time series of the evaluated data, and the corresponding estimates are aligned below the time series plot. The spectrum estimates are given in the first and second panels below the time series panel, where the uppermost of them gives a zoomed view of the range $0-1$ Hz, and the next shows the $0-10$ Hz range. To reveal consistent features in the spectrum estimates, several MT estimates with different frequency resolution were applied and plotted. Here, $NW = 3,4,5$ were used and given in Hz, the respective frequency resolutions are approximately 0.033, 0.044 and 0.056 Hz. The number of averaged eigenspectra were $K = 3,5,7$ respectively. The bottom panels show the estimated probability density functions. For each data segment, three estimates with different binwidth b of the Gaussian kernel (see Eq. (4.8)) are plotted in black. Here, b denotes the binwidth given in Eq. (4.9) and the respective binwidths are b, $2b$ and $0.1b$. For reference, a Gaussian distribution function shaped by the sample mean ($\overline{x}$) and the standard deviation ($\widehat{\sigma}$) of the evaluated data is plotted (solid gray) together with the PDF estimates.

From the time series the most prominent oscillation is clearly visible. By counting the cycles in Figure 5.1, we found this oscillation to be around 0.15 Hz. In the 0-1 Hz spectrum estimates in Figure 5.3, 5.4, 5.5, 5.6 and 5.7, the main peak has its maximum around 0.15 Hz for all the time intervals, but we can see the peakiness, width and level changing during time. Between 0-3 minutes the peak is at its maximum, between 3-9 minutes the peak gets wider with a lower maximum. The oscillation amplitude variations seen in the time series, and the changes in the width of the corresponding peak in the spectrum estimate,

indicates that the oscillation is not sinusoidal, but rather an amplitude and possibly a phase modulated narrow band signal. From 9-30 minutes additional local maxima are developed around the main peak, seen as a shoulder just above 0.1 Hz, and a feature just below 0.25 Hz which develops into a separate peak between 24-27 minutes, seen in Figure 5.7. We also observe a consistent local maximum at just above 0.4 Hz. In the 0-10 Hz plot consistent peaks are observed at 2, 4 and 5 Hz for all time intervals. Peaks around 6 Hz are most evident in Figure 5.4 and 5.5.

While the main peak corresponds to the mean frequency of the surface waves at around 0.15 Hz, the maximum around 0.1 Hz correspond to the average frequency of the maximum surface waves, with a period of $T \approx 8.48$ s and a frequency of around 0.12 Hz (Meteorologisk institutt [2007]). The peak around 0.25 Hz then corresponds closely to the double frequency of the maximum surface waves.

The estimates of the probability density (PDF) are displayed in the lower panels in Figure 5.3, 5.4, 5.5, 5.6 and 5.7. When evaluating these estimates, we also use the additional information from the sample moments in Table 5.1. The skewness are only positive for the time intervals 9-12 minutes and 18-21 minutes. These intervals were found nonstationary with the runs test, but for all the other intervals the skewness is negative. This indicates a left-skewed distribution, with more data in the left tail compared to Gaussian distributed data. This is also evident in the figures, where the estimated PDF are above the left tail of the Gaussian curve (bold gray). For all time intervals expect 18-21 minutes the kurtosis is also negative (see Table 5.1), and we can see the extreme points of the estimated PDF tails are below the Gaussian (bold gray). This indicates a sub-Gaussian distribution, which describe distributions with a more flat top and lighter tails compared to a Gaussian distribution with the same mean and variance. In general, if we exclude the time intervals found nonstationary with the runs test, the distribution of the data are not symmetric, but have a left-skewed (negative skewness) distribution, and can also be described as sub-Gaussian because of the light tails and negative kurtosis.

Time [min]	**Mean** [μV/m]	**Std** [μV/m]	**Var** [μV/m]^2	**Skewness** (dim. less)	**Kurtosis** (dim. less)
0-3	0.038	0.029	0.00081	-0.15	-0.50
3-6	0.045	0.019	0.00034	-0.18	-0.12
6-9	0.040	0.018	0.00031	-0.16	-0.40
9-12	0.030	0.016	0.00026	0.30	-0.50
12-15	0.016	0.012	0.00013	-0.18	-0.18
15-18	0.0014	0.017	0.00029	-0.019	-0.20
18-21	-0.016	0.015	0.00023	0.34	0.61
21-24	-0.039	0.015	0.00022	-0.005	-0.59
24-27	-0.050	0.014	0.00021	-0.023	-0.30
27-30	-0.067	0.018	0.00031	-0.31	-0.37

Table 5.1: Estimated statistical properties for the segments of data (50 m cable, Station 1).

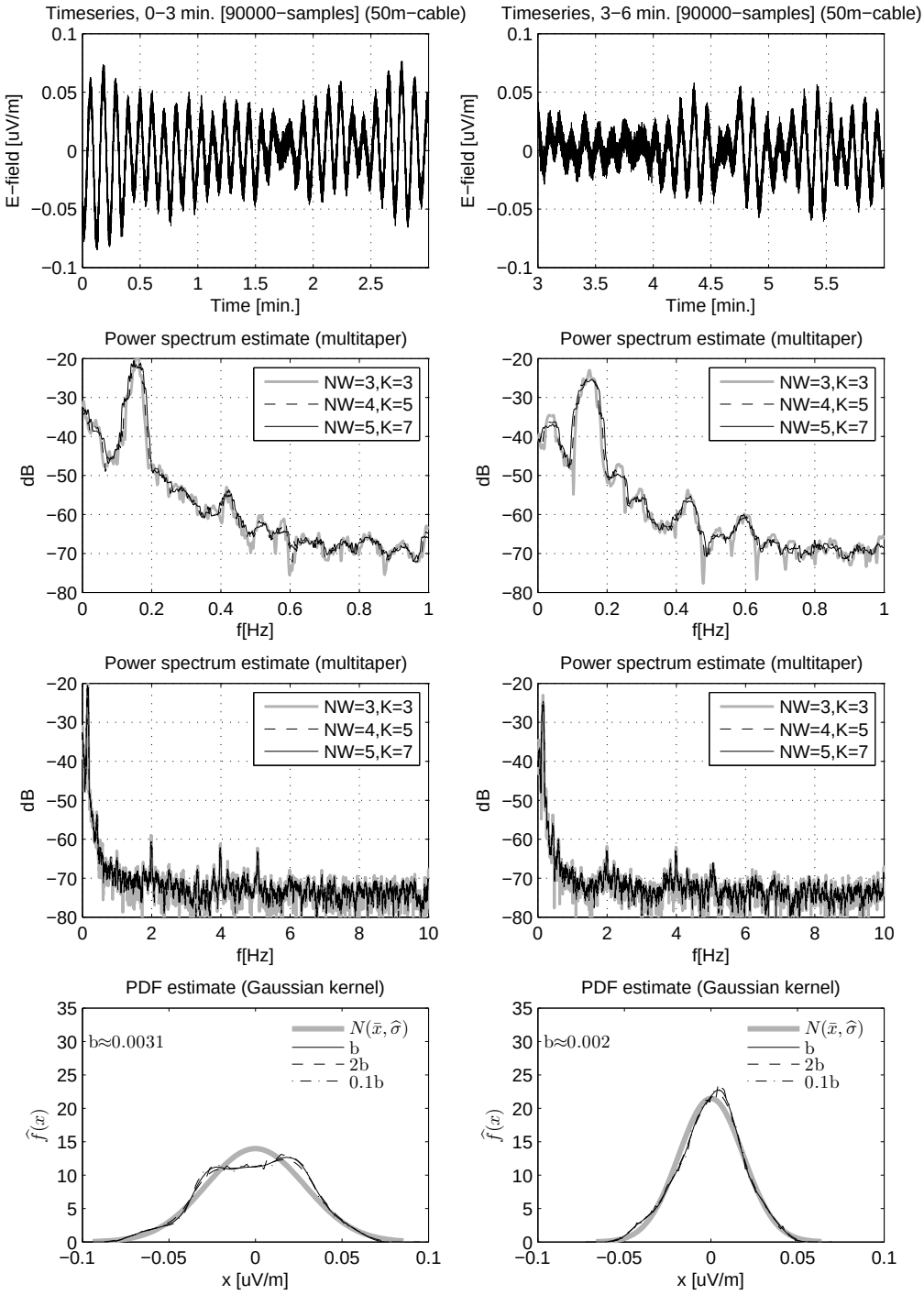

Figure 5.3: Time series for interval 0-3 and 3-6 minutes are given in the top left and top right panels respectively. The spectrum estimates and PDF estimates are align below the corresponding time series. From the time series panel and down we have, spectrum estimates 0-1 Hz, then the range 0-10 Hz in the next panel and in lower the panel the PDF estimate. See text for more details.

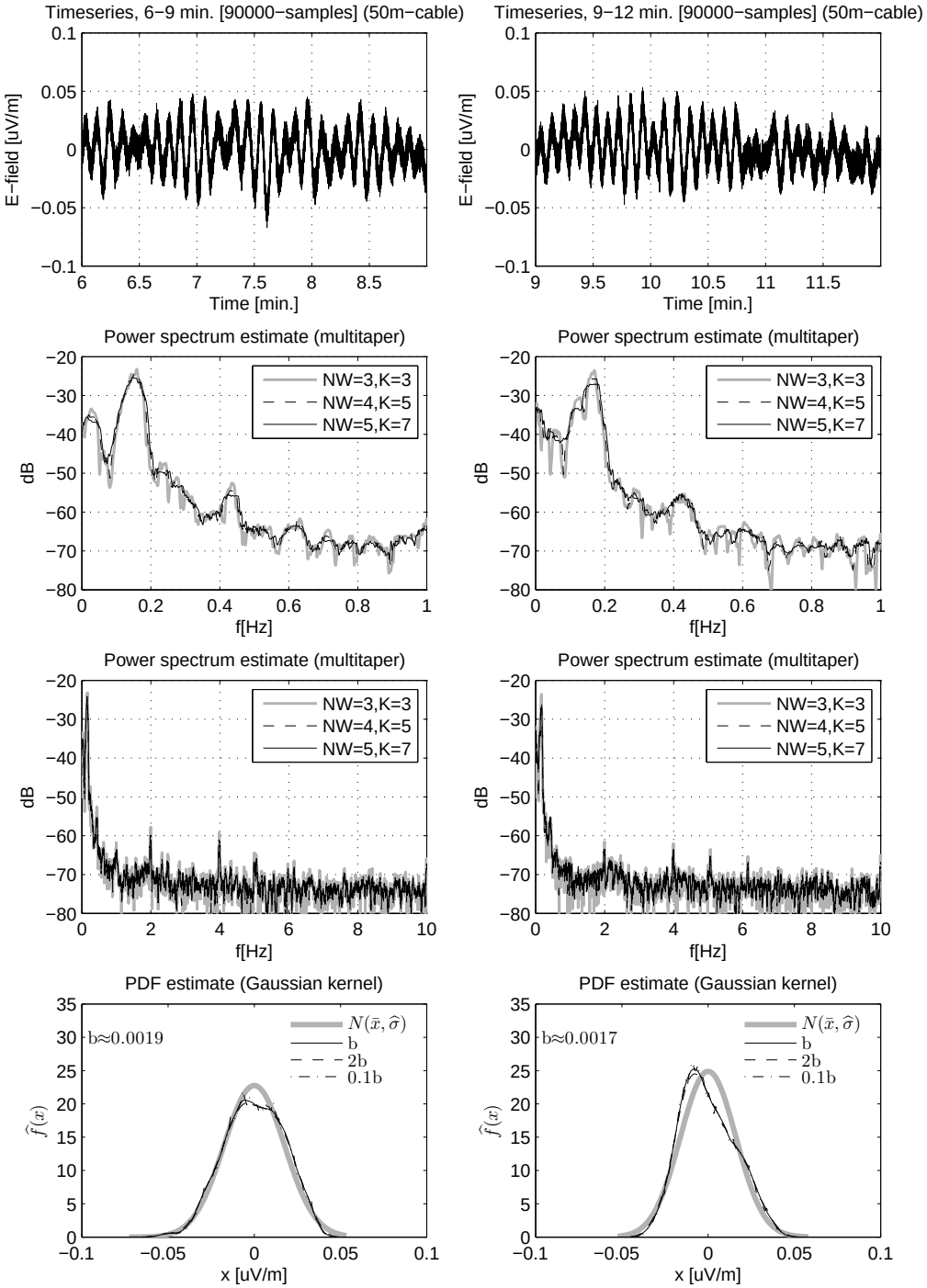

Figure 5.4: Time series for interval 6-12 minutes in upper panels, with spectrum estimates and PDF estimates align below the corresponding time series.

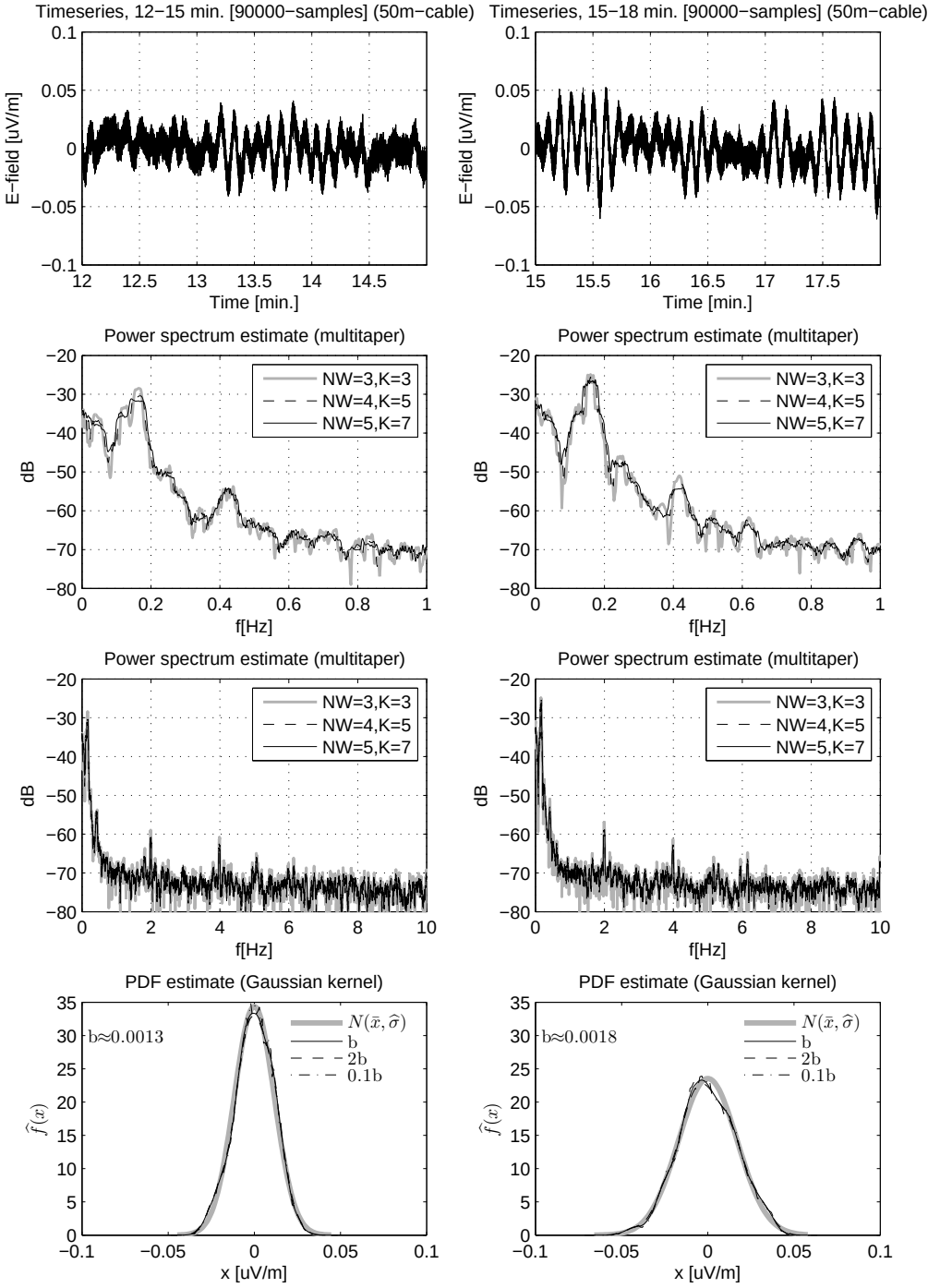

Figure 5.5: Time series for interval 12-18 minutes in upper panels, with spectrum estimates and PDF estimates align below the corresponding time series.

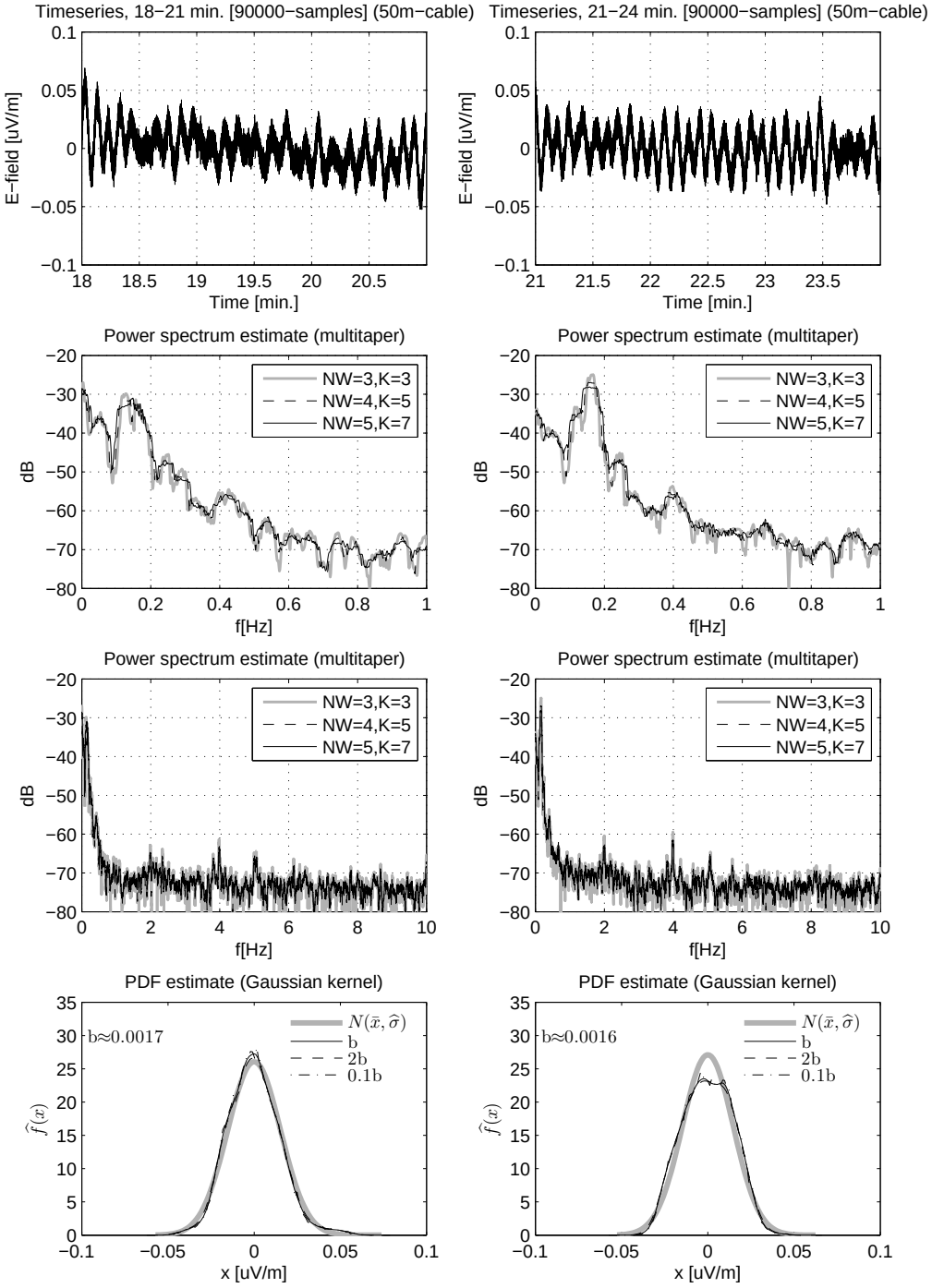

Figure 5.6: Time series for interval 18-24 minutes in upper panels, with spectrum estimates and PDF estimates align below the corresponding time series.

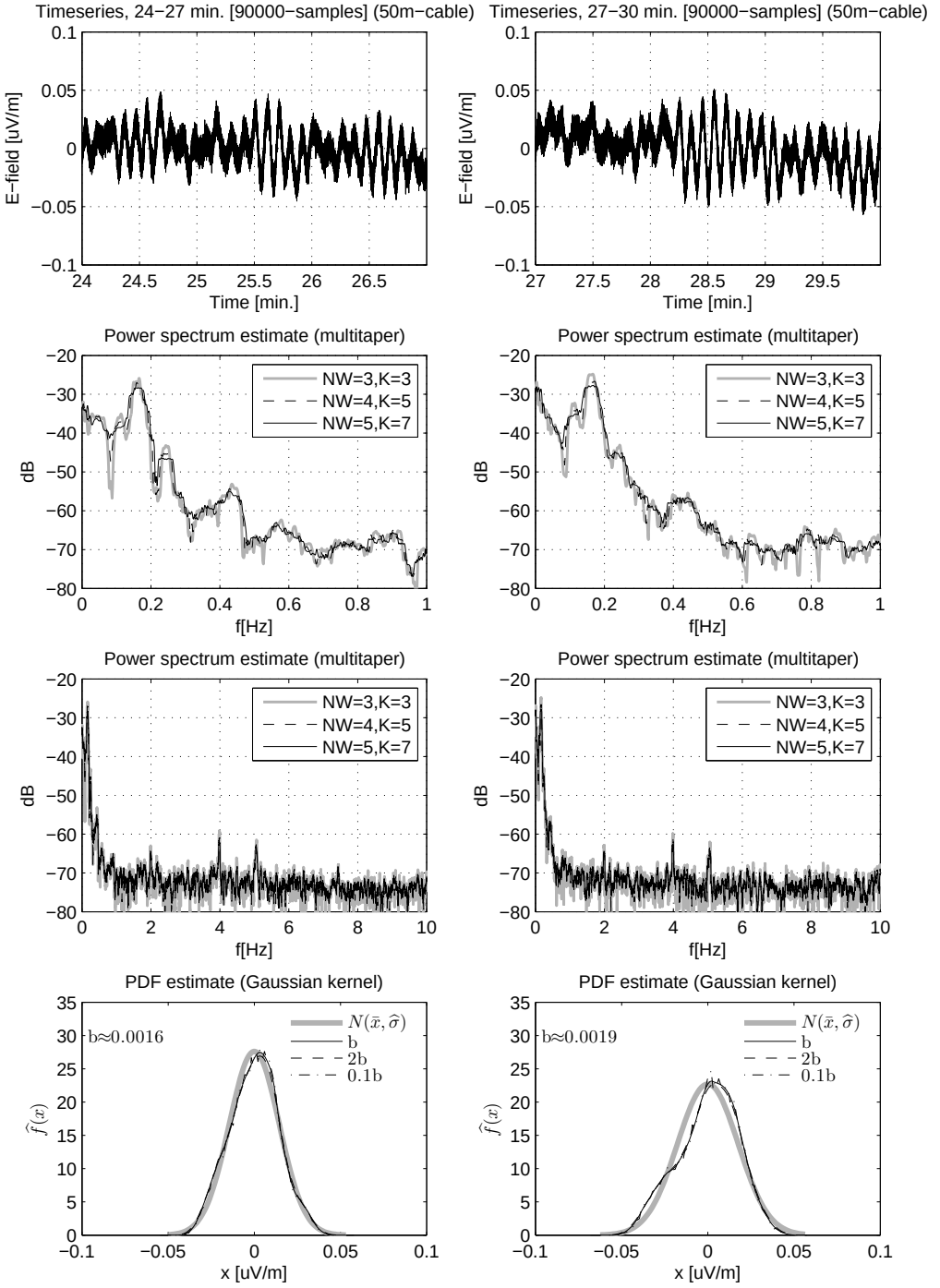

Figure 5.7: Time series for interval 18-24 minutes in upper panels, with spectrum estimates and PDF estimates align below the corresponding time series.

5.1.5 Approximate slope of the background spectrum

From the spectrum estimates in the previous section we clearly see that most of the power in the spectrum is located at the lowest frequencies (below 1 Hz). The slope of the spectrum is a parameter that characterises the background process, e.g., white noise has a flat spectrum and red noise falls off proportional to f^{-1}. By inspection of the spectra on a loglog plot, Figure 5.8, we did an average "eyeball" fit to all the ten spectra presented in Section 5.1.4. Here, we can see the lines (black dashed) approximately follows the decay in the spectra. Between 0-0.2 Hz the decay is proportional to f^{-1}, and we also note that the top of the peak around 0.15 Hz also has a similar decay. After this peak the spectra falls off rapidly, and between 0.2-1 Hz approximately proportional to f^{-4}. Above 1 Hz (up to 250 Hz) the spectrum becomes more and more flat.

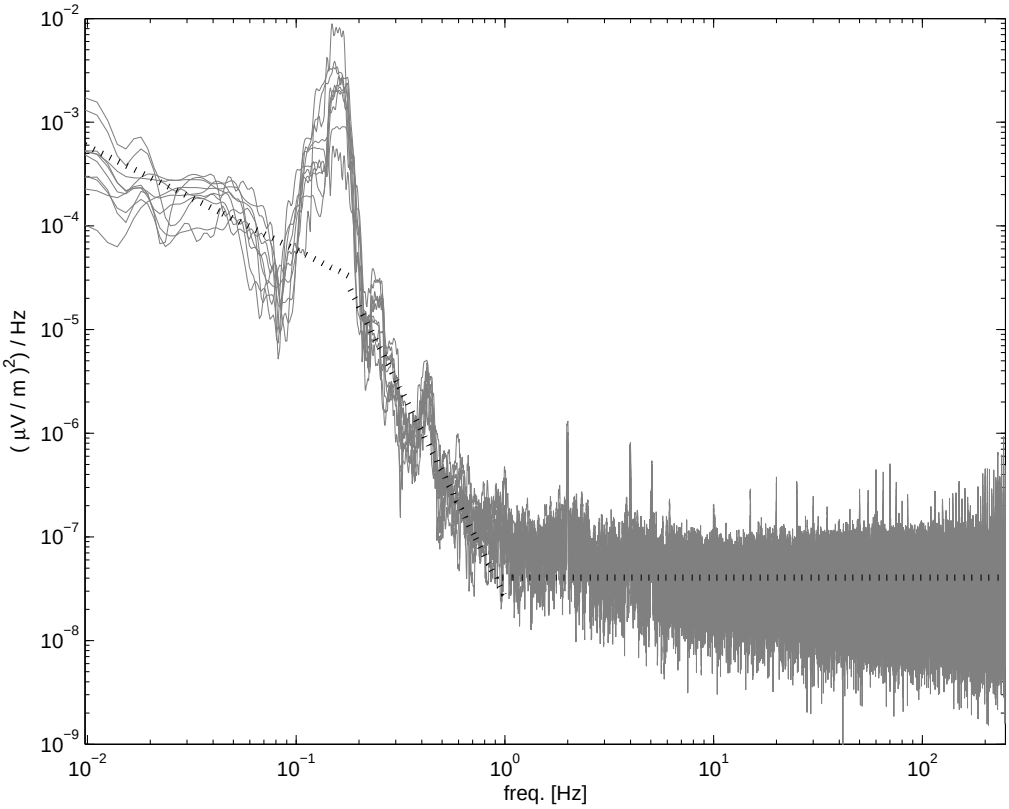

Figure 5.8: The gray lines are all the ten spectrum estimates from Section 5.1.4 (based on 3 minute segments, $NW = 4$, $K = 5$), now in a logarithmic scale. The black dashed lines are the approximated fitted lines, indicating the slope of the spectra.

5.1.6 F-test for sinusoidal components

To search for significant single frequency components, the F-test given in Section 4.9 was applied to the measured data (50 m cable, Station 1). We constructed an automatic routine were significant components where detected based on the following criteria: 1) Only select frequencies were the F-values are above the 99.9% confidence level. 2) For frequencies with F-values above the selected confidence limits, the power level for that frequency were then compared to the mean level of the "flat" region from 1 Hz to 250 Hz. Only frequencies with a power level more than 5 standard deviations above this mean, were found significant. For most of the frequencies between DC and 1 Hz, the level are above the mean plus $5\widehat{\sigma}$, and in practice this criterion only affects the frequencies above 1 Hz.

The test was applied to the same segments as in Section 5.1.4, and for each segment the test was done with different frequency resolutions, $NW = 4,5$ and $NW = 6$, respectively, and the number DPSS tapers applied were $K = 5,6$ and 7, respectively.

All the significant frequencies from the test are summarised in Figure 5.9, were the significant components are labeled to show for which resolution the component were found significant ($NW = 4$ ($\bullet$), $NW = 5$ ($\circ$) and $NW = 6$ ($\square$)). Clearly, most of the significant components are detected in the range from 10 Hz and above, were the spectrum is flattening out. The natural spectrum of the electric field fluctuations, are not expected to contain energetic features at these frequencies (Filloux [1973]), and the significant peaks are most likely caused by the electronics. The peak around 5 Hz, is seen in the spectrum from both the antenna at Station 1 and Station 2 (data from Station 2 will be presented in Section 5.4, Figure 5.19), is related to the electronics (Blixt [2007]), and the bundle of frequency components detected around 20, 60 150 and 220 Hz (Figure 5.9) are actually spaced by 5 and 10 Hz. We also note that the same frequency components are not significant for all time intervals, indicating that the level or the phase of the periodic components vary with time. From 10 Hz and above, only the components at 10 Hz and 155 Hz are significant in only one test, while the other components are either found significant in several tests for the same data segment (with different resolution), or at different time intervals.

Between DC and 10 Hz significant components were detected at 0.16, 0.24, 1.0, 2.0, 4.0 and 10.0 Hz. These are summarised in Table 5.2, including the time interval during which they were detected, and the resolution NW that

Freq. [Hz]	Time interval [min.]	NW
0.16	15-18	6
0.24	21-24 & 24 -27	4 & 5,6
1.0	3-6	4
2.0	9-12 & 12-15	5,6 & 4,5,6
4.0	9-12	4,5
10.0	15-18	6

Table 5.2: Significant single frequency components between 0-10 Hz.

was applied for the given test. The F-values plotted together with the reshaped and the original spectrum estimates for which the components at 2.0 and 4.0 Hz were found significant are given in Figure 5.10. Here we see all the F-values are below the 99.9% limit between DC-1.5 Hz (upper panel). In the lower panel, the frequencies 2.0 Hz and 4.0 Hz have F-values above the 99.9% limit, and in addition the level of the peaks are above $5\widehat{\sigma}$ from the mean level. These components were stated significant and the spectrum were reshaped at these frequencies. The reshaped spectrum is given as the bold black line, while the removed peaks are seen as the dashed gray line. Also at 5 Hz the F-value is above the 99.9% limit. There is a peak just above 5 Hz, but as the frequency for the high F-value and the peak do not coincide, the existence of a periodic component were rejected and no reshaping were done here.

In Figure 5.11, we show the original and reshaped spectrum for which the components at 0.16 Hz and 10.0 Hz were found significant. In the upper panel we see the reshaped spectrum after the component at 0.16 Hz were removed, and still after reshaping there is a prominent feature between 0.1 Hz and 0.2 Hz. This is the only test were the prominent peak were found significant as a periodic component. In the lower panel only the F-value at 10 Hz are above the 99.9% limit. Here, the level were slightly above $5\widehat{\sigma}$ from the mean.

In Figure 5.11, we show the original and reshaped spectrum for which the component at 0.24 Hz was found significant (upper panel). This component was significant in several tests (see Table 5.2), and the figure shows the test results for the time interval 21-24 minutes and frequency resolution $NW = 4$. The component is clearly separated from the prominent peak, and the reshaped spectrum seems quite featureless after the component at 0.24 Hz were removed. This is also the component which corresponds to the double frequency of the maximum surface waves. In the lower panel there is a high F-value just below 12 Hz, but the shape and the level of the spectrum at this

frequency do not indicate any periodic component here.

As mentioned in Section 4.9, the F-test is based on the assumption of a flat background spectrum. It works well when the spectrum is "locally white", i.e., when the spectrum changes slowly in the region $f \pm NW/(N\Delta t)$, and when only a single sinusoidal component exist in the same region. The rapid fall off in the background spectrum at the prominent peak, together with the additional shoulder just above 0.1 Hz, probably explains why the prominent peak is found significant (at 0.16 Hz) in only one of the tests. The automatic routine was made to run the test on many data segments, and to run several tests with the same data, but with different parameters. In addition, the reshaping and removal of the sinusoidal components, is the first step to a "robust" estimation of the background spectrum. This is a method proposed by Mann and Lees [1996] to estimate significance of narrow band features and sinusoidal components in a red $(1/f)$ background spectrum. Here, confidence intervals are related to a AR(1) spectrum which is fitted to a median smoothed version of our reshaped spectrum. Unfortunately, the AR(1) model does not follow the slope of the electric field spectrum (f^{-4}), and the method based on the AR(1) model is probably not well suited our more complicated data.

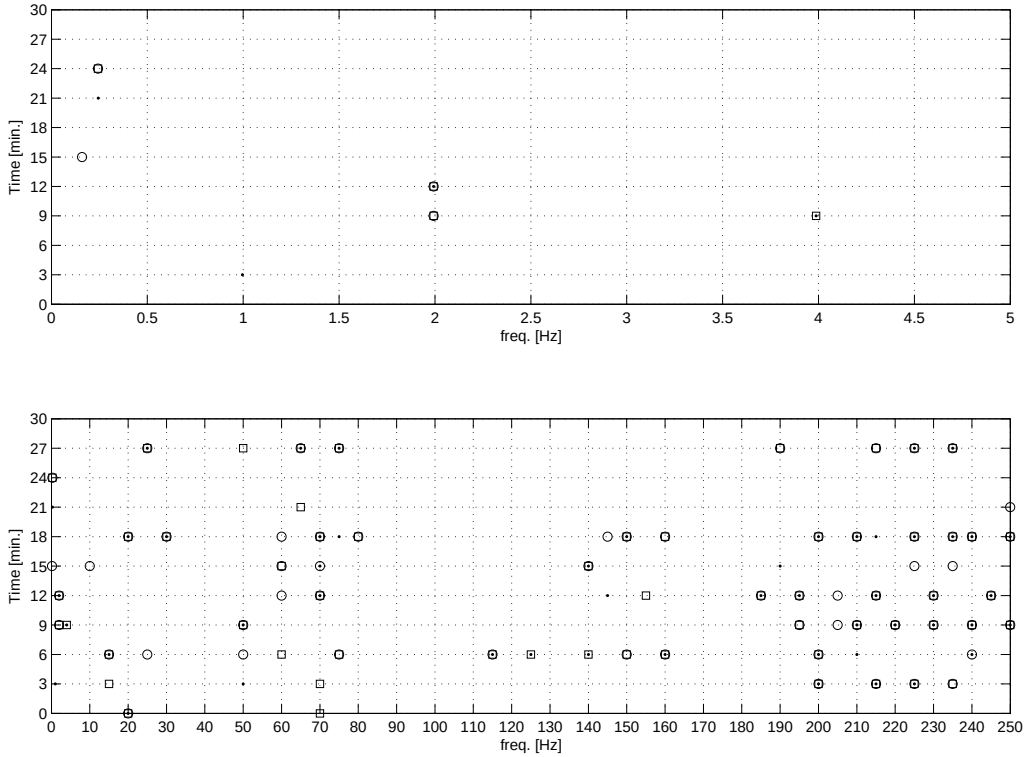

Figure 5.9: The significant frequencies found by the automatic F-test. The symbols represent the results for different frequency resolutions, $NW = 4$ (•), $NW = 5$ (∘) and $NW = 6$ (□). Upper panel is a zoomed in view of the range 0-5 Hz, and in lower panel the whole range 0-250 Hz. The vertical axis gives the starting point of each data segment.

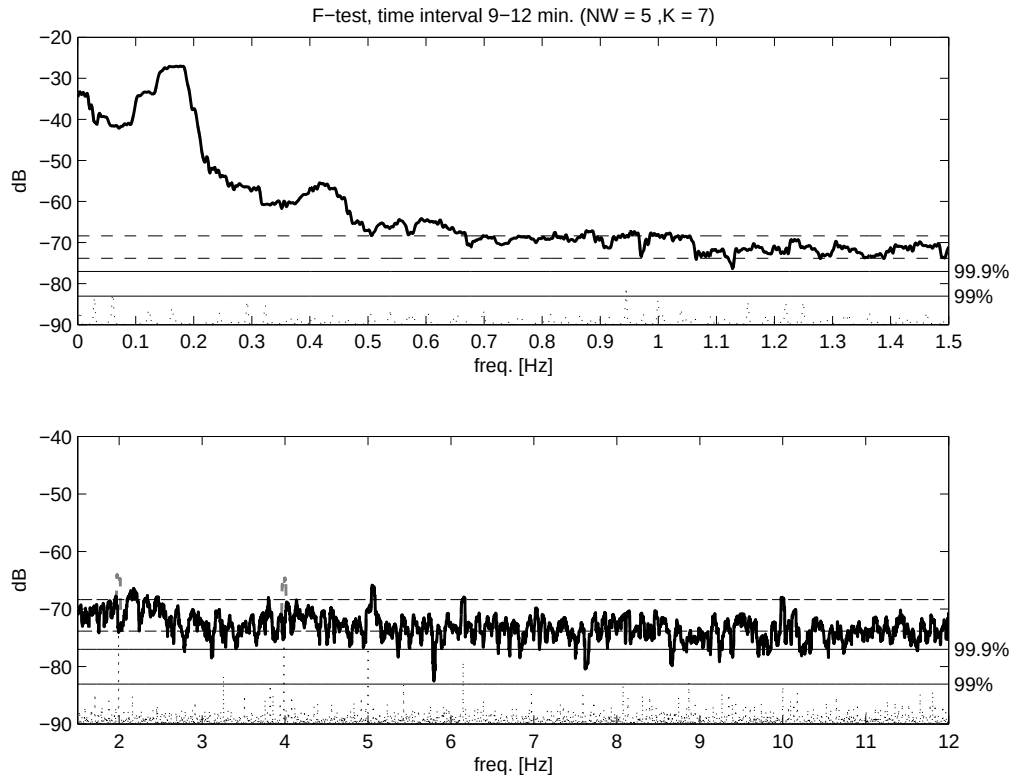

Figure 5.10: F-test plot with significant components at 2.0 and 4.0 Hz, for the time interval 9-12 minutes. The estimated F-values (dotted line) and the 99 and 99.9% confidence limits (solid horizontal lines), are scaled to overlap the spectrum. The dashed horizontal lines are the mean level between 1-250 Hz (lowermost) and the mean level plus $5\widehat{\sigma}$. The reshaped spectrum are given in bold black and the original spectrum is in bold dashed gray. The range 0-1.5 Hz and 1.5-12 Hz are given in upper and lower panel respectively.

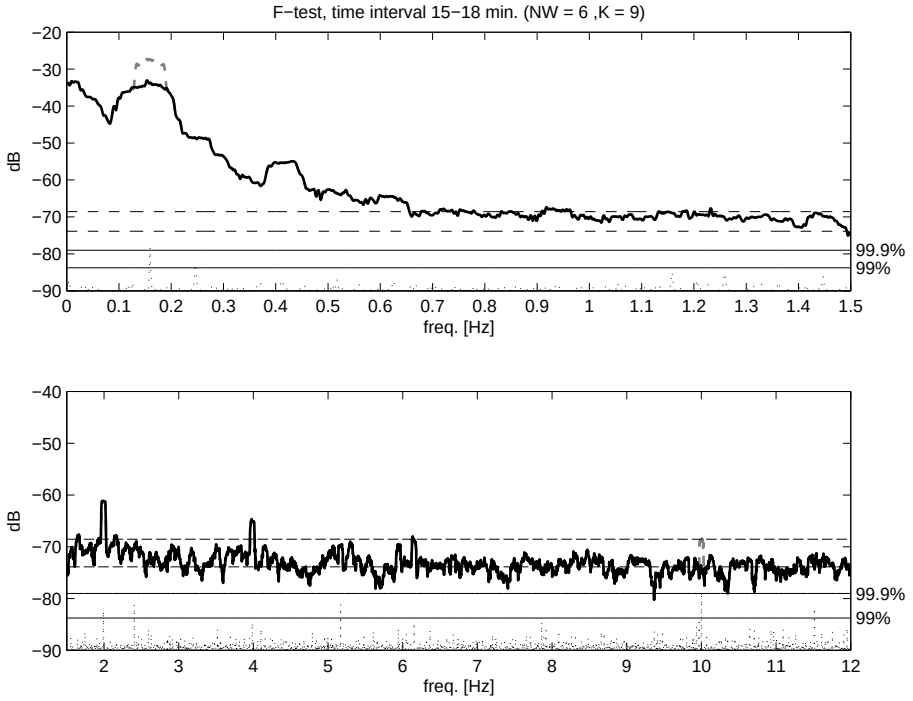

Figure 5.11: F-test plot with significant components at 0.16 Hz and 10.0 Hz, for the time interval 15-18 minutes. Line properties as in Figure 5.10.

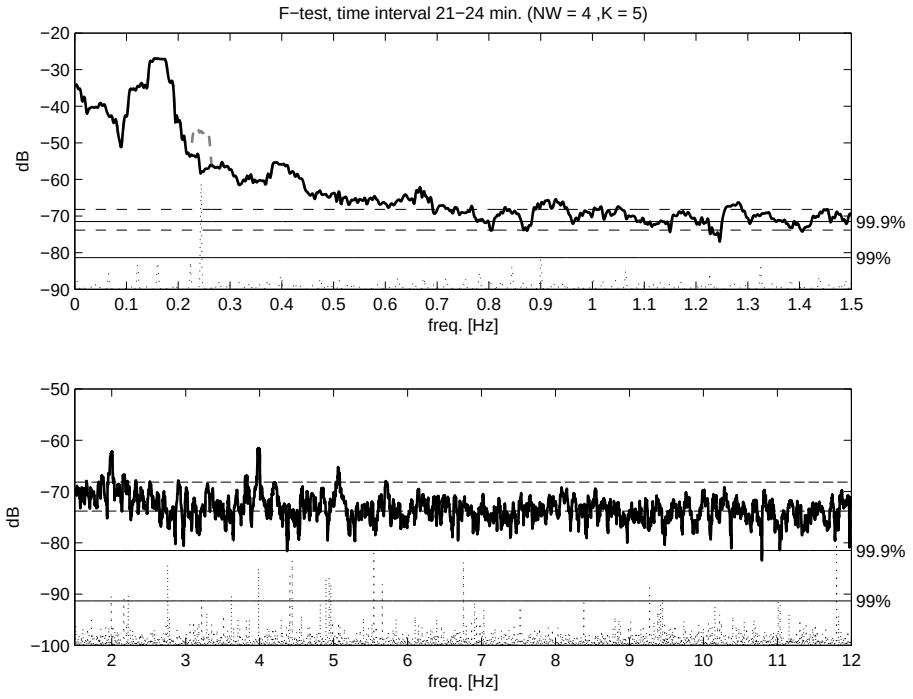

Figure 5.12: F-test plot with significant components at 0.24 Hz, time interval 15-18 minutes. Line properties as in Figure 5.10.

5.1.7 Time development of the prominent peak

To further examine the time development of the prominent peak around 0.15 Hz, the multitaper method was again applied to segments of 90000 samples (3 minutes), but this time as a "sliding-window", where the starting point of the segments were stepped by 5000 samples (10 sec.) forward between each estimate. This procedure result in 163 estimates of the total data series. For each estimate, $NW = 4$ and $K = 5$ eigenspectra were averaged. The level and frequency of the maxima between 0.1-0.2 Hz from each estimate, are given in Figure 5.13, together with the average power in the same range, given as

$$P_{av} = 2\int_{0.1}^{0.2} \widehat{S}^{(MT)}(f)\mathrm{df}. \tag{5.1}$$

From Figure 5.13 we see the maximum level changes more than 10 dB during the 30 minutes, with two distinctive drop in the level at just above 10 minutes and around 18 minutes. When the level drop at 18 minutes also the frequency drop down to about 0.12 Hz. In Figure 5.14, 28 of the multitaper estimates from the sliding window procedure above are shown. Here, the starting points of each data segment are spaced by one minute and the maxima between 0.1-0.2 Hz for each estimate is marked with a dot. The same 28 estimates are also given as a contour plot in Figure 5.15, and we can clearly see the drop in the maximum peak (about 0.15 Hz) around 10 and 18 minutes.

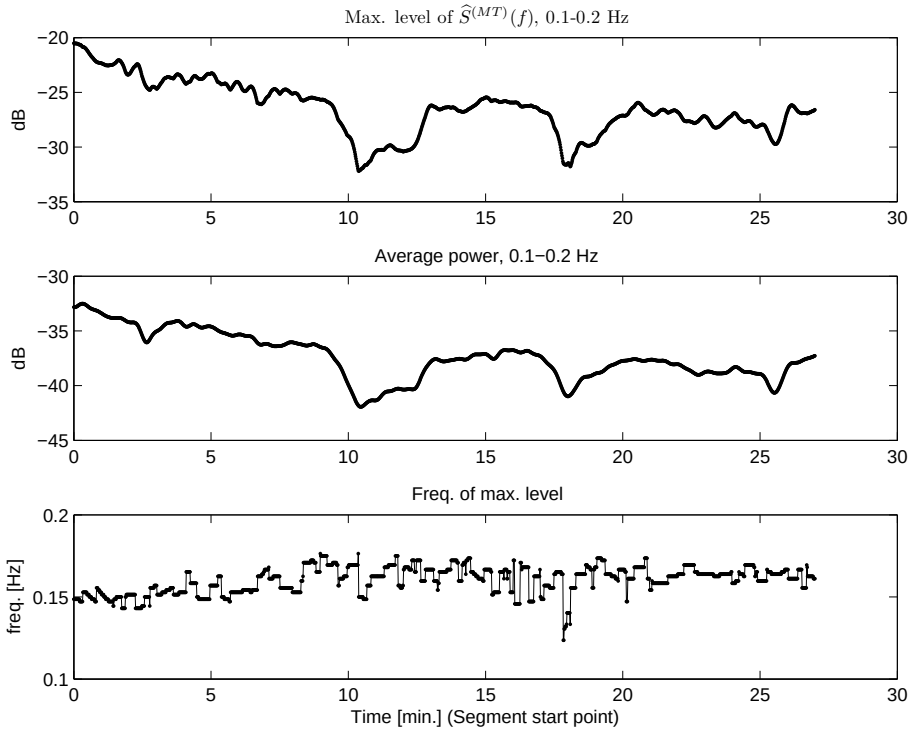

Figure 5.13: The maximum level between 0.1-0.2 Hz is given in upper panel, average power 0.1-0.2 Hz in middle panel and the frequency of the maximum level is given in the lower panel. Time axis gives the start of each segment.

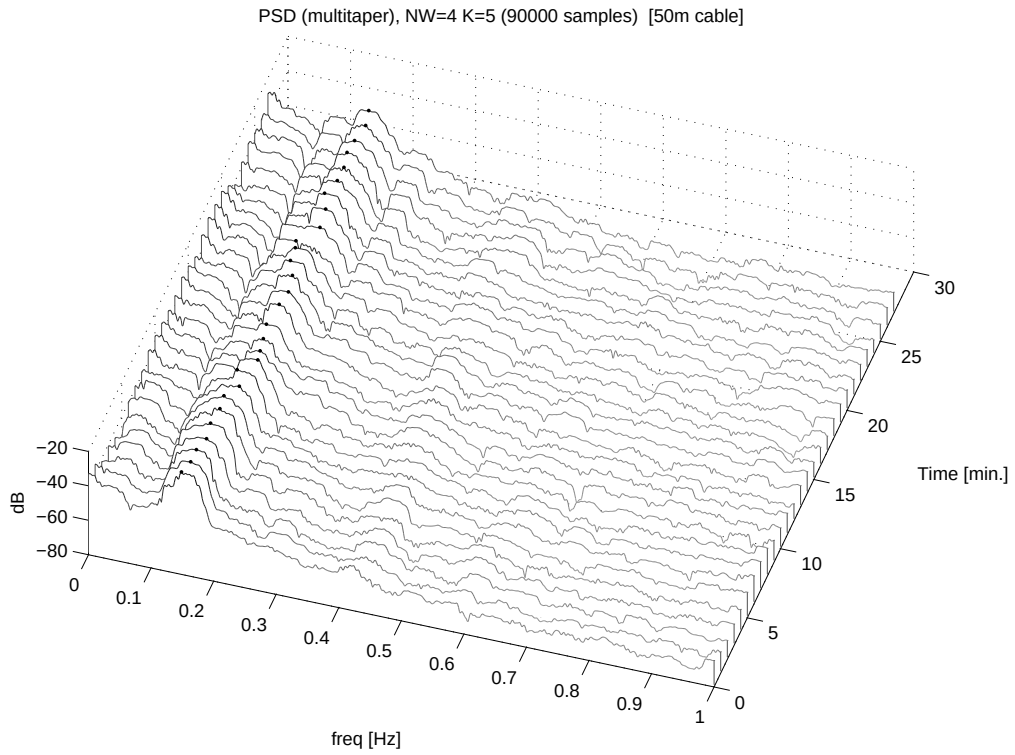

Figure 5.14: Multitaper spectrum estimates based on 3 minute segments ($N = 90000$ samples of data). Between each estimate the starting point was stepped forward 1 min, giving 28 estimates. For all estimates, $NW = 4$ and $K = 5$. The time axis gives the starting point of each data segment.

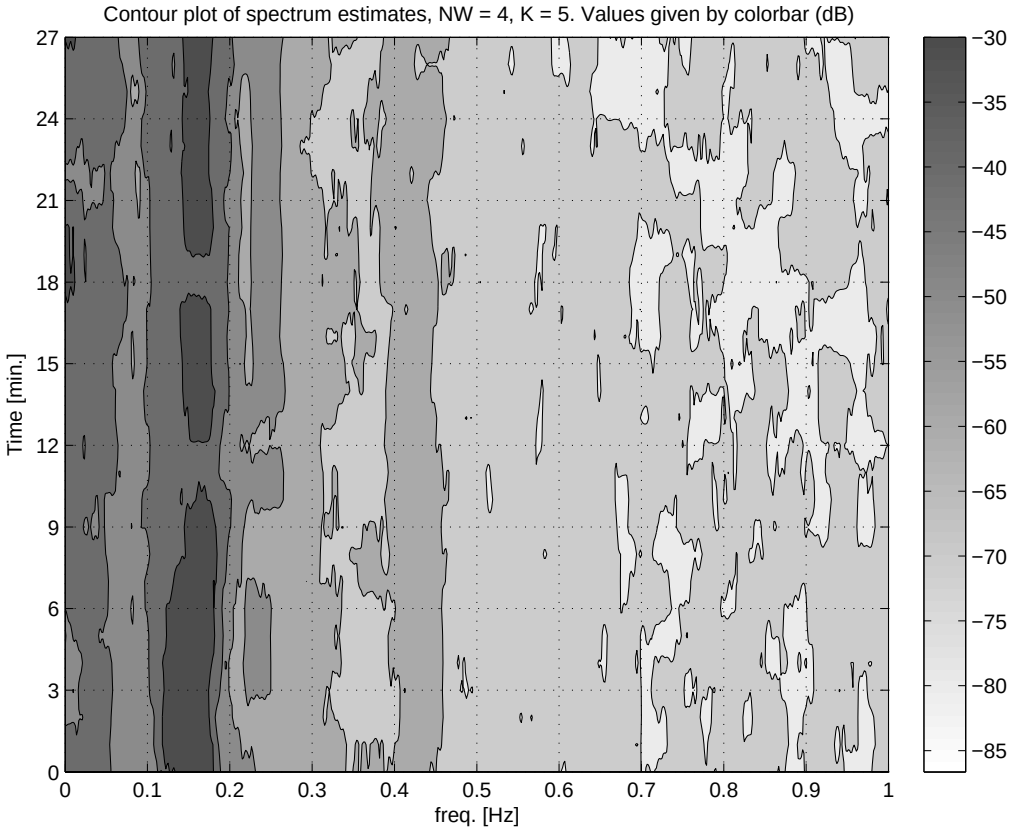

Figure 5.15: Contour plot of the same estimates as in Figure 5.14, for the frequency range 0-1 Hz. The power level in dB is given by the colorbar, and the contour lines are spaced by 10 dB, starting at -30 dB.

5.2 Measurements of antenna position

The position of the seafloor base and the upper buoy of the E-field antenna at Station 1 where measured as explained in Section 3.2. Here, $N = 1800$ samples were recorded, with sampling rate $f_s = 1$ Hz, and covers the same time interval as the E-field data. The accuracy in the position measurements was calculated to be approximately ± 1 m (Blixt [2007]).

The measured time series of the East position for the top buoy and the seafloor base are given in Figure 5.16 and Figure 5.17 respectively. The time series are given in the upper left panels, with the spectrum estimate in the upper right panel. The numerically calculated East velocity is given in the lower left panel. Here, the central difference method did not capture all the rapid changes in the time series, and the forward difference scheme gave a better result. This is also visual in the spectrum estimate in the lower right panel, where the central difference gives lower levels at frequencies above 0.2 Hz.

As seen in the position time series in Figure 5.16 and Figure 5.17, most of the fluctuations in the data are below the precision of the measurement (± 1 m). The measuring method is sensitive to movement of the operating vessel, the accuracy of the GPS measurement and probably also layers in the ocean with different sound speed. The fluctuations we see can therefore have other sources than movement of the antenna, and hence it is not a good predictor for the fluctuation in the E-field caused by the antenna motion. In addition, the sampling rate also differs from the E-field measurements, and a comparison between these position data and the E-field data would be difficult. Still, the spectrum estimates of both the position and the velocity given in the right panels in Figure 5.16, have local maxima around 0.1 and 0.4 Hz. This is close to the local maxima seen in the electric field spectra (see the 0-1 Hz plot Figure 5.3, 5.4, 5.5, 5.6 and 5.7), which could indicate that the position measurements and the electric field measurements are affected by the same ocean phenomena.

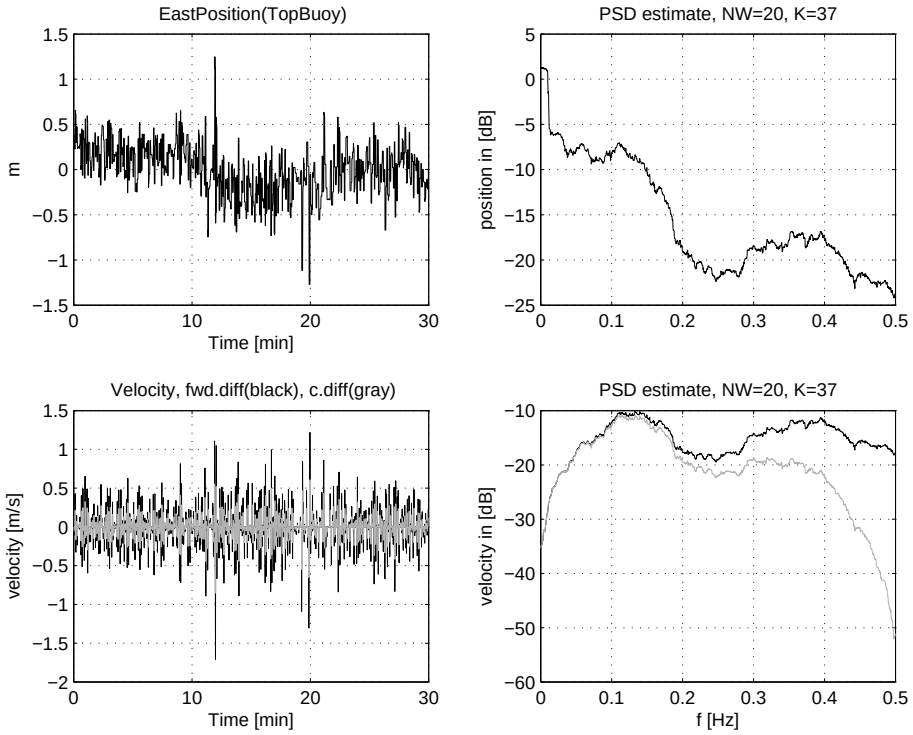

Figure 5.16: The upper left panel displays the measured time series of the East position of the top buoy, with the mean subtracted. The corresponding East velocity is shown in the lower left panel. Right panels displays the multitaper spectrum estimates ($NW = 20$), position in upper panel and velocity in lower panel, respectively. In the lower panels velocity estimated by both forward difference (black) and central difference (gray) methods are shown.

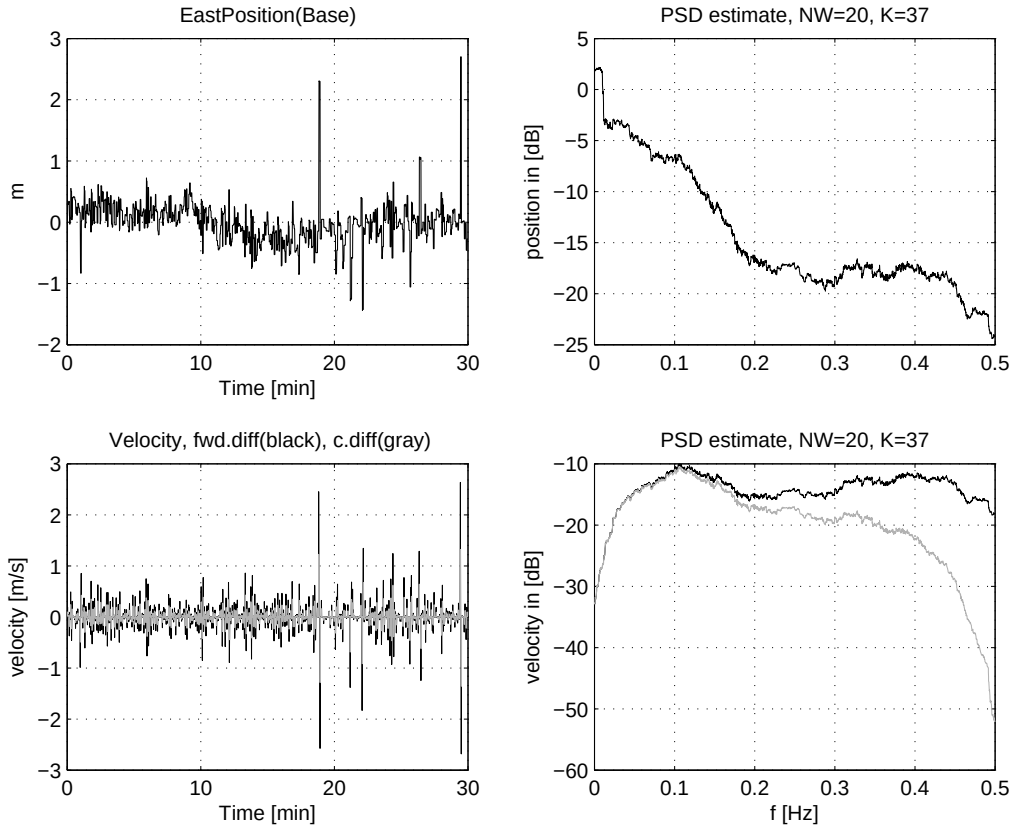

Figure 5.17: The upper left panel displays the measured time series of the East position of the seafloor base, with the mean subtracted. The corresponding East velocity is shown in the lower left panel. Right panels displays the multitaper spectrum estimates ($NW = 20$), position in upper panel and velocity in lower panel, respectively. In the lower panels velocity estimated by both forward difference (black) and central difference (gray) methods are shown.

5.3 Geomagnetic activity

To compare the measured vertical electric field with the geomagnetic activity, we got data from the nearest on-land geomagnetic station (Solund, 61°N, 4.5°E, Tromsø Geophysical Observatory [2007]). The data from the same time period are shown in Figure 5.18. Here, the figure gives the fluctuation around the sample mean values, and given in the same coordinate system as in Figure 2.2. The respective subtracted mean values were, $\overline{F_y} \approx 14504$ nT (North), $\overline{F_x} \approx -376$ nT (positive East) and $\overline{F_z} \approx -48836$ nT (Vertical, positive upwards).

The geomagnetic data were sampled every $\Delta t = 10$ s, and this sampling interval excludes a direct comparison with the electric field measurement at frequencies above 0.05 Hz, which is below the range of main interest, namely 0.1-10 Hz. If we look at the overall trend in the vertical electric field measurements, the mean level changes about 0.11 μV/m during the 30 minutes (see Figure 5.1 and Table 5.1). The North component of the geomagnetic field, F_y (upper panel Figure 5.18), is the main contributor to the vertical electric field, and the geomagnetic variation do not match the shape of the trend in the electric field measurements. In addition the geomagnetic variation is small. By assuming an East directed water velocity of 1 m/s, the fluctuation in the electric field at sea level would be in the same range as the geomagnetic North fluctuation, i.e., a few nV/m. The fluctuation of the geomagnetic field will then be attenuated by the ocean, which further reduces its effect on the vertical electric field measured at the seafloor. This indicates that the trend seen in the electric field measurements is not caused by the variations of the geomagnetic field.

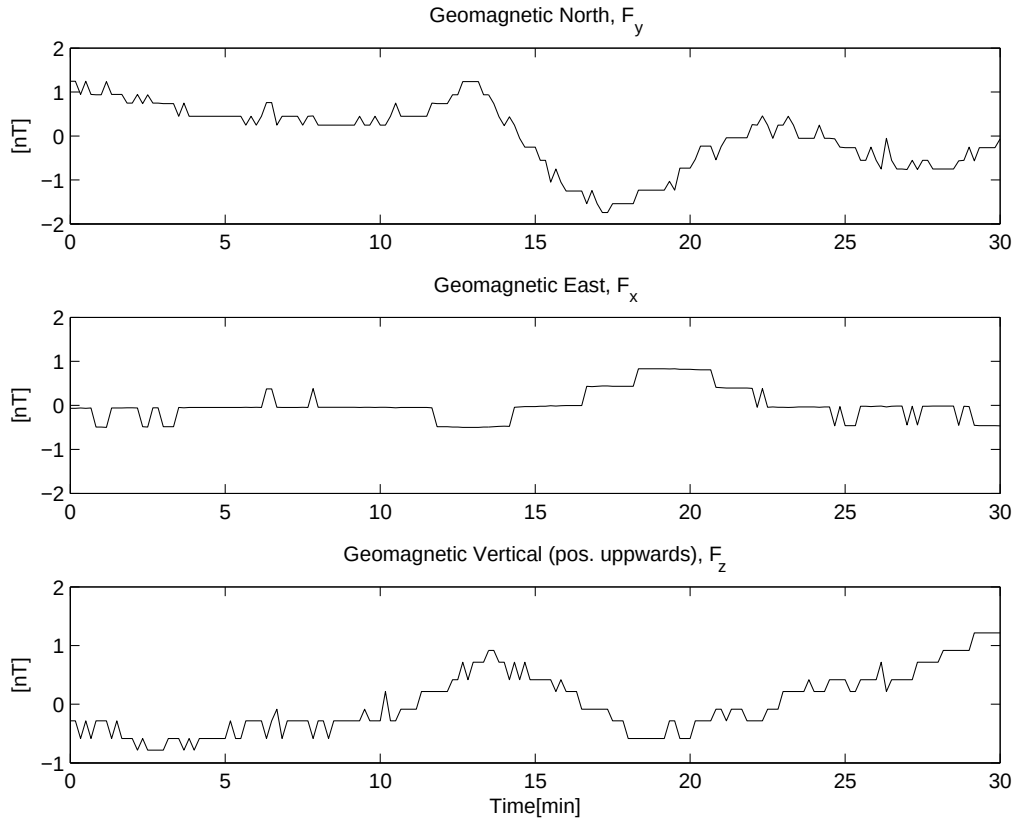

Figure 5.18: Geomagnetic fluctuations measured by a nearby on-land station (Solund, 61°N, 4.5°E, Tromsø Geophysical Observatory [2007]). The North, East and Vertical components are given in the upper, middle and lower panel respectively.

5.4 E-field measurements from other locations

In the previous sections we have analysed the data from the vertical electric field measured by the 50 m cable antenna at Station 1. This data set will now be denoted Station 1. We will here present 6 minutes of data measured by similar antennas at other locations.

- Data from a 50 m cable antenna located at Station 2, now called Station 2. The vertical electric field was measured at the same time as Station 1, and the distance between the stations were 1 km.
- Data from a 230 m vertical cable antenna located in the same area as Station 1 and Station 2, but recorded in 2006. This will now be called 230 m (2006) data.

The Station 2 data are given in Figure 5.19. A prominent oscillation in the time series is evident also here. As for Station 1, the spectrum estimates shows a prominent peak around 0.15 Hz with local maxima around 0.25 and 0.45. In addition, Station 2 has a peak at 0.55 Hz. In the third panels from the top we observe a relative broad feature, peaked just below 2 Hz. Also Station 1 has a peak around 2 Hz, but for Station 2 this is more energetic. A consistent peak at 5 Hz is also observed, but this is related to noise from the electronics (Blixt [2007]).

The 230 m (2006) data are given in Figure 5.20. In the 0-1 Hz spectrum estimates, the prominent peak is located just above 0.1 Hz, with an additional peak at approximately 0.22 Hz in the 3-8 min. time interval. In the 0-10 Hz spectrum estimate, we observe a local maximum at approximately 2.2 Hz.

As we can see, measurements from different locations and different times have a dominating peak located between 0.1-0.2 Hz, which is a frequency range that can be related to the surface waves.

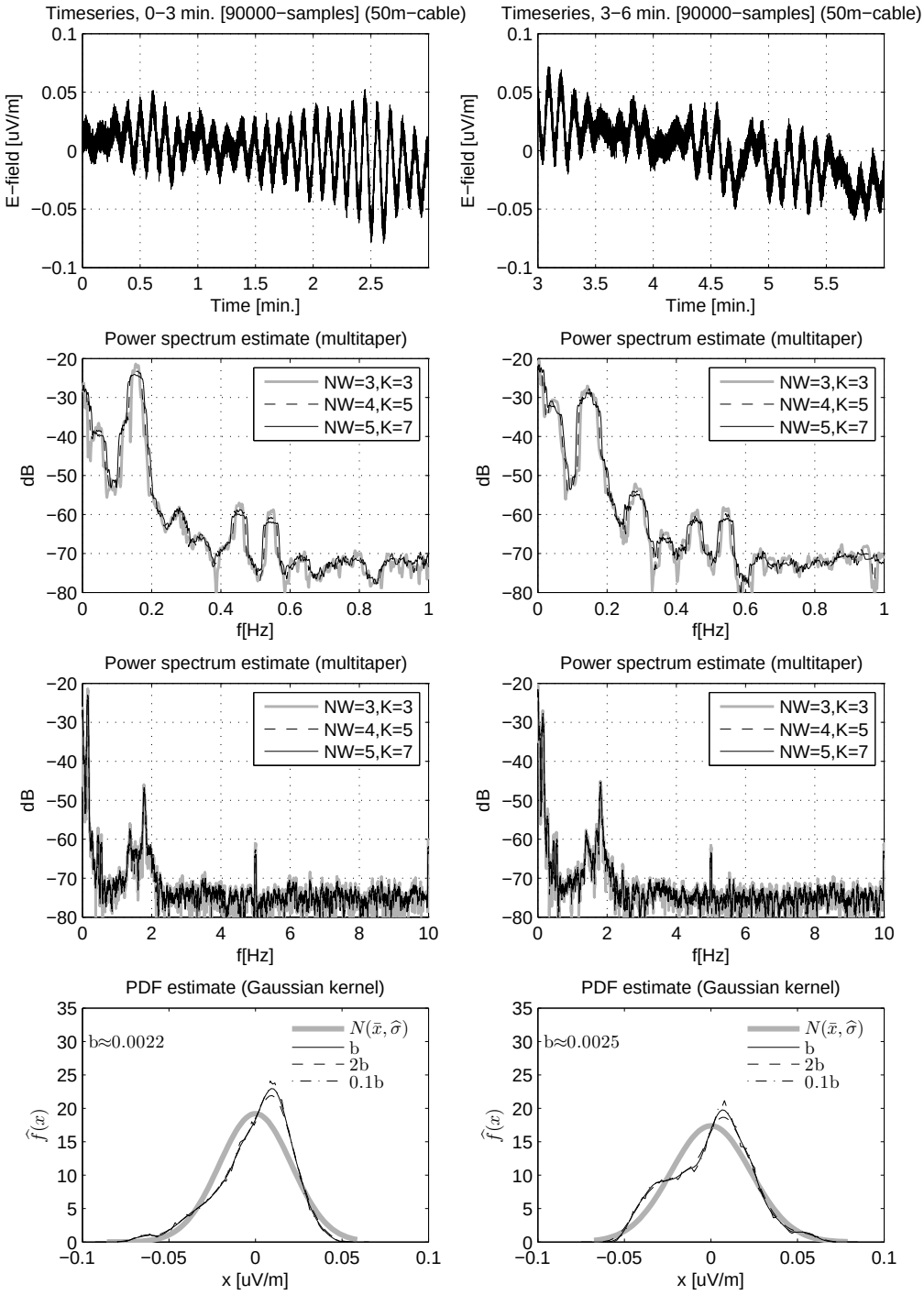

Figure 5.19: E-field data from the 50 m cable antenna, Station 2 (2007). Top panels gives the sample mean removed time series, in top left, time interval 0-3 minutes and in top right 3-6 minutes. Estimates are aligned below the respective time series.

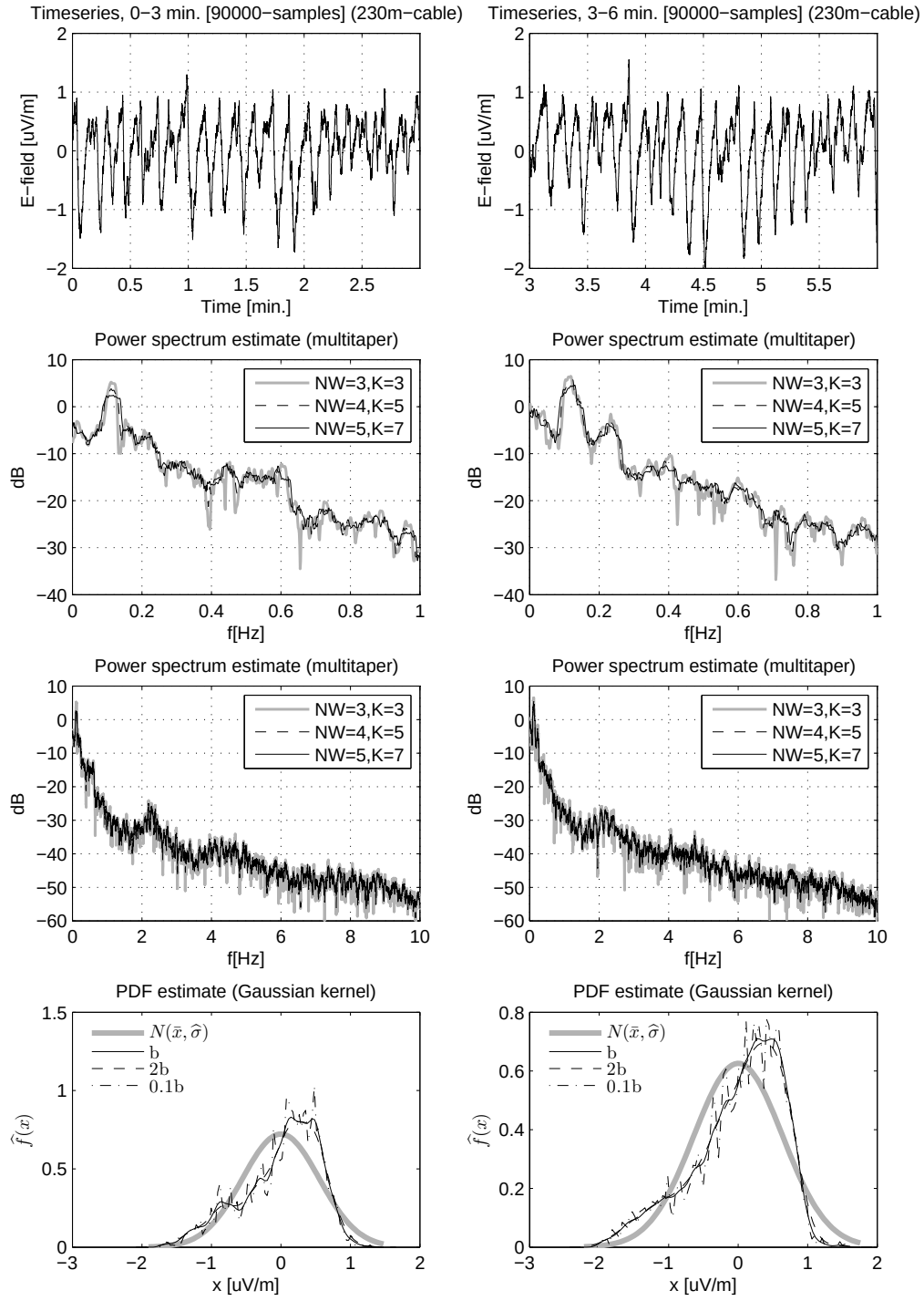

Figure 5.20: E-field data from the 230 m cable antenna, recorded in 2006. Top panels gives the sample mean removed time series, in top left, time interval 0-3 minutes and in top right 3-6 minutes. Estimates are aligned below the respective time series.

Chapter 6

Discussion and conclusions

Data

Electric field data measured by vertical antennas at the seafloor has been analysed in this thesis. Main emphasis is on a data set collected at 20:54 UTC, Sept. 19, 2007 at a depth of 316 m below sea surface. Hereafter referenced to as the Station 1 data. Data from the other antennas are named Station 2 and 230 m (2006). If not specified the discussion treat the Station 1 data.

Methods

The spectrum of the vertical electric field has a large dynamic range, including a rather steep peak up to -20 dB, followed by a rapid fall off to the flat region below -70 dB, including several sinusoidal components at the higher frequencies. The data are also dynamic as a function of time, where the amplitude and the contribution from different frequencies changes during time. Hence, this is rather complicated data to resolve. The multitaper method we implemented, can be applied to relatively short time segments, and by a proper selection of the number of averaged eigenspectra, still provide good bias and variance properties and a reasonable frequency resolution. In addition, we can easily apply several independent estimates, by adjusting the frequency resolution parameter NW. Then, by comparing the different estimates, consistent features seen in several spectral estimates can be revealed and strengthen their status as true features in the spectrum.

By the use of the multitaper method, we can also extend the analysis with an F-test to evaluate the significance of possible present sinusoidal components. A slowly varying background spectrum, which is the basis of this test, is not fulfilled for our data at the low frequencies (below 1 Hz). Hence, this can explain the low F-values at the prominent peaks between 0.1-0.3 Hz in most

of our tests. In addition, we also encounter problems if the amplitude and phase of the periodic components vary, or if several sinusoidals are present with a spacing less than the half-bandwidth W. Therefore, the comparison of different spectral estimates seems to be the most powerful way to reveal true peaks and features at the low frequencies. Still, the F-test provides valuable information, and in particularly for the higher frequencies (where the spectrum becomes more flat) and it can be used to search for unphysical components generated by the electronics. As we made an automatic F-test routine, the test can easily be applied to many data sets, or to the same data but with different parameters. By using both the comparison between several multitaper estimates, and the F-test, the spectrum analysis becomes more complete. We used the multitaper method based on the arithmetic average of several eigenspectra, and the three highest order potentially usable DPSS tapers were excluded in our analysis.

For estimation of the probability density function we used the standard non-parametric kernel methods. The kernel width was chosen according to Silverman's rule-of-thumb. The kernel estimators produce a smooth, continuous and differentiable function estimate, which is preferred for further analysis and calculations based on the estimate. To further reveal consistency in the estimates we could have used even more fixed kernel widths, or alternatively we could have used the adaptive method to select the kernel width (e.g., Silverman [1986]). The electric field data were found to be non-Gaussian, indicated both by the kernel estimates and the sample moments. If we exclude the time intervals flagged as nonstationary by the runs test, the data were left skewed, and with lighter tails than Gaussian distributions.

The implemented runs test is a rather simplistic indicator for trends and lack of stationarity in a data set. Still, it has proven to be useful when we evaluate our estimates.

Observations

The maximum peak in the electric field spectrum is around 0.15 Hz. It varies slightly in frequency, but the level changes more than 10 dB during the 30 minutes of recordings. The frequency of the maximum peak corresponds closely to the frequency of the mean frequency of the surface waves. In addition, the shoulder just above 0.1 Hz, indicating a secondary peak, corresponds to the frequency of the maximum surface waves (0.12 Hz). The peak seen at 0.24 Hz, then correspond to the double frequency of the maximum surface waves. Hence, we see an obvious relation between the measured electric field

and the sea surface waves. Also the data from Station 2 have a prominent peak around 0.15 Hz, which supports this relation. While the prominent peak is located around 0.1-0.2 Hz for both Station 1, Station 2 and the 230 m (2006) data, we also note the differences in the spectrum at frequencies above 0.2 Hz. Particularly, the feature seen at around 2 Hz for all the antennas, has a substantially different shape and level for data recorded by the different antennas, indicating a common origin but with local variations.

In general the amplitude of the electric field fluctuations were less than 0.07 μV/m (Station 1). If we assume that the antenna was completely stationary during the recordings, we can relate this to an average fluctuation in the water between the electrodes (horizontal, East-West). By using the measured north component of the magnetic field of $F_y = 14504$ nT, this indicates a fluctuating water velocity with amplitude less than 5 mm/s. If the cable and the upper electrode of the antenna were moving, it would likely be with a velocity in the same range as the fluctuating water. Hence, the accuracy ($\pm$1 m) offered by the position data from the experiment is not accurate enough to determine the small scale movement of the antenna.

The electrodes were located at depths of 316 m (seafloor) and 266 m respectively and the 2D linear wave theory can not explain the horizontal velocities in the mm/s range at these depths for a single surface wave with period 6.8 s. E.g., for a surface wave described as a single periodic wave train, the elevation of the surface causes circular particle motion below the surface. For a finite depth d, the wave number k is given through the linear dispersion relation (e.g., Sarpkaya and Isaacson [1981](p.155))

$$\omega^2 = g\,k\tanh(k\,d), \tag{6.1}$$

were $g = 9.81$ m/s^2. The amplitude of the horizontal velocity beneath the surface is given by (e.g., Sarpkaya and Isaacson [1981](p.157))

$$v(z) = \frac{\pi H}{T}\frac{\cosh(kz + kd)}{\sinh(kd)}. \tag{6.2}$$

Here, $z = 0$ at the flat surface, and $z = -d$ at the seafloor and H is the total wave height of the surface wave (twice the amplitude from the flat surface). By solving Eq. (6.1) numerically for the observed mean surface wave period $T = 6.8$ s ($\omega = 2\pi/T$), we obtain the wave number $k = 0.08703$ m^{-1}. If we then solve Eq. (6.2) for this wave number, and a finite depth of $d = 316$ m and a wave height $H = 4$ m, the amplitude of the horizontal particle velocity at the upper electrode $z = -266$ m, will be in the range 10^{-7} mm/s and will be further reduced close to the seafloor. Hence, this is far from the velocity 5 mm/s

indicated by the electric field fluctuation, and a linear model of the subsurface water motion due to the surface waves do not explain the results.

No obvious correspondence was observed between the geomagnetic field and the measured electric field. The trend seen in the vertical electric field time series could be caused by a drift in the DC-level of the electrodes. Quite possible it could also be caused by changes in the mean water velocity, e.g., because of tidal movements of the sea water.

Most likely, the fluctuations we see in the electric field is caused by interaction between surface waves. Theory (e.g., Longuet-Higgins [1950] and Kibblewhite and Wu [1991]) shows that the nonlinear interaction between surface waves generates pressure fluctuation which can propagate through the ocean and reach the seafloor even at great depths. The pressure fluctuation cause both water and seafloor motion, and can hence induce electric field fluctuations (Cox et al. [1978], Webb and Cox [1986]). In the latter papers prominent oscillation were measured in the horizontal electric field at the seafloor, with spectra having peaks between 0.1-0.2 Hz, and through theory related to the pressure fluctuation and seafloor motion. The disturbance of the seafloor is called microseism, and is evident between 0.1-5 Hz in both displacement and pressure spectra at the seafloor, with a typically peak between 0.1-0.2 Hz (Webb [1992]).

For a vertical antenna the "local" source of the measured electric field is rather complex to determine, as the pressure fluctuation can produce movement both in the water and the seafloor. As one end of the antenna is fixed to the seafloor and the other end is held up by a buoy, the measured electric field will be caused by a combination of the water, antenna and seafloor motion. The spectrum estimates of the electric field presented here, shows that the prominent peak are present in the range 0.1 Hz to 0.2 Hz for three different antennas, measured at different times and locations. As prominent peaks in the spectrum between 0.1-0.3 Hz seems to be present in all measurement of the electric field at the seafloor (Cox et al. [1978], Webb and Cox [1986], Chave et al. [1991]), and is also present in displacement and pressure spectra, it is not expected that the signal can be removed by e.g., redesigning the antennas. As long as the frequencies around 0.1-0.3 Hz is of interest for CSEM, this motion induced signal needs to be carefully monitored and analysed in order for it to be removed from the desired CSEM signal.

Bibliography

J. S. Bendat and A. G. Piersol. *Random Data: Analysis and Measurement Procedures*. Wiley-Interscience, 3 edition, 2000.

N. Bindoff, J.H.Filloux, P. Mulhearn, F. Lilley, and I. Ferguson. Vertical electric field fluctuations at the floor of the tasman abyssal plain. *Deep-Sea Research*, 33(5):587–600, 1986.

M. Blixt, 2007. Personal communication.

T. Bronez. On the performance advantage of multitaper spectral analysis. *IEEE Transactions on Signal Processing*, 40(12):2941–2946, Dec 1992.

A. Chave and J. Filloux. Observation and interpretation of the seafloor vertical electric field in the eastern north pacific. *Geophysical Research Letters*, 12(12):793–796, 1985.

A. Chave, S. Constable, and N. Edwards. Electrical exploration methods for the seafloor. In *Electromagnetic methods in applied geophysics-Applications*, chapter 12, pages 931–966. Society of Exploration Geophysicists, 1991.

A. D. Chave. On the electromagnetic fields induced by oceanic internal waves. *Geophysical research*, 89(C6):10,519–10,528, Nov. 1984.

A. D. Chave, J. H. Filloux, and D. S. Luther. Electromagnetic induction by ocean currents: Bempex. *Physics of the Earth and Planetary Interiors*, 53(3-4):350–359, 1989.

S. Constable and L. Srnka. An introduction to marine controlled-source electromagnetic methods for hydrocarbon exploration. *Geophysics*, 72(2):WA3–WA12, 2007.

C. Cox, N. Kroll, P. Pistek, and K. Watson. Electromagnetic fluctation induced by wind waves on the deep-sea floor. *Journal of Geophysical Research*, 83(C1):431–442, 1978.

M. B. Dobrin and C. H. Savit. *Introduction to Geophysical Prospecting*. McGraw-Hill Book Company, 1988.

A. Eberhard. An optimal discrete window for the calculation of power spectra. *IEEE Transactions on Audio and Electroacoustics*, AU-21(1), Feb 1973.

T. Eidesmo, S. Ellingsrud, L. MacGregor2, S. Constable, M. Sinha, S. Johansen, F. Kong, and H. Westerdahl. Sea bed logging (sbl), a new method for remote and direct identification of hydrocarbon filled layers in deepwater areas. *first break*, 20(3): 144–152, 2002.

S. Ellingsrud, T. Eidsmo, S. Johansen, M. C. Sinha, L. MacGregor, and S. Constable. Remote sensing of hydrocarbon layers by seabed logging (sbl): Results from a cruise offshore angola. *The Leading Edge*, (21):972–982, 2002.

J. Filloux. Techniques and instrumentation for study of natural electromagnetic induction at sea. *Physics of the Earth and Planetary Interiors*, 7:323–338, 1973.

A. Hanssen. Introduction to statistical signal processing and data analysis. Physics Department, University of Tromsø, 2003. Lecture Notes Fys-261.

A. Hanssen, J. Kongsli, R. Hansen, and S. Chapman. Statistics of synthetic aperture sonar images. *Proceedings of OCEANS 2003*, 5:2635 – 2640, 22-26 Sept. 2003. San Diego, CA.

F. J. Harris. On the use of windows for harmonic analysis with the discrete fourier transform. *Proceedings of the IEEE*, 66(1), 1978.

R. R. Harvey and J. C. L. R. Montaner. Electric field recording of tidal currents in the strait of magellan. *Geophysical research*, 82(24):3472–3476, Aug. 1977.

http://www.km.kongsberg.com. Mst mini ssbl transponders instruction manual. `http://www.km.kongsberg.com/KS/WEB/NOKBG0240.nsf/AllWeb\\/5C49119DBC28AF52C1256EF6004185CB?OpenDocument`, 8.Nov 2007.

S. E. Johansen, H. E. F. Amundsen, T. Røsten, T. E. S. Ellingsrud, and A. H. Bhuyian. Subsurface hydrocarbons detected by electromagnetic sounding. *First Break*, (23): 31– 36, 2005.

J. Kaiser and R. Schafer. On the use of the l_o-sinh window for spectrum analysis. *IEEE Transactions on acoustics, speech, and signal processing*, ASSP-28(1), 1980.

G. K. Keller. Rock and mineral properties. In M. N. Nabighian, editor, *Electromagnetic methods in applied geophysics – Theory. Vol. 1*, pages 12–51. Society of Exploration Geophysicists, 1987.

A. C. Kibblewhite and C. Y. Wu. The theoretical description of wave-wave interactions as a noise source in the ocean . *Acoustical Society of America Journal*, 89:2241–2252, May 1991.

F. N. Kong, H. Westerdahl, S. Ellingsrud, T. Eidesmo, and J. Johansen. 'seabed logging': A possible direct hydrocarbon indicator for deepsea prospects using em energy. *Oil and Gas Journal*, (100):30–38, 2002.

R. H. Landau and M. J. Pàez. *Computational Physics*. Wiley-vch, 2004.

J. Larsen. An introduction to electromagnetic induction in the ocean. *Physics of the Earth and Planetary Interiors*, 7:389–398, 1973.

J. Larsen. Transport and heat flux of the florida current at 27°n derived from cross-stream voltage and profiling data: theory and observations. *Philosophical Transaction: Physical Science and Engineering*, 338:169–236, 1992.

J. Lees and J. Park. Multiple-taper spectral analysis: A stand-alone c-subroutine. *Computer and Geosciences*, 21(2):199–236, 1995.

J. M. Lees. Reshaping spectrum estimates by removing periodic noise: Application to seismic spectral ratios. *Geophysical research letters*, 22(4):513–516, February 1995.

F. Lilley, A. Hitchman, P. Milligan, and T. Pedersen. Sea-surface observations of the magnetic signal of ocean swell. *Geophysical Journal International*, 159(2):565–572, 2004.

M. Longuet-Higgins. A theory of the origin of microseisms. *Philosophical Transactions of the Royal Society of London. Series A, Mathematical and Physical Sciences*, 243(857):1–35, 1950.

L. O. Løseth, H. M. Pedersen, B. Ursin, L. Amundsen, and S. Ellingsrud. Low-frequency electromagnetic fields in applied geophysics: Waves or diffusion? *Geophysics*, 71(4):W29–W40, 2006.

L. MacGregor and S. Sinha. Use of marine controlled-source electromagnetic sounding for sub-basalt exploration. *Geophysics Prosp.*, (48):1091–1106, 2000.

M. E. Mann and J. M. Lees. Robust estimation of background noise and signal detection in climatic time series. *Climatic Change*, 33(3):409–445, July 1996.

Meteorologisk institutt. `http://www.met.no`, 2007. Weather data from Troll A received on enquiry.

A. H. Nuttall. Some windows with very good sidelobe behavior. *IEEE Transactions on acoustics, speech, and signal processing*, ASSP-29(1), 1981.

N. Palshin, L. Vanyan, A. Poray-Kohits, V. Matyushenko, P. Kaikkonen, and J. Tiikkainen. Measurements of motionally induced voltage in the coastal zone of the throat of the white sea. *Earth Planets Space*, 54:433–441, 2002.

N. Palshin, A. Nozdrina, V. Matyushenko, A. Porai-Koshits, and I. V. Egorov. Electromagnetic method for monitoring currents in the gorlo of the white sea. *Oceanology*, 46(3):325–334, 2006.

E. Parzen. On estimation of a probability density function and mode. *The Annals of Mathematical Statistics*, 33(3):1065–1076, Sep 1962.

D. B. Percival and A. T. Walden. *Spectral analysis for physical applications: Multitaper and Conventional Univariate Techniques*. Cambridge University Press, 1993.

W. H. Press, S. A.Teukolsky, W. T. Vetterling, and B. P. Flannery. *Numerical recipes in C: the art of scientific computing*. Cambridge university press, 2nd edition, 1992. ISBN 0-521-43108-5.

K. S. Riedel and A. Sidorenko. Minimum bias multiple taper spectral estimation. *IEEE Transactions on signal processing*, 43(1), Jan. 1995.

T. B. Sanford. Motionally induced electric and magnetic fields in the sea. *Journal of Geophysical Research*, 76, 1971.

T. Sarpkaya and M. Isaacson. *Mechanics of wave forces on offshore structures*, chapter 4. Wave theories. Van Nostrand Reinhold Co., New York, 1981. ISBN 0442254024.

R. Shiavi. *Introduction to Applied Statistical Signal Analysis*. Academic Press, 2 edition, 1999.

B. Silverman. *Density estimation for statistics and data analysis*. Chapman and Hall, first edition, 1986.

D. Slepian. Some comments on fourier analysis, uncertainty and modeling. *Society for Industrial and Applied Mathematics*, 25(3):379–393, July 1983.

D. Slepian. Prolate spheroidal wave functions, fourier analysis, and uncertainty. v - the discrete case. *Bell System Technical Journal*, 57:1371–1430, 1978.

H. Stark and J. W. Woods. *Probability and Random Processes with Applications to Signal Processing*. Prentice-Hall, 3 edition, 2002.

A. Stuart and J. K. Ord. *Kendall's advanced theory of statistics*, volume 1. Charles Griffin & Co., London, fifth edition, 1987. Originally by Sir Maurice Kendall.

G. Sutton and N. Barstow. Ocean-bottom ultralow-frequency (ulf) seismo-acoustic ambient noise: 0.002 to 0.4 hz. *The Journal of the Acoustical Society of America*, 87 (5):2005–2012, 1990.

S. Theodoridis and K. Koutroumbas. *Pattern recognition*. Academic Press, 1998. ISBN 0-12-686140-4.

D. J. Thomson. Spectrum estimation and harmonic analysis. *Proceedings of the IEEE*, 70(9):1055–1096, September 1982.

Tromsø Geophysical Observatory. Geomagnetic data. `http://geo.phys.uit.no/geomag.html`, Oct 2007. Faculty of Science University of Tromsø, Norway.

M. Wand and M. Jones. *Kernel Smoothing*. Chapman and Hall/CRC, 1 edition, 1995. ISBN 0-412-55270-1.

S. Webb and C. Cox. Observations and modeling of seafloor microseisms. *Journal of Geophysical Research*, 91(B7):7343–7358, 1986.

S. C. Webb. The equilibrium oceanic microseism spectrum . *Acoustical Society of America Journal*, 92:2141–2158, Oct. 1992.

P. D. Welch. The use of fast fourier transform for the estimation of power spectra: A method based on time averaging over short, modified periodograms. *IEEE transactions on audio and electroacoustics*, AU-15(2):70–73, 1967.